Spring 2020

The Impact of Fine Scale Drivers on Upwelling Processes

David Kenward
University of New Hampshire, Durham

Recommended Citation
Kenward, David, "The Impact of Fine Scale Drivers on Upwelling Processes" (2020). *Doctoral Dissertations*. 2508.
https://scholars.unh.edu/dissertation/2508

The Impact of Fine Scale Drivers on Upwelling Processes

BY

David R. Kenward
B.A. Physics, B. A. Astronomy, Lycoming College

DISSERTATION

Submitted to the University of New Hampshire
in Partial Fulfillment of
the Requirements for the Degree of

Doctor of Philosophy
in
Physics

May, 2020

This dissertation has been examined and approved in partial fulfillment of the requirements for the degree of Doctor of Philosophy in Physics by:

Dissertation Director, Marc Lessard, Ph.D., Associate Professor of Physics
Harlan Spence, Professor of Physics
Lynn Kistler, Professor of Physics
Charles J. Farrugia, Research Professor of Physics
Shawna Hollen, Assistant Professor of Phsics

On [24 April, 2020]

Original approval signatures are on file with the University of New Hampshire Graduate School.

DEDICATION

I dedicate this work to my wife whose love and support was often the only thing keeping me going.

ACKNOWLEDGEMENTS

I would like to acknowledge those who have been a large part of this journey for me.

My parents; Pam and Marc who always pushed me to challenge myself and who supported me in all ways imaginable and from an early age taught me not to quit. I imagine I would not have gotten this far if I had been allowed to quit Tee-ball at a young age.

My wife, Angelika who for whatever reason agreed to move to New Hampshire with me after two years of long distance dating. Who put up with an exorbitant amount of complaining and general grumpiness over the years. I've never known a more understanding or kind soul.

My advisor, Marc Lessard who has provided me countless opportunities to work hands on with space flight hardware and sent me all over the world to support different projects. Even though that has meant risking being mauled by bears, flying in the cargo bay of a military transport, and living without plumbing at -40F, it has been the opportunity of a lifetime and I am forever grateful.

My mentors; Chris Kulp and Joanne Hill-Kittle, who both allowed me far more leeway to break things than should be trusted to someone who nominally has no idea what they are doing. The confidence I gained from those experiences has proven to be invaluable during the course of my studies.

My friend and former colleague, Bruce Fritz who was always willing to listen to my complaints, proofread my papers, ever-so-gently remind me to put proper labels on my plots for the thousandth time, and listen to me tell him the Bears still suck.

The talented group of folks I have had the great pleasure of working with the past 6 years: Mark Widholm, Mark Chutter, Ian Cohen, Michelle Salzano, Niharika Godbole,

Dominic Puoppulo, Tyler Chapman, Josh Bagley, Anthony Velte, Connor Fleury, Naomi Wight and many others in the SSC who are not named.

Thank you.

Contents

List of Figures

ABSTRACT

The Impact of Fine Scale Drivers on Upwelling Processes

by

David R. Kenward

University of New Hampshire, 2020

Ionospheric upwelling and outflow are large-scale processes which affect the dynamics of the greater magnetosphere-ionosphere-thermosphere system. Though these terms historically refer to the propensity of ions to increase in scale height and escape Earth's gravity due to a the collective effect of energization processes; that same behaviour is frequently observed to occur with neutral species within the cusp regions of the ionosphere. Although many different driving mechanisms have been identified which contribute to the energization and increase in scale height of the ionosphere, the relative energy budget of these individual drivers is debated. In this dissertation, data from the Rocket Experiment for Neutral Upwelling 2 (RENU2) will be presented as a case study of these energization processes. In particular, sub-kilometer scale features are examined to demonstrate that a significant portion of energy flux into the ionosphere is carried by fine-scale structures which have an integrated effect to cause the large-scale upwelling. An additional study is presented on the ability of pulsating aurora to drive upwelling. Pulsating aurora are spatially confined regions of periodic brightening driven by electron precipitation (on the order of 10s of keV) embedded in a diffuse aurora background (on the order of a few keV). Though these two studies are unrelated, both are linked by the idea of that large-scale responses of the ionosphere may be driven by fine-scale

structures. Additionally, a section is presented on the development and first flight of an ejectable instrument to measure electron temperatures in a distributed array from a single sounding rocket. The ability to perform multi point measurements from a single rocket platform is paramount to understanding the fine scale coupling of the ionosphere to large scale phenomenon.

CHAPTER 1

Introduction

I'm going to start from the very basics here with the question ”what's a plasma?”. This is directed at someone without any previous knowledge. Since we encounter relatively few plasmas in our daily lives and because it's rather difficult to get "hands on" with a plasma, I'd like to address some of the basic principles of a plasma. My goal in these first few pages are to provide a few basics as to how and why a plasma behaves the way it does. This is intended to be informal, something akin to a conversation and scribbling equations on a napkin. It's important to recognize that even as the picture of an event or dynamics of a region get further complicated, the basic behaviors below will still hold true. It could even be said that the basic behaviors of a plasma, and the differences in some of the parameters due to the mass of individual species (i.e., an electron is much lighter than an ion), their relative number densities, etc are what lead to some of the more complicated dynamics. This will be especially apparent for example, in the treatment of joule heating in Chapter 3. As I've just hinted at, the equations which will follow in this section will have variables for mass, charge, density, etc. Please note, that in these equations the general variable is used rather than giving equations for, say, the electron plasma frequency and the ion plasma frequency individually. Using these equations it is important to maintain specificity of the species in question.

1.1 Plasma

Plasma is a group of atoms which have been energized enough that the electrons are no longer bound to the nuclei. This does not mean that the electrons and ions are free from one another. As the old cliche states, “opposites attract” and the electrons and newly ionized atom still interact via their mutual electromagnetic field. Reaching down and wiggling the ion will cause the electron to wiggle. When enough of a gas [1] becomes ionized, wiggling our ion again will cause a collective motion in the ionized gas. This is the defining characteristic of a plasma; complex, ordered, behavior. Wiggling a single water molecule, or even a small group of water molecules inside of a bowl of water doesn’t create observable waves, you have to wiggle the whole glass for that. Wiggling a small group of molecules in a theroetical ″bowl″ of plasma can certainly cause a group wave motion that may continue well after we stop wiggling our small group. One might think that it would take a significant portion of a gas to ionize before we see plasma behavior, but in fact the threshold can be very small. Without jumping ahead and delving into more detail than appropriate for an introductory paragraph, suffice to say for now that the threshold for ″when does ionized gas become a plasma?” depends on densities and how frequently ions, electrons, and neutral atoms are bumping into each other. Another important thing to introduce here is the concept of quasineutrality. That is, over a large enough plasma, the charges should balance out such that any one infinitesimal piece of the plasma may not have a net zero charge, but a sufficient number of those pieces will.

1.1.1 Characteristic length and time scales of a simple plasma

Since we know that plasmas interact with each other through their electric fields, a natural question to ask is how far away from a particle in our plasma is its field felt? Another way to say this is what is the distance from which you must be from some plasma particle

---

[1] I say ‘gas’ here because the terrestrial and space plasmas we work with are most familiar with often begin as, or are best thought of as a gas. Though this is not always the case, some liquids (mercury being a good example) and solids may exhibit plasma behavior i.e. plasma wave modes under the right circumstances.

before its effects are shielded from you by the rest of the plasma. This is the Debye length. The Debye length is given by

$$\lambda_D = \sqrt{\frac{\epsilon_o T}{n e^2}} \tag{1.1.1}$$

where ϵ_o is the permittivity of free space, n is the number density, e the fundamental charge, and T is the temperature of the plasma.

As has been already hinted at, one of the fundamental behaviors of a plasma is that it oscillates. The plasma frequency ω_p is a function of the fundamental charge, ϵ_o the permittivity of free space, the mass m, and the number density, n.

$$\omega_p = \frac{n e^2}{\epsilon_o m} \tag{1.1.2}$$

Note that for equal densities, electron and proton (or other ion species) plasmas will have vastly different frequencies due to the inclusion of mass in the equation. The electron frequency is typically the most important when examining plasmas and is often synonymous with plasma frequency. Inverting the quantity ω_p gets you the period of the plasma oscillation, . Going back to the idea of wiggling our plasma, if we reach in and grab a few electrons and give 'em a jiggle, we'll find we can force the plasma to oscillate at frequencies different from the plasma frequency, but when we wiggle some electrons at precisely the plasma frequency, we will more easily excite large amplitude waves. This is called resonance.

In our simplistic view of a plasma, i.e. a collection of gas sufficiently heated to become partially ionized, $\frac{1}{\omega_p}$ and λ_D give time and length scales upon which processes which perturb our plasma can occur before we need more complex ideas and math to describe them.

1.1.2 Introducing a magnetic field

Things will start to get more complicated when we introduce a magnetic field into our plasma. Because the plasma particles are charged, they will react to the magnetic field. Due to the opposite sign of the charges, ions will rotate in a left handed manner, while electrons will rotate in a right handed matter (thumb in the direction of the magnetic field, fingers curl in the direction of the rotation). The frequency of this rotation is the cyclotron frequency

$$\omega_c = \frac{|e|B}{m} \tag{1.1.3}$$

where B is the strength of the magnetic field. Another quantity we can define here is pitch angle, which is the angle that a particle's velocity vector makes with the magnetic field, and can be written as

$$\alpha = \arctan\frac{v_\perp}{v_\parallel} \tag{1.1.4}$$

where α is the pitch angle, and $v_\perp$ and $v_\parallel$ are the components of the particle velocity perpendicular and parallel to the magnetic field. The perpendicular velcoity component is what leads to the circular motion around the field. Conceptually, this can be thought of similarly to a ball tethered to a stick. The tether provides the force which keeps the ball going around the stick (in our case, that force is provided by the Lorentz force which we will get to shortly). Imparting a small velocity to the ball initially leads to a circle with a small radius, imparting a larger velocity leads to a larger radius of rotation. In the case of electrons or ions oscillating around the magnetic field, this is known as the Larmor or gyro radius.

$$r_g = \frac{mv_\perp}{|e|B} \tag{1.1.5}$$

The parallel component of the velocity on the other hand, leads to what's known as guiding center motion. While a charged particle remains tied to a magnetic field line, it may move parallel/antiparallel with the field. Guiding center is the superposition of this with the cyclotron motion; i.e. the rotation around the field plus the movement along the field.

This is as good a place as any to wrap up our informal discussion of what a plasma is and why its behavior is different than the phases of matter which we are more familiar with. Much further past this, things get rather complicated. I am reminded of the famous quote from Richard Feynman which has been paraphrased enough times (and I'll do it again here) to boil down to "if you can't explain it simply, you don't understand it." I think a more appropriate Feynman quote in the same vein, and conveniently about magnetism came from a 1983 interview where the interviewer asked Dr. Feynman to explain magnetic repulsion and attraction. For several minutes, Dr. Feynman goes on about what it means to understand something – "why do you slip on ice?" may reasonably met with "because ice is slippery" because we all have an intuitive understanding of what ice is like from day to day experiences. "Why is ice slippery?" Dr. Feynman notes is a distinctly more difficult question to answer, and he relates this to a difficulty in explaining the how and why of magnetic repulsion. He then ends with the quote that I think fits quite well here:

> I really cannot do a good job, any job, of explaining magnetic force in terms of something else you are more familiar with, because I do not understand it in terms of anything else you are more familiar with.

CHAPTER 2

The Magnetosphere

The Earth has a magnetic field which is roughly dipolar in shape. The Earth's magnetic field is what gives us near-space region known as the magnetosphere. The accepted definition of the region comes from Gold (1959) who opened his seminal paper "Motions in the Magnetosphere of the Earth" with the following paragraph.

> It has now become possible to investigate the region above the ionosphere in which the magnetic field of the earth has a dominant control over the motions of gas and fast charged particles. This region is known to extend out to a distance of the order of 10 earth radii; it may appropriately be called the magnetosphere. Even though at present only the most rudimentary information is available about the behavior of this region, it is of interest to investigate the laws that dictate the motion of the material there.

This brief introductory paragraph from Gold's work highlights the main points to be addressed in this section; namely the physical extent and topology of the field, its dynamics and the dynamics of the plasma within the region.

2.1 Flux Frozen Condition

Before moving forward, I find it useful to include a brief description of Alfvén's theorem, as it has great consequences for the motions of plasma under the influence of a magnetic field. This condition is commonly expressed as

$$\boldsymbol{E} + \boldsymbol{v} \times \boldsymbol{B} = 0 \tag{2.1.1}$$

under the condition of perfect (or extremely high) conductivity. This would be true generally for the highest portions of the ionosphere as well as out along Earth's magnetic field lines in the magnetosphere, and along the field lines of the Interplanetary Magnetic Field (IMF). Put simply, if you have a magnetic field embedded in a highly conducting plasma, the magnetic field lines will move along with the flow of the plasma. This is called the frozen-in flux condition. A short illustration of why this equation denotes the flux frozen condition follows by considering some magnetic flux ϕ_B which is moving along with some plasma through a contour $\boldsymbol{C}$ subtended by surface $\boldsymbol{S}$. The amount of magnetic flux can be described by

$$\phi_B = \int_S \boldsymbol{B} \cdot dS \tag{2.1.2}$$

We then differentiate each side with respect to time, apply Faraday's law to the time varying $\boldsymbol{B}$ term, and consider the time variance due to the motion of $\boldsymbol{C}$.

$$\frac{\partial \phi_B}{\partial t} = -\int_S \nabla \times \boldsymbol{E} \cdot dS + \int_C \boldsymbol{B} \cdot V \times dL \tag{2.1.3}$$

where dL is an element of $\boldsymbol{C}$. We can use Stokes' theorem to handle our integral over C and then rearrange to obtain

$$\frac{dB}{dt} = -\int_S \nabla \times (\boldsymbol{E} + \boldsymbol{v} \times \boldsymbol{B}) \cdot dS \tag{2.1.4}$$

which is the total time rate of change of the magnetic flux through a surface. When $(\boldsymbol{E} + \boldsymbol{v} \times \boldsymbol{B} = 0$ then the integral goes to zero, and the time rate of change of the magnetic flux must also be zero, hence, the magnetic field lines are fixed to their locations in the plasma and must move with it.

2.2 Topology

Earth's magnetic field is not static, solitary, endless structure and so it has a boundary. This boundary is called the magnetopause and is the result of balancing the pressure of the solar wind with the magnetic pressure of the magnetosphere (see Figure 1) (Shue and Song, 2002). The behavior of plasma inside the magnetopause is dominated by Earth's magnetic field. Outside the magnetopause, solar wind plasma and frozen-in flux streams along through interplanetary space. As it approaches Earth however, the interaction with Earth's magnetic field causes a shock to form which lifts off the magnetopause. This is called the bow shock, as it bears a resemblance to the shock which lifts away from the bow of a boat as it passes through calm water. Between the bow shock and the magnetopause is a region of shocked solar wind plasma and turbulent magnetic field known as the magnetosheath.

These regions, being a result of interaction with solar wind and interplanetary magnetic field, are thought of as the sun-facing side of the magnetosphere. On the night side, the shape of the field is different due to not being directly in the line of sight of the solar wind. The night side of the magnetosphere is called the magnetotail. While the day side of the magnetosphere is compressed due to the pressure from the solar wind, the magnetotail is elongated. Near the equatorial region of the magnetotail lies the plasma sheet, a region of more dense plasma and diminished magnetic field strength. The plasma sheet separates the tail's north and south lobes.

On both the dayside and nightside magnetosphere there exist two regions, the first extending from approximately 1.2-3 earth radii and the second from around 3-7 earth radii both of which contain trapped energetic particles (Ganushkina et al., 2011). These are known as the Van Allen Radiation belts. The inner radiation belt is comprised largely of protons with energies above 10 MeV, while the outer radiation belt contains electrons of on the order of 0.1-10 MeV. In each case, the "typical" energy of a radiation belt particle is dependent on where in the radiation belt you are. Similarly, the location and extent of the outer radiation belt can be highly varied based on space weather conditions which cause more electrons to diffuse into and out of the outer belt.

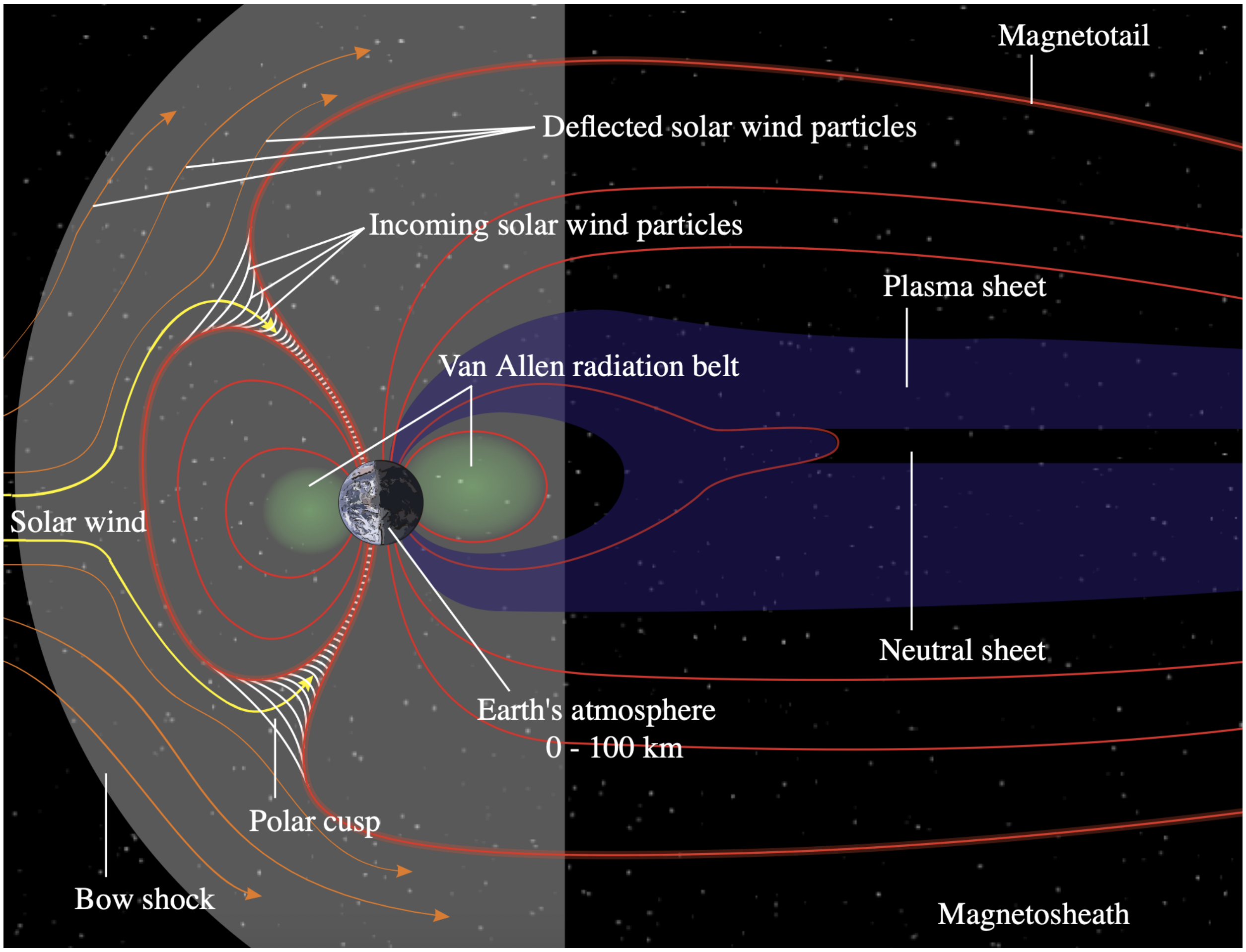

Figure 1: Diagram depicting 2-D slice of Earth's magnetosphere with major regions indicated. Photo from wikimedia commons `https://upload.wikimedia.org/wikipedia/commons/5/50/Structure_of_the_magnetosphere-en.svg`.

2.2.1 Magnetic Reconnection

A major way in which energy from the solar wind couples to Earth's magnetosphere (and eventually, the ionosphere-thermosphere system) is through the process of magnetic reconnection. Magnetic reconnection occurs on both the dayside and nightside of the magnetopshere. It begins on the dayside, where the solar interplanetary magnetic field (IMF) meets with Earth's magnetic field and, because magnetic field lines cannot cross, "pushes" on it. When the IMF and the Earth's magnetic field have anti-parallel components, this is a higher energy configuration and the magnetic field lines "snap" and reconnect. This results in open field lines with one end at the Earth's polar regions and the other end which extends out into the solar wind (Gonzalex et al., 1994). Solar wind particle and wave energy may stream directly towards Earth along these open field lines.

After reconnecting on the dayside, the open field lines convect across the polar regions and drape across the magnetotail, causing the elongation of the tail. In the tail region, these field lines reconnect again and undergo dipolarization, sending more particle energy streaming towards Earth as part of the process of a geomagnetic substorm (see Chapter 5). Newly reconnected field lines eventually travel back to the dayside as part of the Dungey Cycle. The exact details of the reconnection process are not yet completely known, and competing models exist which allow for different rates of reconnection, dynamics, etc. The basics of this coupling process are depicted in figure 2.

2.3 Particle motions

In Section 1.1.2, guiding center motion was discussed and described as the superposition of a particle moving linearly along a magnetic field line while gyrating around it. A rotating electron however, can be interpreted as a current. That loop of current then has a magnetic moment which can be written in general form as

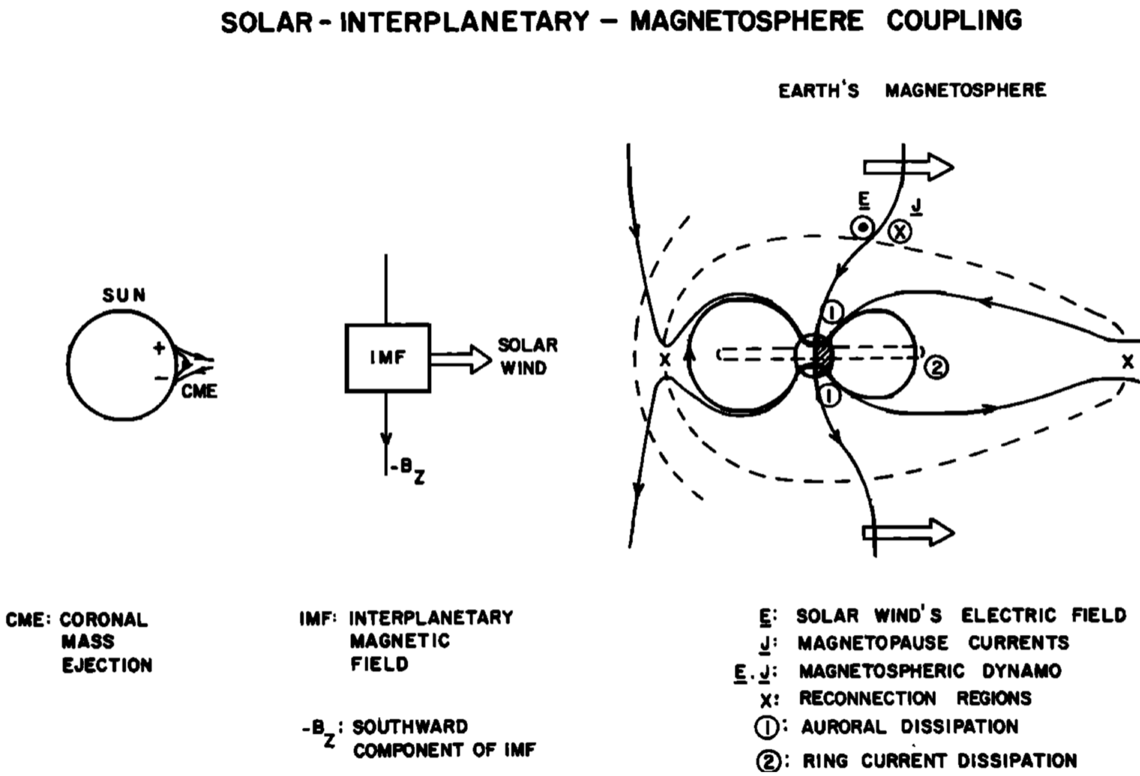

Figure 2: A diagram depicting the coupling of energy derived from the solar wind into Earth's magnetosphere. Field lines reconnect on the dayside and then convect over the polar regions to the dayside where they eventually reconnect again and undergo dipolarization. Taken from Gonzalex et al. (1994)

$$\mu = I\pi r^2 \tag{2.3.1}$$

but for our specific case, $r = r_g$ and $I = \frac{q\omega_c}{2\pi}$ which we can plug immediately into the formula for μ.

$$\mu = \frac{mv_\perp}{2B} \tag{2.3.2}$$

This is the magnetic moment for a particle undergoing guiding center motion. It is invariant under “small enough” or “slow enough” changes, meaning the the changes encountered by the particle (such as the strength or direction of the magnetic field) should happen on time scales longer than a the period of gyration and/or over length scales longer than a gyroradius. In the magnetosphere, this means that for a particle traveling along a magnetic field line as it approaches a polar region where B changes, $v_\perp$ must also change in order for μ to remain constant. Eventually, (and assuming the particle does not collide with the atmosphere) the direction of $v_\perp$ will flip entirely and the particle will travel back down the field line from whence it came. This is called magnetic mirroring and the point at which the particle reverses direction is known as the mirror point. As this can happen in either hemisphere, the particle will “bounce” back and fourth between hemispheres. This motion is what causes particles of specific energies to become trapped in the radiation belts.

In addition to the guiding center and bounce motion, magnetospheric plasma may undergo drift motion. This motion is perpendicular to the direction of B and is the result of a number of different causes, all of which are mathematically represented as a cross product. Gradient and curvature drifts are a result of the geography of earth’s magnetic field. Gradient drift occurs when you have a magnetic field whose strength has a spatial dependence, and curvature drift which occurs when you have a magnetic field which has a radius of curvature. A third drift motion is what’s called “E cross B” drift, as it arises from having an electric field perpendicular to a magnetic field.

$$v_D = \frac{cE \times B}{B^2} \tag{2.3.3}$$

E cross B drift is unique that it does not depend on the charge of the particle nor the mass, so ions and electrons will drift together.

CHAPTER 3

The Ionosphere - Thermosphere System

The ionosphere and thermosphere are two overlapping regions of Earth's atmosphere which extend from roughly 60-85 km upwards to 1000 km. The two coexisting regions are treated separately due to their difference in behavior; the charged particles of the ionosphere interact with Earth's magnetic field, while the neutral atoms and molecules of the thermosphere do not. These two regions do interact with each other; the exchange of energy between the two and the dynamics which carry that energy is a large focus of this work.

3.0.1 Thermosphere

The thermosphere is the layer of the atmosphere which lies above the mesosphere. The boundary between the two is the higher altitude of two temperature minima which lie in the atmospheric system, i.e. the mesopause (see Figure 4. The typical height for the mesopause is given as about 85 km. From the mesopause up to about 110 km, the thermosphere is a homogenous mixture of atmospheric gases due to turbuluent mixing. above this boundary known as the turbopause, the thermosphere becomes stratified – atoms and molecules separate into layers where different species dominate.

At the thermosphere, the extreme ultraviolet (EUV) portion of the solar spectrum is absorbed which causes photo-ionization of the neutral gas. This absorption and ionization is what generates the ionosphere.

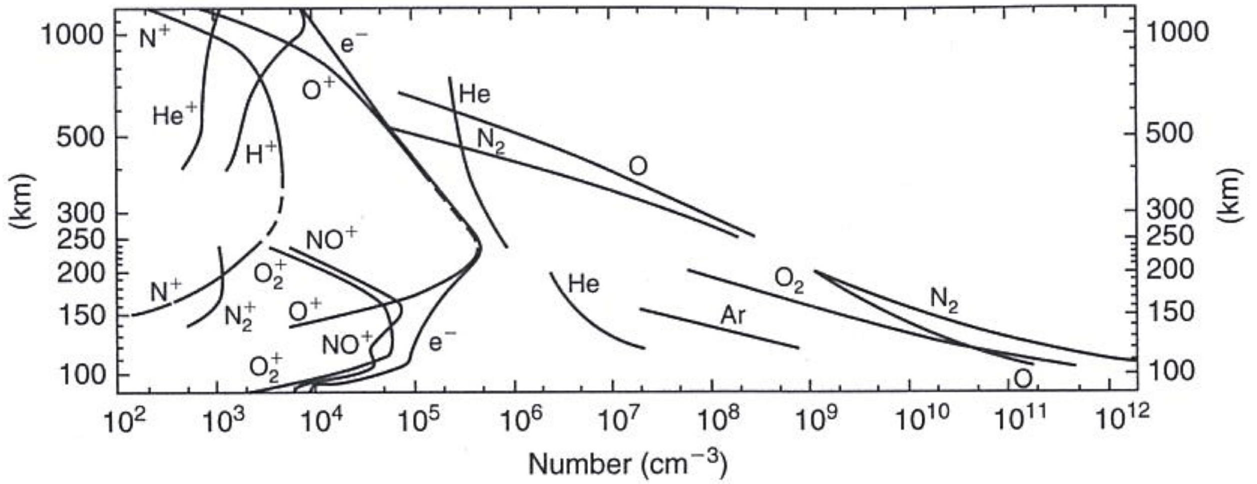

Figure 3: A plot showing the height structuring of common neutral and ion species in the ionosphere-thermosphere system. Figure from (Kelley, 2009)

3.1 Ionosphere

The generation of the ionosphere by EUV absorption in the thermosphere means that the overall structure of the ionosphere is intimately tied to the thermosphere. The dependence on EUV to produce ionization also leads to daily and yearly variations in ionospheric density (see Figure 3 for density of various species as a function of height). Local maximas in the electron density define the different regions of the ionosphere. The lowest region, the D region, extends from the bottom (near 60 km) of the ionosphere up to around 85 km. The D region is the most tenuous portion of the ionosphere. As such, it disappears at night without continuous photoionization by x-rays which penetrate low enough to create ionization at the lowest portion of the thermosphere. The E region extends from 90 - 150 km (see Figure 4). Unlike the D region, the E region does not disappear during night time, though the density does diminish without solar EUV present. The highest region of the ionosphere, the F region, contains the highest density in the ionosphere, around 10^{12} electrons per cubic meter at an altitude of 250 - 300 km. During the day, the F region maxima will often split into two. These peaks are then referred to as the F_1 (lower) and F_2 (upper) layers.

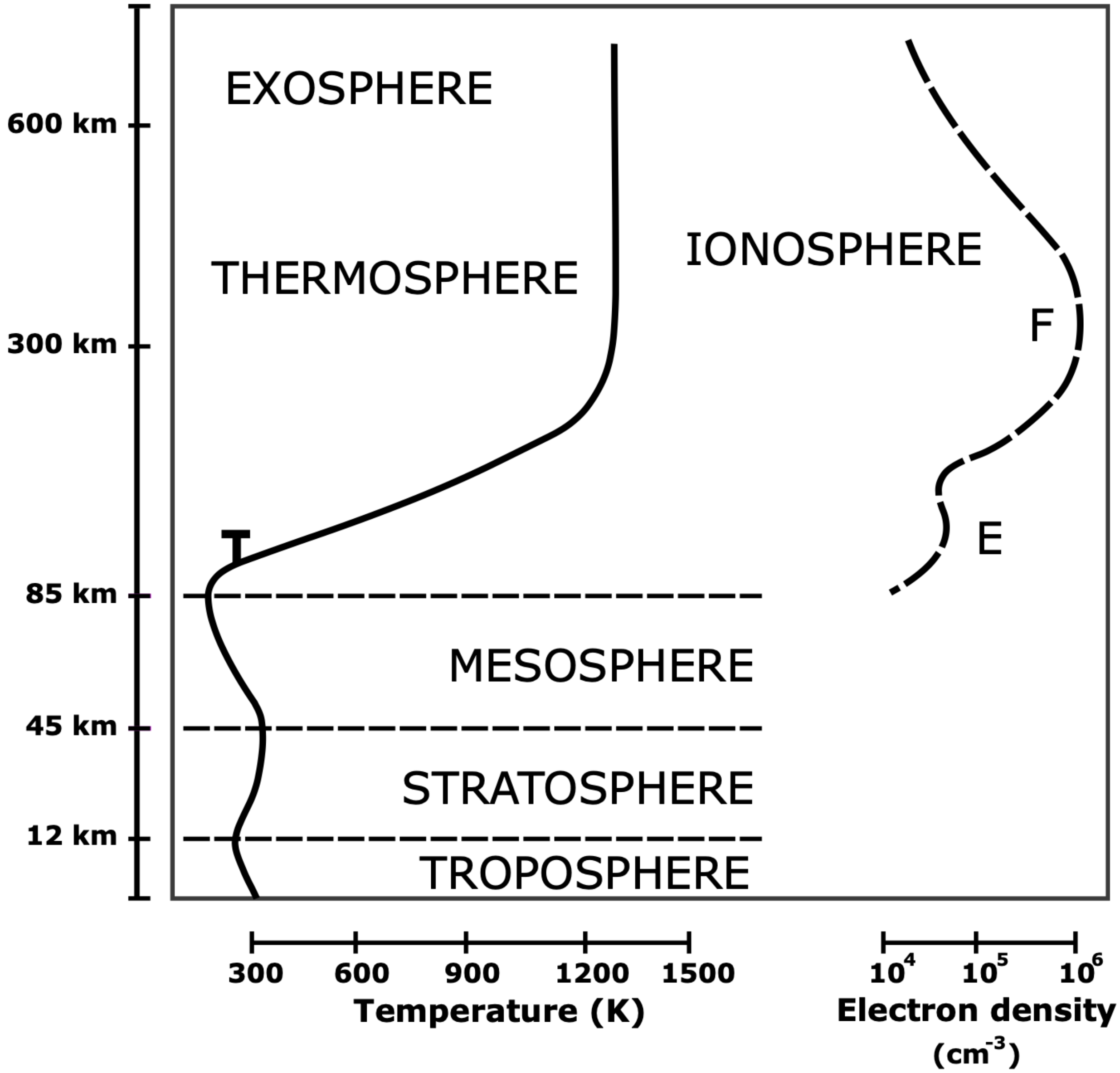

Figure 4: A figure showing the basic structure of the ionosphere-thermosphere system showing a typical temperature profile for the neutral thermosphere and a typical density profile of the ionospheric plasma. Photo from Wikimedia commons:`https://upload.wikimedia.org/wikipedia/commons/1/18/Atmosphere_with_Ionosphere.svg`

3.1.1 Convection and currents

The electric field system at the magnetosphere maps into the ionosphere along equipotentials, i.e. field lines. From a very simplistic point of view, this system can be thought of as a circuit such as the one in 5. In this picture, we treat the field lines mapping from the magnetosphere (V, in the diagram – the source or power supply) and will apply the "perfectly conducting" or flux frozen approximation first mentioned in Section 2.1. The ionosphere, being not perfectly conducting, will have a resistance, and so currents must flow.

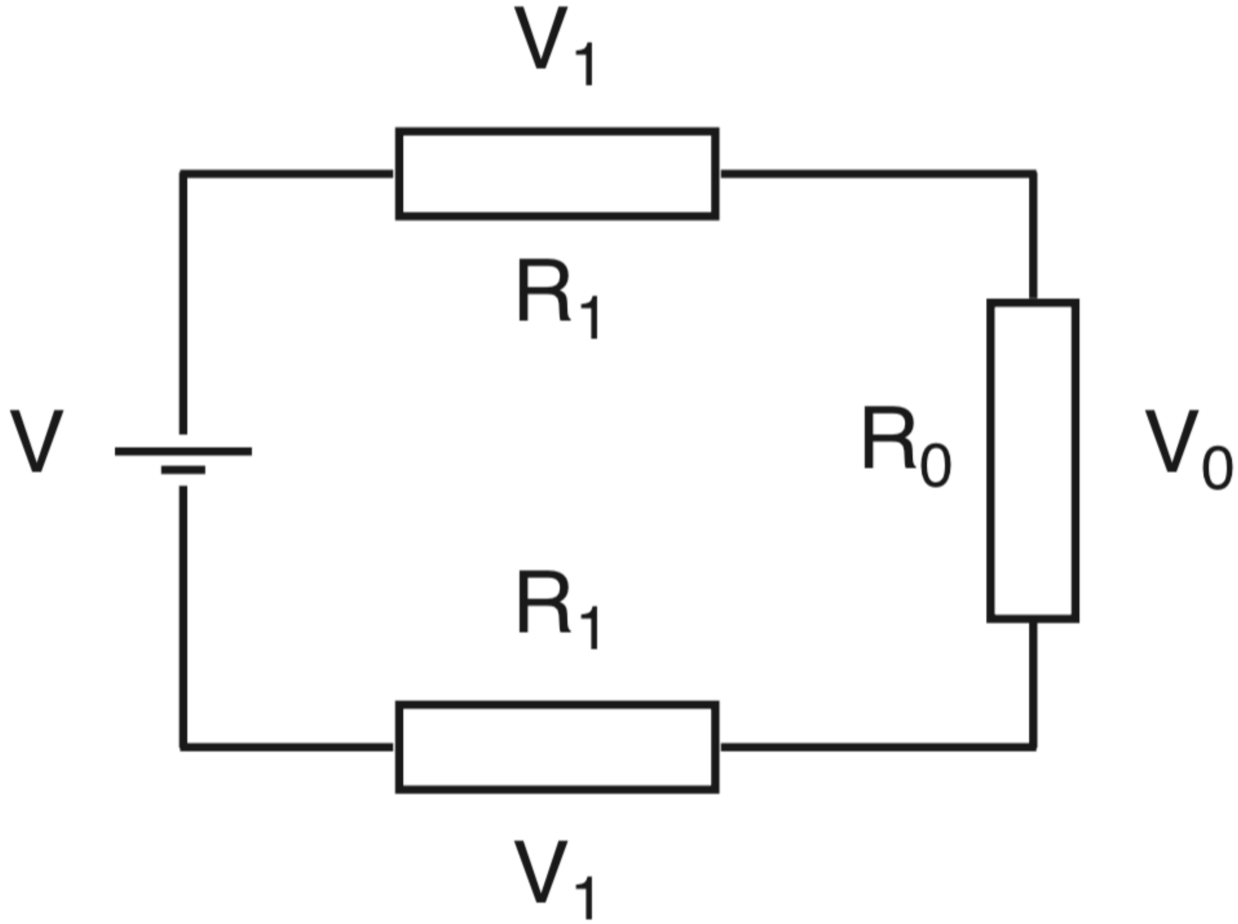

Figure 5: A simple circuit representation of the M-I current system

Here, the ionosphere is represented by resistor R_o, and the equipotential field lines as R_1. The current in the system is

$$I = \frac{V}{R_o + 2R_1} \tag{3.1.1}$$

The voltage in the "ionosphere" i.e. resistor R_o is expressed as

$$V_o = \frac{VR_o}{R_o + 2R_1} \tag{3.1.2}$$

If we apply the condition that $R_o >> R_1$ then $V_o \approx V$ and $V_1 << V_o$ and the voltage drop across R_1 is nearly zero. This is a simple analogue to illustrate what's meant by the field lines being equipotentials while also motivating the discussion of the current system which results.

The electric field which maps from the magnetosphere to the ionosphere is perpendicular to the magnetic field as a result of the magnetic field lines being equipotentials. The potential difference between the field lines must be the same everywhere so that

$$E_i = r_m i E_m \tag{3.1.3}$$

where E_n is the electric field associated with the magnetosphere or ionosphere according to the subscript. The term $r_m i$ is a mapping factor which is largely dependent on the topology of the field. It is born out of the condition that

$$s_i E_i = s_m E_m \tag{3.1.4}$$

meaning the electric fields at the magnetosphere and ionosphere must be equivalent except for some scaling factor, s_n. The mapping factor $r_m i$ is simply the ratio $\frac{s_m}{s_i}$.

If we consider that the Earth's magnetic field is roughly dipolar, the topology dictates that $r_m i > 1$ due to the convergence of the field lines as one follows two equipotential field lines from the magnetosphere to the ionosphere. This means that a small electric field out in the magnetosphere can be much larger once mapped into the ionosphere.

The results of mapping the electric field into the ionosphere, at high latitudes, are induced currents. To understand how these currents are induced and the dynamics involved it is useful to take a step back and start with the simple question: what is a current?

A current is simply a net rate of flow of charge past a point. We can express this as

$$j_{net} = j_i + j_e \tag{3.1.5}$$

which says simply that our net current is the sum of our currents carried by ions, and our currents carried by electrons. Since we are going to be applying this to our model ionosphere, let's make the assumption that $n_e = n_i$. Additionally, let's assume there is a single ion species and we will keep the formalism that positive current is carried by ions. We can now write

$$j_{net} = en_e(v_i - v_e) \tag{3.1.6}$$

where v_i and v_e are the respective velocities of the ions and electrons. To understand the currents here, we need to understand the motion of the particles involved. Keeping things as simple as possible, consider that those particle species are a single ion species, a single neutral species, and electrons. Since there is a magnetic field, the ion and electron species will be undergoing gyroscopic motion around the field line at their respective frequencies and radii. We will ascribe coordinates x, y, z to the system, aligning z to the background magnetic field and allowing the gyration of the charged particles around the field line to occur in the $x - y$ plane.

To investigate the velocities of the particles we will use a kinetic picture in which ions and electrons collide like rigid spheres with the neutral species. The cross section of that collision is given by $\lambda_n = \pi r_o^2$ where r_o is the radius of the target (i.e. the neutral species, in the frame that the neutrals are at rest and the electrons and ions are moving through it). The average velocity of an ion or neutral is given by $< V >$, and then we can write the $\nu_{xn} = n_n \lambda_n < V >$, with n_n the neutral density and the ν_{xn} denoting the collision frequency between our neutrals and either electrons or ions. The force experienced by an electron or ion through these collisions is then

$$\boldsymbol{F_{coll}} = m_x \nu_{xn} < \boldsymbol{V} > \tag{3.1.7}$$

In the case that there are electric or magnetic fields, or that these collisions can induce a separation of charge (which will be shown later), the collisional force experienced by the particles can be set equal to the Lorentz force equation.

$$m_x \nu_{xn} < \boldsymbol{V} >= e(\boldsymbol{E}+ < \boldsymbol{V} > \times \boldsymbol{B}) \tag{3.1.8}$$

We can now solve for the velocities of the ions and electrons separately. We have already aligned our coordinate system so that our $B = B_z$, and recalling that our geomagnetic field lines are lines of equipotential, $E_z = 0$. We now perform the cross product and collect constants to write

$$v_x e_x + v_y e_y = \frac{q}{m\nu}(E_x e_x + E_y e_y + v_y B e_x - v_x B e_y) \tag{3.1.9}$$

where e_i gives the vector direction. We recognize that we can divide B out from the term in parentheses on the right hand side of the equation and our fractional constant becomes $\frac{\omega}{\nu}$ with 1.1.3. We can now write two separate equations, one for v_x and one for v_y (dropping the e_i notation since it is understood now that the e_x and e_y directions are being separated)

$$\begin{aligned} v_x &= \frac{\omega}{\nu}(\frac{E_x}{B} + v_y) \\ v_y &= \frac{\omega}{\nu}(\frac{E_y}{B} - v_x) \end{aligned} \tag{3.1.10}$$

From here, we can solve for the respective velocities by plugging in either equation into the other and solving. This results in the two independent equations

$$\begin{aligned} v_x &= \frac{1}{1+\frac{\omega^2}{\nu^2}}[\frac{\omega E_x}{\nu B} + \frac{\omega^2 E_y}{\nu^2 B}] \\ v_y &= \frac{1}{1+\frac{\omega^2}{\nu^2}}[\frac{\omega E_y}{\nu B} - \frac{\omega^2 E_x}{\nu^2 B}] \end{aligned} \tag{3.1.11}$$

For ease of reading, subscripts denoting ions, electrons, and neutrals are dropped; but it is understood that ω refers to the gyrofrequency of the respective species of ion or electron, and ν to the collision rate between ions and neutrals or electrons and neutrals. The two equations 3.1.11 can be written more compactly in vectorial form as

$$v_{perp} = \frac{1}{1+\frac{\omega^2}{\nu^2}}[\frac{\nu \boldsymbol{E}}{\omega} + \frac{\boldsymbol{E} \times \boldsymbol{B}}{B^2}] \tag{3.1.12}$$

Now with equation 3.1.6 we can plug in the perpendicular velocities and obtain the currents perpendicular to the background field.

$$j_{perp} = qn_e \frac{1}{1+\frac{\omega_i^2}{\nu_i n^2}}[\frac{\nu_i n \boldsymbol{E}}{\omega} + \frac{\boldsymbol{E}\times\boldsymbol{B}}{B^2}] - \frac{1}{1+\frac{\omega_e^2}{\nu_e n^2}}[\frac{\nu_e n \boldsymbol{E}}{\omega} + \frac{\boldsymbol{E}\times\boldsymbol{B}}{B^2}] \tag{3.1.13}$$

With a vigorous application of algebra, this can be written succinctly as

$$j_{perp} = \sigma_P \boldsymbol{E} + \sigma_H \frac{\boldsymbol{E}\times\boldsymbol{B}}{B^2} \tag{3.1.14}$$

where we have substituted σ_P and σ_H in accordance to the equations below.

$$\sigma_P = \frac{en_e}{B}(\frac{\omega_i \nu_{in}}{\omega_i^2 + \nu_{in}^2} + \frac{\omega_e \nu_{en}}{\omega_e^2 + \nu_{en}^2}) \tag{3.1.15}$$

$$\sigma_H = \frac{en_e}{B}(\frac{-\omega_i^2}{\omega_i^2 + \nu_{in}^2} + \frac{\omega_e^2}{\omega_e^2 + \nu_{en}^2}) \tag{3.1.16}$$

Though not included in the parallel currents, it is convenient to also define $\sigma_{||}$ here as well as

$$\sigma_{||} = e^2 n_e(\frac{1}{m_i \nu_{in}} + \frac{1}{m_e \nu_{en}}) \tag{3.1.17}$$

These are the Pedersen, Hall and parallel (i.e. field aligned) conductivities. Pedersen conductivity is in the direction parallel to the electric field and perpendicular to the magnetic field, while Hall conductivity is perpendicular to both. The values given in 3.1.15, 3.1.16 and 3.1.17 all refer to the 2-D conductivities since the conductivity can be a function of altitude. The height integrated conductivities are denoted with a capital sigma and are, as the name implies, found by integrating the 2-D conductivity along the vertical direction. With all of this, we can succinctly write the 3-D currents as

$$\boldsymbol{J} = [\sigma](\boldsymbol{E} + \boldsymbol{V} \times \boldsymbol{B}) \tag{3.1.18}$$

where $[\sigma]$ is the conductivity tensor and may be written as below.

$$[\sigma] = \begin{bmatrix} \sigma_P & \text{-}\sigma_H & 0 \\ \sigma_H & \sigma_P & 0 \\ 0 & 0 & \sigma_{||} \end{bmatrix} \tag{3.1.19}$$

3.2 Heating

This section is meant to be a jumping off point for future students or graduate students confused by discussions surrounding joule heating. The derivations which follow are based entirely on the sources cited within it. I have done my best to bring some cohesion to the approaches taken by each source in discussing what joule heating is. This topic is something that is often discussed and debated – the kind of thing where if you ask a handful of different scientists at a conference, you're likely to get a handful of different answers. It is apparent in the literature cited below that this confusion is due in large part to inexact language and some amount of pedantry. It is my hope that while this section is by no means a complete or definitive treatise on the topic that it provides enough information for the confused future student to gain some traction on the subject.

In writing equation 3.1.18 we have provided a succinct relationship between the currents, electric and magnetic fields. However, care must be taken in using this relation, as E and V both depend on the frame in which they are measured Tu et al. (2011) and must therefore be measured in the same frame. This becomes particularly important for considerations where Joule or Ohmic heating is discussed. Traditional treatment of Joule dissipation is defined in the neutral atmosphere frame and is given by $j \cdot (\boldsymbol{E} + \boldsymbol{U_n} \times \boldsymbol{B})$ (where $\boldsymbol{U_n}$ is the flow velocity of the neutral thermosphere) often referred to as "j dot E" heating and is a sum of frictional heating from ion-neutral collisions and "true" Joule disspation, i.e. heating which is proportional to ηj^2 (Strangeway, 2012; Vasyliunas and Song, 2005). Alternatively, when this is expressed in the plasma frame as $\eta j^2 = j \cdot (\boldsymbol{E} + \boldsymbol{U} \times \boldsymbol{B})$ (where $\boldsymbol{U}$ is the flow velocity of the plasma and η is a constant which contains the electron ion and electron neutral collision frequencies) this has the j^2 term explicitly stated and thus, this casting of Joule dissipation takes the functional form of classical Ohmic dissipation Vasyliunas and Song (2005); Tu et al. (2011).

There is a great deal of debate within the community as to what this precisely means. The confusion arises due to the dynamics of the ionosphere-thermosphere environment which contain two media: the neutral atmosphere with velocity $\boldsymbol{U_n}$ and the plasma with velocity $\boldsymbol{U}$ (sometimes the plasma velocity is given as $\boldsymbol{U_i}$ as the ion velocity is a close approximation of the overall plasma velocity). The choice to express Ohm's law in the neutral frame or the plasma frame does not impact the functional form of the equation but rather the constants which appear which are associated joule dissipation. To illustrate and ultimately clarify what is meant in discussing joule dissipation, we will consider Ohm's law in both the plasma and neutral frames.

In specifying the plasma or neutral velocity, we are identifying a specific frame for the electric field. J cannot depend only on E; but rather on the electric field in the particular frame of reference, expressed by Vasyliunas and Song (2005) as $\boldsymbol{E}* = \boldsymbol{E} + \boldsymbol{V} \times \frac{\boldsymbol{B}}{c}$. The selection of a velocity frame must be taken into consideration, as J can be expressed in terms of an $\boldsymbol{E} + \boldsymbol{V}t \times \frac{\boldsymbol{B}}{c}$ which satisfies the equation

$$\boldsymbol{V} = \boldsymbol{U} + \xi(\boldsymbol{U_n} - \boldsymbol{U}) \tag{3.2.1}$$

where ξ is an arbitrary constant Vasyliunas and Song (2005). Furthermore, J can be written as proportional to $\boldsymbol{U_n}$ or to $\boldsymbol{U}$ with different conductivity coefficients (Song et al., 2001). In order to more effectively highlight what is meant by Joule or Ohmic heating, let us consider a three fluid ionosphere.

The current density is still given by 3.1.6, but we will define a plasma velocity as

$$\boldsymbol{U} = \frac{m_i \boldsymbol{v_i} + m_e \boldsymbol{v_i}}{m_i + m_e} = \boldsymbol{u_i} + \frac{m_e}{m_i}\boldsymbol{u_e} \tag{3.2.2}$$

where in the far right hand side of the equation we have dropped terms in accordance with $m_i >> m_e$ and we have made a change to representing the all velocities as u_s rather than v_s to follow better in line with established literature.

We will begin by examining Ohm's law in the plasma frame. We can write the momentum equations for a three fluid ionosphere for the ions, electrons and neutrals respectively as (derivation follows closely with Song et al. (2001)).

$$N_e m_i \frac{d}{dt}\boldsymbol{u_i} = -\nabla P_i + eN_e(\boldsymbol{E} + \boldsymbol{u_i} \times \boldsymbol{B}) + \boldsymbol{F_i} - N_e m_i \nu_{in}(\boldsymbol{u_i} - \boldsymbol{u_n}) - N_e m_i \nu_{ie}(\boldsymbol{u_i} - \boldsymbol{u_e}) \tag{3.2.3}$$

$$N_e m_e \frac{d}{dt}\boldsymbol{u_e} = -\nabla P_e + eN_e(\boldsymbol{E} + \boldsymbol{u_e} \times \boldsymbol{B}) + \boldsymbol{F_e} - N_e m_e \nu_{en}(\boldsymbol{u_e} - \boldsymbol{u_n}) - N_e m_e \nu_{ei}(\boldsymbol{u_e} - \boldsymbol{u_i}) \tag{3.2.4}$$

$$N_n m_n \frac{d}{dt}\boldsymbol{u_n} = -\nabla P_n + \boldsymbol{F_n} - N_n m_n \nu_{ni}(\boldsymbol{u_n} - \boldsymbol{u_i}) - N_n m_n \nu_{ne}(\boldsymbol{u_n} - \boldsymbol{u_e}) \tag{3.2.5}$$

where the variables all follow from the previous discussion, and F_s are the external forces of the fluid species (such as gravity). If we enforce a steady state, with no external forces, and negligible gradient forces then we can write

$$\boldsymbol{E} + \boldsymbol{u_i} \times \boldsymbol{B} = \frac{m_i \nu_{in}}{e}(\boldsymbol{u_i} - \boldsymbol{u_n}) + \frac{m_i \nu_{ie}}{q}(\boldsymbol{u_i} - \boldsymbol{u_e}) \tag{3.2.6}$$

$$-\boldsymbol{E} + \boldsymbol{u_e} \times \boldsymbol{B} = \frac{m_e \nu_{en}}{e}(\boldsymbol{u_e} - \boldsymbol{u_n}) + \frac{m_e \nu_{ei}}{q}(\boldsymbol{u_i} - \boldsymbol{u_e}) \tag{3.2.7}$$

Using equation 3.2.2 to plug in for u_i and u_e we arrive at

$$\boldsymbol{E} + \boldsymbol{U} \times \boldsymbol{B} + \frac{m_e}{m_i e N_e}\boldsymbol{j} \times \boldsymbol{B} = \frac{m_i \nu_{in}}{q}(\boldsymbol{U} + \frac{m_e}{m_i q N_e}\boldsymbol{j} - \boldsymbol{u_n}) + \frac{m_i \nu_{ie}}{e}(\boldsymbol{U} + \frac{m_e}{m_i e N_e}\boldsymbol{j} - \boldsymbol{U} + \frac{q}{e N_e}\boldsymbol{j}) \tag{3.2.8}$$

$$-\boldsymbol{E} + (\boldsymbol{U} - \frac{\boldsymbol{j} \times \boldsymbol{B}}{e N_e}) = \frac{m_e \nu_{en}}{e}(\boldsymbol{U} - \frac{\boldsymbol{j}}{e N_e} - \boldsymbol{u_n}) - \frac{m_e \nu_{ei}}{e}(\boldsymbol{U} + \frac{m_e j}{e m_i N_e} - \boldsymbol{U} + \frac{\boldsymbol{j}}{e N_e} \tag{3.2.9}$$

with the assumptions we have already made about the system, we have that $m_i N_e \nu_{ie} = m_e N_e \nu_{ei}$ and so we can cancel and gather terms to arrive at

$$\boldsymbol{E} + \boldsymbol{U} \times \boldsymbol{B} = \frac{m_i \nu_{in}}{e}(\boldsymbol{U} - \boldsymbol{u_n}) - \frac{m_e \boldsymbol{j}}{N_e e^2}(\nu_{en} - \nu ei) - \frac{m_e \boldsymbol{j}}{m_i} \times \boldsymbol{B} \tag{3.2.10}$$

$$\boldsymbol{E} + \boldsymbol{U} \times \boldsymbol{B} = \frac{-m_e \nu_{en}}{e}(\boldsymbol{U} - \boldsymbol{u_n}) + \frac{m_e \boldsymbol{j}}{N_e e^2}(\nu_{en} - \nu_{ei}) + \boldsymbol{j} \times \boldsymbol{B} \tag{3.2.11}$$

In these two equations, we define

$$\eta = \frac{m_e}{N_e e^2} \tag{3.2.12}$$

which is the coefficient in front of the j^2 term in classical ohmic dissipation. We can also write the plasma momentum by adding equations 3.2.10 and 3.2.7 and obtain

$$\boldsymbol{j} \times \boldsymbol{B} = N_e(m_i \nu_{in} + m_e \nu_{en})(\boldsymbol{U} - \boldsymbol{U_n}) + \frac{m_e \boldsymbol{j}}{e}(\nu_{in} - \nu_{en})\boldsymbol{j} \tag{3.2.13}$$

We can perform the same derivation but with $V = U_n$ which is how we usually define the electric field in the ionosphere, i.e. in the neutral atmosphere frame. To do this, it is algebraically simpler to begin with Ohm's law and the collisional term in the plasma momentum equation as expressed by Vasyliunas and Song (2005)

$$\boldsymbol{E} + \boldsymbol{U_n} \times \boldsymbol{B} = \frac{1}{eN_e}\boldsymbol{j} \times \boldsymbol{B} + \frac{m_e}{eN_e}\frac{\partial \boldsymbol{j}}{\partial t} \tag{3.2.14}$$

with

$$\frac{\partial \boldsymbol{j}}{\partial t} = -(\nu_{ei} + \nu_{en} + \frac{m_e}{m_i}\nu_{in})\boldsymbol{j} + eN_e(\nu_{en} - \nu_{in})(\boldsymbol{U} - \boldsymbol{U_n}) \tag{3.2.15}$$

This is functionally the same as our previous expressions but provides a more succinct starting point requiring less algebra to arrive at (in the hope that by doing so preserves clarity and is easy to follow). It should be noted that these two equations also recover the result from equations 3.2.10, 3.2.11 and 3.2.13 when the appropriate velocities are plugged in and terms of order $\frac{m_e}{m_i}$ are neglected.

Following similar steps as was done for the plasma frame derivation, we arrive at the expression for the entire plasma

$$\boldsymbol{E} + \boldsymbol{U} \times \boldsymbol{B} = \frac{1}{eN_e}\boldsymbol{j} \times \boldsymbol{B} - \frac{m_e(\nu_{ei} + \nu_{en})}{e^2 N_e} - \eta \boldsymbol{j} \tag{3.2.16}$$

where here we have

$$\eta = \frac{m_e \nu_{in}}{m_i} - \frac{m_e^2}{e^2 N_e}\left(\frac{(\nu_{en} - \nu_{in})(\nu_{in} - \nu_{en})}{m_i \nu_{in} + m_e \nu_{en}}\right) \tag{3.2.17}$$

which from inspection we can see that even neglecting terms of order $\frac{m_e}{m_i}$ is a more complex expression. It is also apparent that there is a term missing from this equation in comparison to equations 3.2.10 and 3.2.11: the frictional or drag term, i.e. the $U - U_n$ term. Instead, the effects of the neutral atmosphere colliding with or flowing through the plasma are contained entirely within the dissipative term, η. This is to say, in the plasma frame we can separate out two sources of heating: frictional/drag and "true" ohmic dissipation which depends only on the electron collisional terms. In the neutral frame, η includes the ion collisional terms and in this sense, "j dot E" or joule heating is not "true" joule heating but rather frictional heating recast as ohmic dissipation.

CHAPTER 4

The Cusp

The magnetospheric cusp describes the region of Earth's magnetic field in which solar wind and magnetosheath particles may stream freely towards the Earth. The cusp is a small region in terms of magnetospheric/ionospheric scales – typically a few degrees in latitudinal extent and several hours in local time. Despite being a small region, the cusp is of particular interest as it sees a high occurrence rate of neutral density enhancements.

The cusp region was first noted by Chapman and Ferraro (1931) who treated it as a point of near zero magnitude in the magnetospehre. In topology, a "cusp" is defined as a point at which two branches of a curve meet such that their tangent lines have equal slopes. The name cusp then should be self-evident if you consider the picture of a dipole magnet with it's field lines. A topological cusp is present at each pole. That picture is inherently 2-D, while magnetic field lines are inherently 3-D. The same type of structure in 3-D is (topologically) termed "cleft" which describes the boundary of the closed field line torus. See Figure 6 for a depiction of the 3-D cusp/cleft structure.

In the realm of auroral physics, the terms "cusp" and "cleft" were used interchangeably for a time – with only minor distinction. Heikkila and Winningham (1971) reported high latitude fluxes of low-energy (which they defined as being <1 keV) electrons and protons near the open-close field line boundary on the dayside of the magnetosphere. They deemed this "cusp precipitation" and postulated that entry of these particles into the ionosphere was due to the nulls predicted first by Chapman and Ferraro (1931). Soon after this, the term "cleft" was taken to refer to precipitation which shows a similar energy spectrum in the same vicinity as the cusp (i.e. near magnetic noon) but understood to be the ionospheric footprint of the Lower Latitude Boundary Layer (LLBL) funnel.jpg funnel.jpg

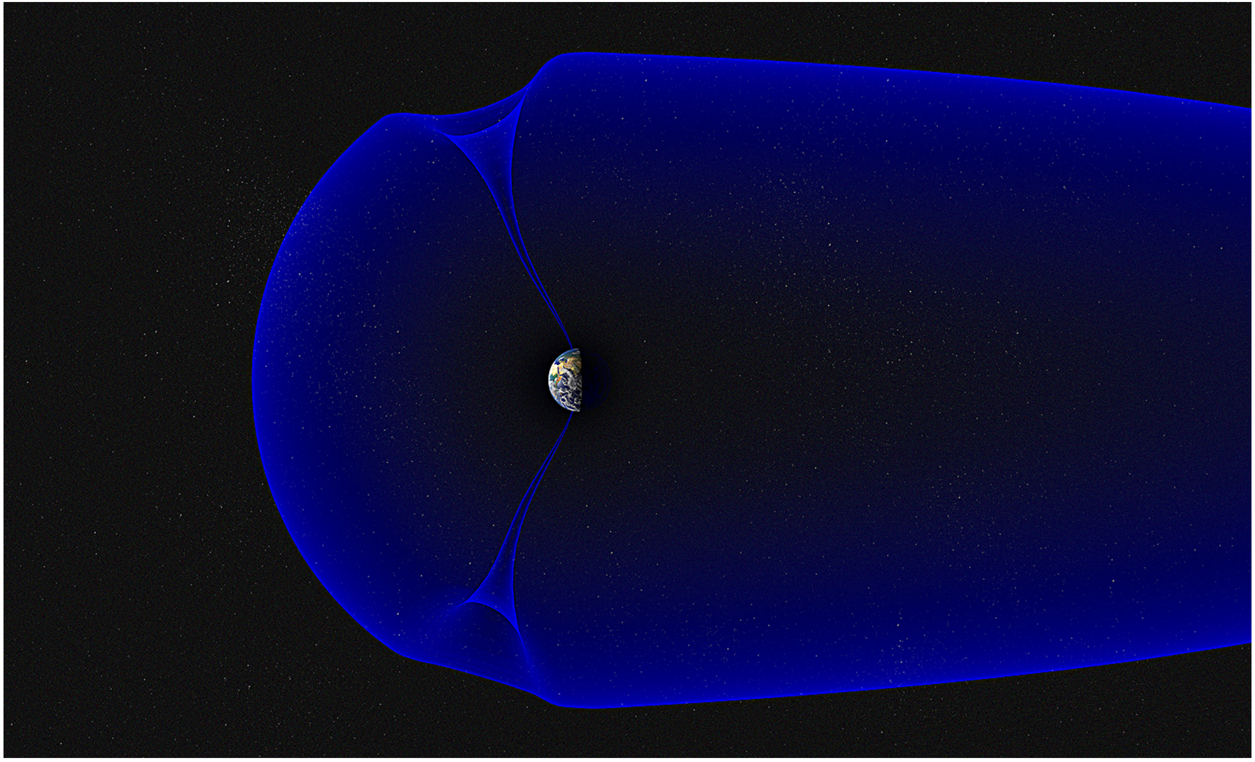

Figure 6: Diagram depicting the "funnel" shape of the cusp. From this, one can imagine taking a 2-D slice of the image and seeing how the funnel shape becomes two lines which meet at a theoretical point. Taken from https://www.nasa.gov/feature/goddard/2018/science-on-the-cusp-sounding-rockets-head-north and originally provided by Andøya space center/Trond Abrahamsen

and so the ionospheric region near magnetic noon was separated into a "cusp proper" and "cleft/boundary layer" (see Keith et al. (2005) and references therein, in particular Heikkila (1972) and Reiff (1979)). The difference between the two is this: the cusp proper (despite being a 3-D region) is taken to be the area in which magnetosheath/solar wind plasma enters the ionosphere essentially unperturbed, that is without being accelerated – and so is modified only by changes in the solar wind, while the cleft describes a similar population of electrons and protons, but structuring in the precipitation (temporal or spatial) may be present due to various acceleration processes (some examples may be inverted-v structures, velocity/time dispersion, etc). As understood by Heikkila (1985):

> The cleft is the low altitude region around noon of about 100 eV electron precipitation associated with 630.0 nm emission, but containing also structured features of higher energy. The cusp is a more localized region near noon within the cleft characterized by low energy precipitation only, having no discrete auroral arcs, often displaying irregular behavior, presumably associated with the magnetic cusp.

In order to demonstrate that the cusp and cleft were in fact two morphologically different regions and provide criteria for distinguishing between the two, Newell and Meng (1988) examined one year's worth of DMSP F7 electron and ion data, comprising 5,609 individual passes of the spacecraft through the dayside cusp/cleft region. The following four criteria are taken directly from Newell and Meng (1988):

1. If the energy flux of the ions (electrons) was less than 10^{10} eV/cm^2 s sr ($6x10^{10}$), the region was neither cusp nor boundary layer
2. If the energy flux in the 2- or 5-keV electron channel was greater than 10^7 eV/cm^2 s sr, the region was neither cusp nor boundary layer, since such fluxes would indicate plasma sheet presence.
3. If the first two criteria were met, the region was boundary layer if either 3000 eV $<$ E_i $<$ 6000 eV or 220 eV $<$ E_e $<$ 600 eV where E_i and E_e are the average electron and ion energies, respectively.
4. If the first two criteria were met and both 300 $<$ E_i $<$ 3000 eV and E_e $<$ 220 eV, the region was identified as cusp.

These criteria defined what is known as the "cusp proper" or the low altitude (1000 km and below, i.e. the ionosphere) region where plasma flux most closely resembles that which is found in the magnetosheath, which implies that there are little to no acceleration processes operating to alter the particle spectra. What this means for us is that the cusp proper is a more constrained region poleward of the cleft (Keith et al., 2005).

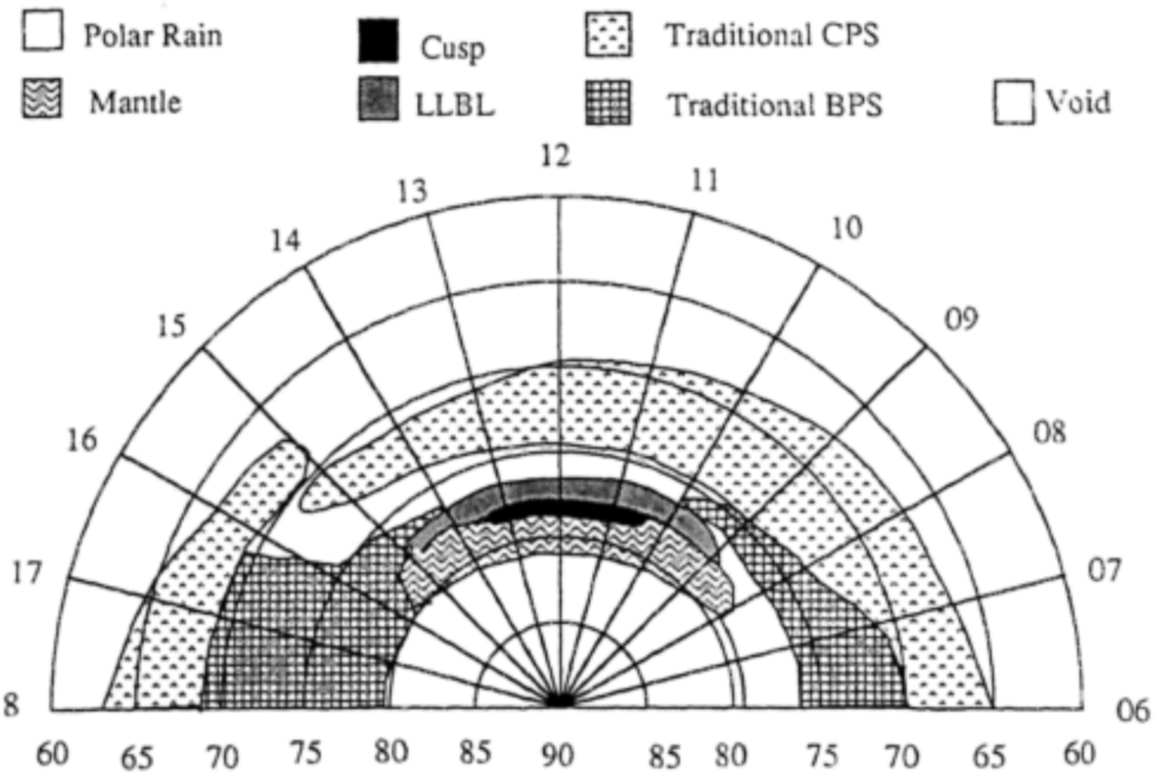

Figure 7: The location of the cusp based on a statistical study of precipitation by Newell and Meng (1992) (also the source of the figure). The cusp is the indicated by the black portion of the figure. The area keyed as the LLBL is the cleft. The diagram displays the magnetic latitude along the bottom of the figure and the magnetic local time along the circular boundary. The keyed regions are labeled and show the projection onto the dayside polar region of auroral precipitation as it maps from the respective source location.

While the cusp proper is a continuous structure Keith et al. (2005) its location and extent varies with IMF conditions, but the general area and extent of the cusp can be seen in Figure 7. IMF B_z controls the latitudinal variation, while IMF B_y controls the longitudinal variation. When IMF B_z goes more negative, the northern hemisphere cusp is pulled equatorward. As IMF B_y increases in magnitude, the cusp stretches duskward (Keith et al., 2005). Reversing the sign of these changes reverses elongation or location change.

Understanding the differences between the cusp, "cusp proper" and cleft are important, as different physical processes operate within the bounds of the regions. There is little distinction made in much of the literature of the past two or so decades (see, for example, Pfaff et al. (1998), Tanaka et al. (2005) which refer to cusp precipitation but report electron acceleration structures). This leads to confusion as there has been a significant amount of work done in reporting on the dynamics of the cusp and cleft. It is important to the scientific process to use clear and concise language which can be difficult to do when studying overlapping regions which do not have a hard boundary. It is also of course important to not allow pedantry to obstruct the scientific process, and we should not dissuade a changing understanding of the dynamics in these two regions based only on the chosen language. Rather, this lengthy discussion of pedantry and pedagogy is included here in order to keep a historic perspective on the understanding of these studies. The goal of including this historic perspective is to help allow for ongoing and future work to add to our understanding of prior observations rather than put past and present at odds with one another. From here forward, I will refer to the cusp, cusp proper and cleft simply as the cusp – as is the trend in modern studies of the regions.

4.1 Upwelling and Neutral Density Enhancements

As a result of its relatively small size and the direct access to solar wind plasma, the cusp region of the Ionosphere-Thermosphere system features a high concentration of energy dissipation. That energy dissipation means that the ionospheric cusp is one of the largest sources for ion outflows into the magnetosphere, and the thermospheric portion of the cusp exhibits large neutral density enhancements (Varney and Zhang, 2017). These two topics motivate many cusp studies. Ionospheric outflow has important implications for processes further out in the magnetosphere, such as mass loading at the magnetotail and enhancement of the ring current (Welling et al., 2015; Moore et al., 2014).

Neutral upwelling has implications for satellites in orbit which experience more drag when encountering a more dense atmosphere.

4.1.1 A note on language

It can be seen in the literature that there is not yet a unified set of terms regarding the processes of ions and neutrals increasing in scale height or escaping the influence of Earth's gravity. Briefly, here are the terms used and their meaning. Upwelling refers to either plasma or neutrals which have increased in scale height (i.e., have increased in energy due to heating and expanded upwards) but not gained enough energy to escape Earth's gravity. Upflow is also used interchangeably for this process. In the case of neutrals which have undergone upwelling/upflow the region is often referred to as a "neutral density enhancement." Outflow refers to plasma which has gained enough energy such that it has achieved escape velocity. Typically, this is presented as a two step process, where the first step is upflow. Once at increased scale heights, secondary processes (commonly considered to be wave-particle interactions Strangeway et al. (2005)) can further energize plasma and cause outflow. Neutrals do not typically, at least in any quantity to be studied – gain enough energy to outflow. Neutrals or plasma which have upwelled but not gained enough energy to outflow will eventually cool/lose energy and undergo downflow.

4.1.2 Processes driving upwelling and outflow

Outflow is generally considered to be a two step process, the first step of which is upflow. Ion upflow can be driven in two different ways: joule dissipation and electron heating Strangeway et al. (2005). Upflow which results from joule heating is referred to as Type I, while upflow which results from electron heating is referred to as Type II.

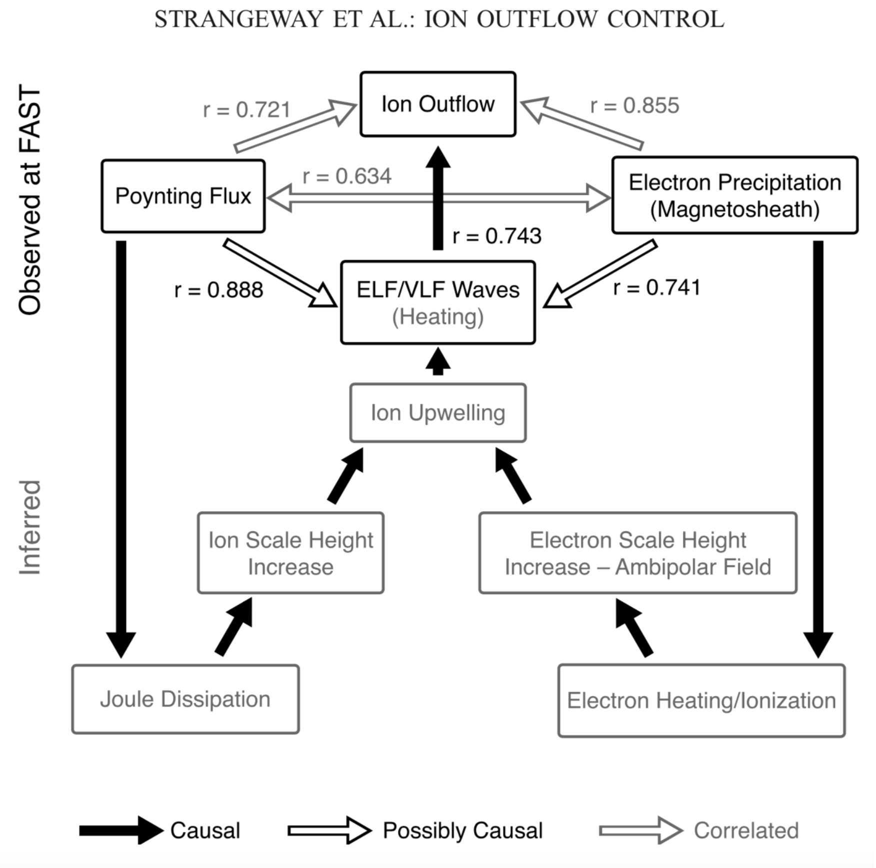

Figure 8: Figure from (Strangeway et al., 2005) which outlines the relevant processes for ion upwelling and outflow. The relationship between ion outflows and the energy inputs behind them are indicated by the arrows.

Heating through joule dissipation occurs as plasma flows through the neutral thermosphere or vice á versa (see section 3.2). As it specifically pertains to upflow, joule heating will primarily increase the temperature of the minority species (Strangeway, 2012). For the ionosphere, this almost always means that the ion population is heated more strongly than the neutrals, as the neutral density is generally higher than the plasma density (see, Figure 3).

Type II upflow is driven by soft electron precipitation. Here, the ambient electrons in the ionosphere are heated by soft (meaning 100s eV scale) electrons. Such soft electrons are sourced through auroral precipitation – though Chapter 7 will discuss a different source for soft electrons. This causes the ambient electrons to increase in scale height, which sets up an ambipolar field and lifts the ion population. To drive neutral upwelling through this process, the electron precipitation would have to either heat the neutrals directly through collisions (inefficient) or the upwelling ions drag neutrals upwards with them (transfer of momentum). Type II outflow is thought to be the majority type of upflow events in the cusp (Moen et al., 2004).

4.1.3 Cusp Aurora

The soft electron precipitation in the cusp region forms a particular auroral signature referred to in the literature as cusp transients or more precisely Poleward Moving Aurora Forms (PMAFs). As the name implies, PMAFs form at the equatorward edge of the ionospheric cusp and drift poleward over the course of roughly 10 minutes. Often times, PMAFs are not solitary events but repeat with 3-15 minutes in between structures (Lockwood et al., 1989) considered to be the ionospheric signature of Flux Transfer Events (FTEs) sent off by pulsed reconnection at the magnetopause (Sandholt and Farrugia, 2007). PMAFs are most commonly observed between 0900 and 1500 MLT (i.e. the dayside cusp) (Lockwood et al., 1989).

The electron precipitation which comprises a PMAF is sourced from the magnetosheath (Mende et al., 2016). However, the precipitation can at times be highly structured and exhibit fine scale signatures indicative of electron acceleration (Tanaka et al., 2005; Pfaff et al., 1998; Mende et al., 2016; Arnoldy et al., 1996). Some observations such as Pfaff et al. (1998); Arnoldy et al. (1996); Tanaka et al. (2005) have reported inverted-v type structures, commonly associated with large scale potential structures (Newell et al., 2009). More commonly, fine scale structure within cusp aurora are attributed to electron acceleration via Alfvén wave interactions Moen et al. (2004); Chaston et al. (2003); Chaston et al. (2005).

CHAPTER 5

The Aurora

The aurora has long captured the imagination of humans. The earliest recording of an auroral sighting dates back to 2600 B.C. in China:

> Fu-Pao, the mother of the Yellow Empire Shuan-Yuan, saw strong lightning moving around the star Su, which belongs to the constellation of Bei-Dou, and the light illuminated the whole area.

Cave paintings may also have depicted auroral phenomena as early as 30000 B.C. (Dunbar, 2006). It is not difficult to imagine how mysterious, colorful and moving lights in the sky were the inspirations for mythologies and legends.

Though today we understand that the cause of these lights are not supernatural portends of doom they are still of great scientific interest. While the lights themselves have little impact on human life, the interaction with our near space environment and energy transfer from the solar wind, through the magnetosphere, ionosphere and thermosphere system have consequences for a technological society.

5.1 Auroral emissions

At the very basic level, the aurora occurs when protons and/or electrons collide with Earth's atmosphere. The emission of light is due to the release of energy when an ion captures a free electron or when an excited atom or molecule relaxes back to a low energy state. Many of these emissions are visible to the human eye; 630.0 nm (red), 557.7 nm (green) and 427.8 nm (blue) are all common auroral emissions. The aurora is not limited to the visible spectrum and does appear in ultraviolet and even the x-ray portion of the spectrum (Grodent, 2015; Anderson, 1960).

The different emission lines are indicative of different molecular and/or atomic species being excited. There are also different height profiles for auroral emissions. Due to the lack of turbulent mixing above the turbopause, the various emission lines will have heights where they are more effectively excited. For example, red line emissions (630 nm) being an atomic oxygen line is excited in a relatively extended region from 150 km upwards beyond 400 km – with the lower boundary being a result of atmospheric quenching (Gillies et al., 2017). Green line emissions (557.7 nm) on the other hand are more constrained in altitude from a lower limit of 95 km upwards to 150 km (Gillies et al., 2017). Typically, auroral emissions do not occur lower than about 95 km due to atmospheric quenching, however in the case of hard (10s of keV up to 100 keV) electron precipitation, lower altitudes are possible (Brown et al., 1976).

The aurora can be seen from sufficiently northern or southern latitudes year round, provided it's dark enough to see the emission. The ring of latitudes in which the aurora occurs is called the auroral oval. It is on the order of a few degrees in latitude across and typically within 10 - 20 degrees of latitude from the pole, with a skew such that the day side (i.e. sun-facing) side of the oval is around 10 degrees in latitude closer to the pole than the night side (Feldstein, 1986).

5.2 Types of aurora

The aurora occurs in a myriad of different visual forms which appear in different colors, shapes, sizes and behaviors. These various auroral forms are indicative of the dynamics and source regions of the incident particles.

5.2.1 Discrete Aurora

The discrete aurora is what typically comes to mind when picturing aurora. Visually, these appear as distinct, ribbon-like arcs which stretch across the sky. They are often dynamic and will move, spiral, curl, fold, bulge, ripple and brighten – all behaviors indicative of different physics at play. The discrete aurora are more pronounced pre-midnight and occur at the poleward boundary of the auroral oval, on field lines which map to the plasma sheet boundary layer in the magnetotail. The energies of the precipitating electrons are typically on the order of hundreds of eV up to around 10 keV (Arnoldy, 1981; Newell et al., 2009). The electron precipitation most commonly associated with discrete aurora is called "inverted-v" precipitation due to it's appearance when the spectra is plotted with energy as a function of time. It appears as a narrow band of energies which exhibit an enhanced particle flux over the background starting at a low energy and "ramping up" to a maximum in energy and then decaying back to lower energy which forms an upside down "V" shape on a plot. Although this gradual ramp up and ramp down behavior is the namesake of the spectra, it does not always appear (Newell, 2000) and instead inverted-v (also called monoenergetic) accelerations may instead show very sharp edges and/or a flat line across the peak energy (rather than a sharp point as inverted-v would denote). In any case, such monoenergetic aurora are associated with quasi-static electric fields which exist aligned with the magnetic field line and have sharp gradients at the edges of the of the spectral signature, indicative of large electric fields (Newell et al., 2009).

Electron spectra of discrete aurora may instead exhibit broadband acceleration. In this case, the aurora is sometimes referred to as "Alfvénic" as they are accelerated by means of interactions with Alfvén waves (often called KAWs or DAWs for kinetic or dispersive Alfvèn waves) as has been demonstrated by Ergun (1998); Chaston et al. (2003, 2004, 2007).

Figure 9: An example of discrete aurora. Note the defined, rayed structure of the arc. Photo from wikimedia commons `https://en.wikipedia.org/wiki/Aurora#/media/File:Aurora_Borealis_and_Australis_Poster.jpg`

5.2.2 Diffuse Aurora

The diffuse aurora, as the name suggests, is a less visually stunning phenomenon and appears often as almost as a haze of color in the sky. Diffuse aurora occurs over a large range of latitudes but is most prevalent towards the equatorward side of the auroral oval. It is caused by precipitation of electrons from the central plasma sheet which undergo pitch angle diffusion (Khazanov et al., 2017). Typical electron energies for diffuse aurora range from 100s of eV up to "a few" keV (Arnoldy, 1981). Despite the diffuse aurora appearing less dynamic, it has been shown that it constitutes a larger portion of the incident energy flux into the ionosphere than discrete aurora (Newell et al., 2009).

Figure 10: An example of diffuse aurora, which appears as a glowing haze in the sky. Photo credit: Bob King, Universe Today, `https://www.universetoday.com/103414/auroras-dance-over-northern-u-s-last-night-may-return-tonight/amp/`

While it is understood that the source ions and electrons of the diffuse aurora are sourced from the plasma sheet, the means by which the plasma sheet source is replenished is an open question (Newell et al., 2009).

5.2.3 Pulsating Aurora

Pulsating aurora is a commonly occuring phenomenon which manifests as patches of aurora with a periodic variation in luminosity. Typical periods of modulation are from 2 to 20 seconds wiht 8 seconds being the average (Royrvik and Davis, 1978). The patches may be abundant, and have different periods of variation with brightness in the range of hundreds of Rayleighs to a few kiloRayleighs in the 427.8 nm emission line. Pulsating aurora is not to be confused with flickering aurora, which is also a modulation of the luminosity of an auroral though on a much faster time scale of 6-8 Hz (Jones et al., 2011). Various studies have shown that patches of pulsating aurora do or do not E cross B drift, there seems to be no singularly correct distinction, suggesting that different processes may be at work. Grono and Donovan (2018) notes that pulsating aurora with a rapidly changing structure will expand/contract/change shape without regard for the E cross B direction. Pulsating aurora can be highly varied in size, shape, patch velocity and lifetime. Grono and Donovan (2018) separates pulsating aurora into three categories based on their shape and pulsating behavior as follows:

1. Patchy aurora: characterized by stable structures with pulsations limited to small a region.
2. Patchy pulsating aurora: a number of stable structures which appear near each other and exhibit pulsating behavior which is less subtle i.e. brighter, or in a larger region.
3. Amorphous pulsating aurora: regions of pulsating aurora which change shape, often rapidly and often without regard to the $E \times B$ drifting of plasma

Pulsating aurora events occur primarily in the morning side of the auroral oval and last on average 1.5 hours (Jones et al., 2011) although pulsating aurora have been observed to last up to 15 hours (Jones et al., 2013).

The primary electrons which comprise pulsating aurora are sourced from the interaction of chorus waves near the magnetic equator, which scatter the electrons into the loss cone (Kasahara et al., 2018). It is not currently known what processes transports plasma to re-fill these lost electrons.

The typical energies of the electrons in pulsating aurora are on the order of 10s of keV up to 100 keV (Brown et al., 1976; Miyoshi et al., 2015; Partamies et al., 2017), although in some cases energy scales on the order of 1 keV have been reported (McEwan et al., 1981) though such low energies do seem outliers for primary precipitating energies. Work by Evans et al. (1987) demonstrated that some lower energy electrons (hundreds of eV scale up to singular keV scale) may be found in pulsating aurora as well in the form of secondary, or backscatter electrons. Recent work by Samara et al. (2017) has suggested that some of the periodic intensifications seen in pulsating aurora are from secondary or backscatter electrons which precipitate from the opposite hemisphere or mirror and re-precipitate.

5.2.4 Black Aurora

Black aurora is not an auroral emission but strictly a morphological phenomenon embedded in diffuse or pulsating aurora which appears as a well defined region which lacks aurora entirely or has a low enough emission intensity such that it appears black compared to the surrounding aurora (Royrvik and Davis, 1978; Davis, 1978). There are several theories as to the cause of black aurora. Marklund et al. (1994) used electric field measurements from the Freja satellite which show intense, divergent electric field structures as a result of positive space charge in conjunction with black aurora and conclude that black aurora is a region of electrons traveling back up the field line (i.e. a return current structure). However, these same electric field structures may also be attributed to standing Alfvén waves (Weimer and Gurnett, 1993). Still other theories attribute black aurora to a localized suppression of pitch angle scattering at the plasma sheet (Peticolas et al., 2002) or a relaxation of a plasma pressure enhancement near the plasma sheet inner boundary (Sakaguchi et al., 2011).

5.3 Geomagnetic Storms and Substorms

Periods of exceptionally active aurora are known as storms, a terminology that dates back to the 1800s when humans first began taking a scientific interest in the aurora. Geomagnetic storms are identified and categorized by their disturbance of Earth's magnetic field. Such a disturbance is caused by an increase in the ring current. A ring current enhancement may start with a sudden impulse of an interplanetary shock structure (such an occurrence is called a storm sudden commencements), though this is not always the case and not required for a geomagnetic storm to occur (Gonzalex et al., 1994). Geomagnetic storms are identified and categorized based on how far they depress the horizontal component of the magnetic field recorded by magnetometers in low latitudes. For such systems, the 3-D coordinate convention is H, Z, D where H is the horizontal component, Z the vertical and D the dip-angle i.e. the angle between the local magnetic field line and H. The first such study of storm onsets in an attempt to categorize geomagnetic storms was performed by Sugiura and Chapman (1961) who identified 346 sudden storm commencements and by examining the daily mean values of the horizontal field at 26 different middle and low lattitude sites and broke the storms into three categories of weak, moderate and great. Today, this concept of using low latitude ground based magnetometer data as a proxy for the ring current intensity has been formalized into the Disturbance Storm Time, or D_{st} index. D_{st} ranges from about +100 nT to -600 nT, with quiet conditions being typically near zero; though long term ring current enhancements can occur which cause D_{st} to hang around -10 to -20 nT for years at a time (Gonzalex et al., 1994). D_{st} categorizes storms as Intense (-100 nT or more) Moderate (-50 nT) or Small (-30 nT).

Geomagnetic storms are divided into three phases; an initial phase, main phase and recovery phase (McPherron, 1997). During the initial phase, D_{st} increases to positive values; this may occur on timescales froma minutes to hours. The magnetopause is compressed inward during this time. The main phase sees a drop in D_{st} (the minimum of the drop categorizes the storm as intense, moderate or small). The drop in D_{st} occurs as a result of an increase in the population of particles in the ring current, though the cause of that increase is up for debate (McPherron, 1997). During the main phase, cross-tail electric fields cause the plasmapause to move closer to Earth and the outer layers of the plasmasphere to erode. The recovery phase is the longest phase, lasting tens of hours to weeks of time in which the ring current population decays, causing the D_{st} index to return to pre-storm levels.

The concept of the substorm was developed predominantly by both Chapman and Akasofu in the early part of the 1960s, with Chapman coining the term "polar substorms" in 1962 (McPherron, 1997). Akasofu (1964) developed the first morphological model of substorms (he would call them "auroral substorms") by separating them into the expansion and recovery phases which were denoted by distinct morphologies of the auroral arcs which were visible. These two phases would later become three phases as the idea of the substorm being a polar phenomenon morphed into a more encompassing magnetospheric phenomenon. The three phases are the same as for a storm but the timescale differs; growth, expansion and recovery which as a whole occur over the course of 1-3 hours and may repeat several times in a night of observation (Rostoker et al., 1994; Akasofu, 1964). During a substorm, very bright and structured aurora are visible – when we see photos of extravagant auroral displays, we are most likely seeing pictures taken during substorms.

The substorm growth phase can be thought of as a storing of energy which then gets released during the expansion phase. The growth phase is driven by the solar wind and begins when the interplanetary magnetic field (IMF) turns southward, causing reconnection on the dayside and enhancing the convection electric field. Solar wind energy gets transferred from the dayside to the nightside into the magnetosphere through the reconnection process (see Figure 1). On the ground, the aurora during the growth phase appears as a quiet, diffuse arc oriented east-west and drifting slowly southward. Out in the magnetosphere, the tail lobe field strength increases which compresses the plasma sheet near Earth (Fairfield and Ness, 1970; Fairfield et al., 1981). The cross tail current also increases during this phase, causing the magnetic field lines in the tail to become elongated, i.e. pulled further tailward (this is known as the tail-stretching phase) (Kaufmann, 1987).

The beginning of the expansion phase is marked by a sudden increase in brightness of the quiet arc and subsequently a rapid motion of the arc poleward (Akasofu, 1964). This marks the substorm onset. If the substorm is "weak" the poleward motion may only last a few minutes and other arcs which may be present may not be affected. However, in a "stronger" (or what may be viewed as a more canonical) substorm, the brightening of the most southward arc and subsequent poleward motion is accompanied by other arcs forming N-S aligned folds, the result of which appears as a bulge expanding poleward as well as east and west (Akasofu, 1964). The termination of the expanding bulge appears as a brightening which travels from east to west, called the westward travelling surge.

Out in the magnetosphere during the expansion phase, plasmoids – fast tailward plasma flows with slower north-then-south turning B_z signatures are observed. These are consistent with theories regarding tail reconnection, though unconfirmed (Eastwood and Kiehas, 2015). In some cases of rapid north-turning-south events are associated with anti-dipolarization fronts (Li et al., 2014). High speed plasma flows also occur in the Earthward direction as the field relaxes to a more dipolar configuration (i.e. dipolarization; in which the B_z component grows). The previously enhanced cross tail current diminishes as the substorm current wedge forms. The substorm current wedge forms when the cross tail current gets disrupted and connects through field aligned currents (FACs) into and out of the ionosphere (Kaufmann, 1987). Some of those currents are dissipated in the ionosphere as part of the auroral electrojet system (Luehr and Buchert, 1988). Importantly, it is during the growth phase when electrons with 10s of keV scale energies are injected into the near-Earth tail (Arnoldy and Chan, 1969). For a long time, it was thought that the relationship between storms and substorms was that a storm was a sum of many substorms which composed it. In this framework, it was conceptualized that substorms caused the injection of particles leading to a longer term enhancement of the ring current,

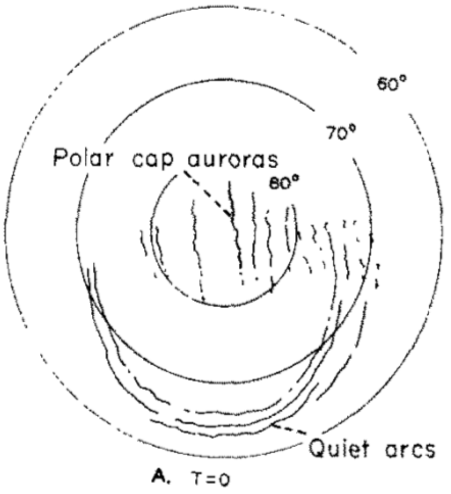

FIG. 2. THE DISTRIBUTION OF THE AURORAS DURING THE QUIET PHASE.

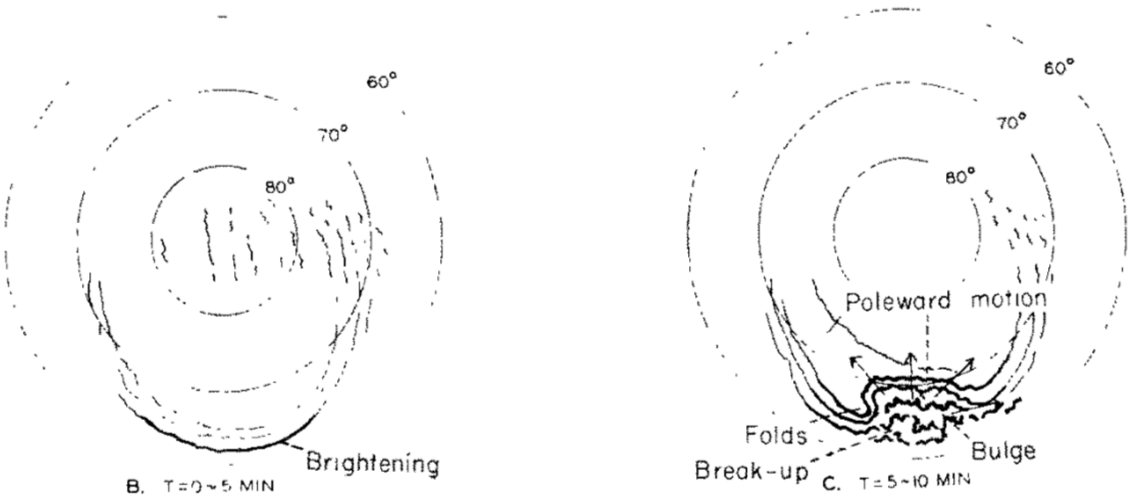

FIG. 3. AURORAS DURING THE EXPANSIVE PHASE (STAGE I).

FIG. 4. AURORAS DURING THE EXPANSIVE PHASE (STAGE II).

Figure 11: Hand drawn sketches depicting the appearance of aurora during a geomagnetic storm from Akasofu (1964). The top image (labeled fig. 2) shows the overall structure of the aurora during the quiet phase. The bottom plots show the typical location of the brightening of an arc marking the beginning of the expansion phase (fig. 3), followed by the formation of the poleward-expanding bulge (fig. 4).

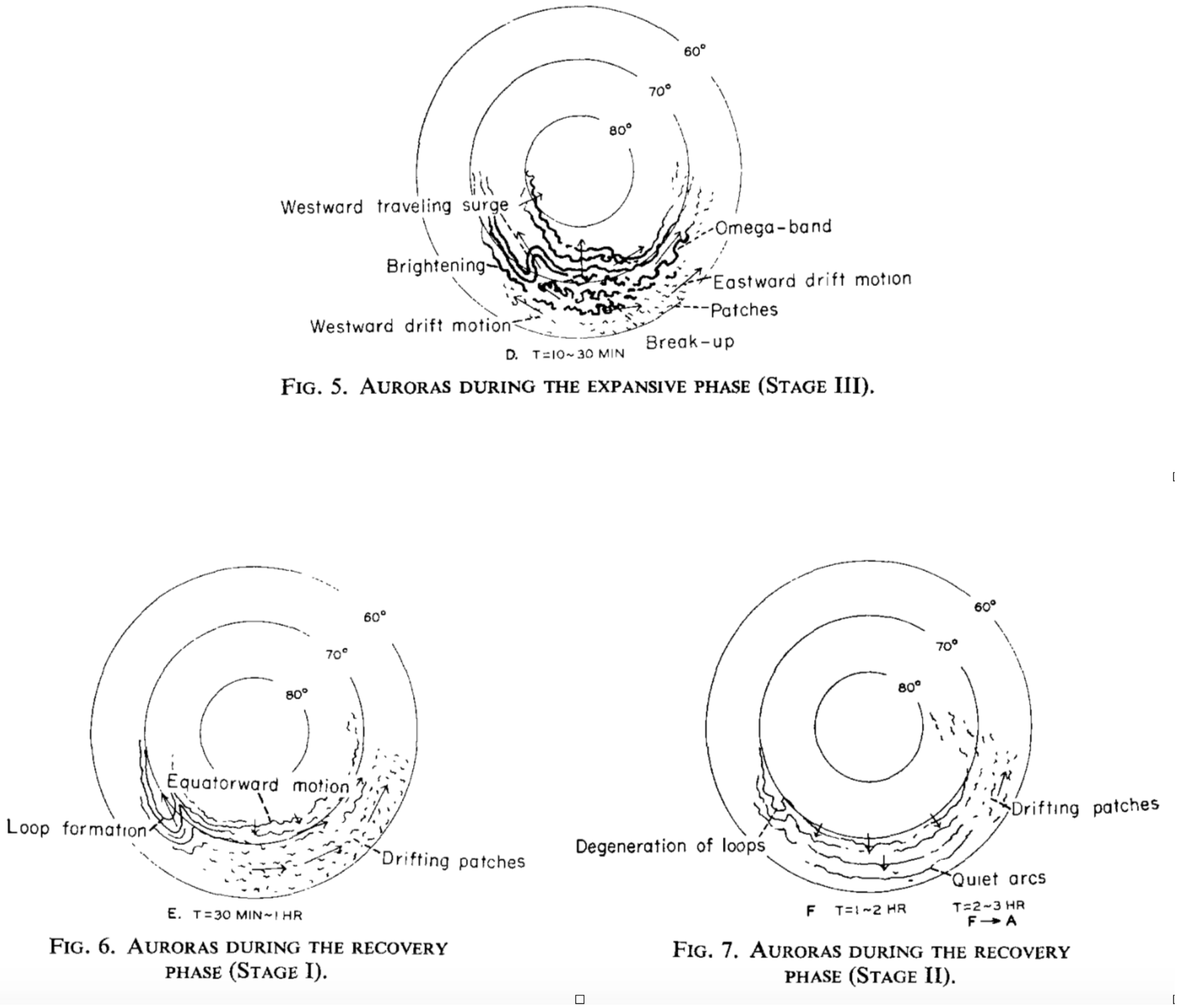

FIG. 5. AURORAS DURING THE EXPANSIVE PHASE (STAGE III).

FIG. 6. AURORAS DURING THE RECOVERY PHASE (STAGE I).

FIG. 7. AURORAS DURING THE RECOVERY PHASE (STAGE II).

Figure 12: A second set of hand drawn sketches depicting the appearance of aurora during a geomagnetic storm from Akasofu (1964). These depict the more complex auroral forms during the expansion phase through to the breakup and recovery phase.

thus providing the impetus for a long term negative displacement of D_{st} (i.e., a storm). At present, the connection between storms and substorms is not so distinct and not settled within the community; as studies such as (McPherron, 1997) have demonstrated that substorm onsets and decreases in D_{st} are not well correlated.

Following the expansion phase, the recovery phase is a return to the pre-substorm state. Often, another substorm will directly follow Akasofu (1964). A typical recovery phase is on the order of an an hour and half, during which time the substorm current wedge dissipates McPherron (1997). Bright bands of aurora which comprised the westward travelling surge move out of sight and are replaced with drifting patches, pulsating aurora and omega bands. Diffuse or quiet arcs will drift slowly more equatorward and the bulge is diminished. In general, as recovery phase proceeds, the aurora become less distinct and less visibly intense Akasofu (1964).

CHAPTER 6

Instrumentation

Throughout the course of my time in the Magnetosphere - Ionosphere Research Lab I have had the opportunity to work on many different instrumentation projects. These have spanned a range of instrument types, both rocket-borne and ground based. I have been involved with the deployment of a ULF magnetometer system to Gakona, Alaska and the retrieval of one of these systems from Sondrestrom, Greenland. On the rocket side of things, I have worked on instrumentation for the RENU2, ISINGLASS, SUBTEC8, LAMP, CREX2 and KINETX campaigns. For these campaigns, I have been involved in the construction of the High Energy Electron Plasma (EPLAS, HEPLAS) instruments, the thermal Electron Retarding Potential Analyzer (ERPA) and the newly designed Cylindrical Electron Retarding Potential Analyzer (CERPA). The CERPA instrument is a brand new design. Since I have seen this new instrument through from its design and testing phase through its first flight, I have elected to include a thesis chapter detailing the purpose, design and construction of the instrument. My role throughout the development of the instrument was to serve as sort of systems engineer – a go between for the mechanical and electrical engineers (Mark Widholm and Dominic Puoppulo). I developped the process for appling the screens to the frames, and oversaw both torque and vibrational testing. I also performed the build for both CERPA instruments flown on SUBTEC-8.

6.1 CERPA concept

Sounding rockets are a vital tool for the study of the Magnetosphere - Ionosphere - Thermosphere system. For a comparatively low cost, they are a flexible platform on which a wide array of instruments can be deployed to make high resolution in-situ measurements. The downsides of a sounding rocket mission is that they are short lived; with flight times on the order of 15 minutes and they can only obtain in-situ data along one spatial dimension (the flight path). Recent efforts are pushing these limitations however; in particular the development of small payloads ejected from a sounding rocket in order to take data in a distributed array. This provides valuable data in two spatial dimensions, enabling studies which probe at more fine scale structures within the ionosphere. The development of such payloads has been named a priority by the NASA sounding rocket program. The CERPA instrument was designed in order to meet this demand and provide a crucial measurement of electron temperature, with the flexibility to add a small ion detector or fluxgate magnetometer to the ejectable platform as well.

6.2 Principle of operation

The CERPA is a retarding potential analyzer (Serbu, 1964). Retarding potential analyzers have a long history of use in ionospheric studies Knudsen (1966). The operating principle for such an instrument is simple; by placing a fine mesh screen in front of an anode and biasing the screen with a known voltage, particles without the energy required to pass that voltage are rejected away from the anode. Particles with enough energy to pass through the voltage are collected on the anode and read out as a current. The bias voltage applied to the screen is swept and in doing so, the current collected on the anode at each step is counted to create an incident spectrum of particles (which may be either electrons or ions in general; for the case of the CERPA we are interested in the electrons).

The primary data product of the CERPA is the electron temperature of the surrounding ionosphere. This is measured by performing two voltage sweeps on the bias screen, during which the current on the anode is recorded for the ramp up and ramp down in voltage and averaged. Ffrom Langmuir theory in which the probe potential is less than the plasma potential then only a fraction of the electrons in the plasma can overcome that potential difference and access the probe (Cohen et al., 2016). This results in a current on the anode which is then:

$$I(V) = -Aen_e\sqrt{\frac{2k_BT_e}{m_e}}Exp(\frac{e(V-V_p)}{k_BT_e}) \tag{6.2.1}$$

where A is the area of the collecting surface, n_e is the electron density, k_B is the Boltzmann constant, m_e is the electron mass, e the electron charge, V the voltage of the sweep, V_p the plasma potential, and T_e the electron temperature. Effects of ram are neglected due to the high thermal velocity of the electrons. This then means that the high energy tail of the differential energy spectrum follows the Maxwellian expression above. Taking the log of the current and differentiating with respect to the voltage we obtain

$$\frac{dlnI}{dV} = \frac{d}{dV}(ln(-Aen_e\sqrt{\frac{2k_BT_e}{m_e}})(\frac{e(V-V_p)}{k_BT_e})) = \frac{e}{k_BT_e}. \tag{6.2.2}$$

This expression is equated to the slope of the line of best fit obtained by fitting the high energy tail of the differential energy spectrum, allowing T_e to be solved for.

6.3 Instrument Design

The CERPA instrument has three main physical constraints which led to the current design. The first constraint sets the physical size of the instrument. To fit into the ejection housings the instrument must be 3.4 inches in diameter and no longer than 6.205 inches in length. This volume must contain the entirety of the instrument and electronics for the instrument. It mates to the portion of the ejectable payload which contains batteries, telemetry, radios for communicating back to the main payload, and the rocket motor

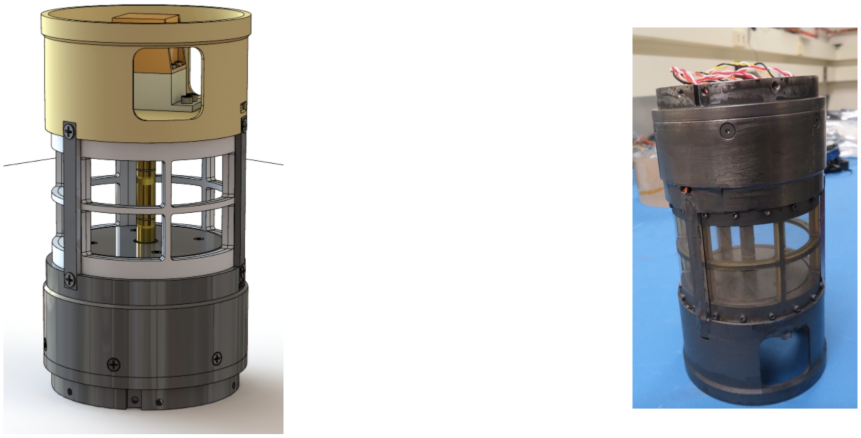

Figure 13: Comparison of a 3-D model of a CERPA to the fligth unit. Note that the 3-D model is upright, but the actual unit is upside down in the picture due to the wiring which must be attached to the motor, telemetry and power supply portion of the payload provided by Wallops. Model and picture of actual unit are both courtesy of Dominic Puoppulo. The flight unit on the right has all surfaces, including the ultem cap coated with Aerodag to minimize effects of spacecraft charging. Wiring visible in top of picture on flight unit are connections to the support portion of the payload.+

which propels the ejectable (this will be called the support portion for further discussion). The second constraint then is that the instrument must be robust enough to survive the impulse of being rapidly accelerated out of the ejectable housing. The housing is rifled to impart a spin stabilization onto the ejectable. Previous experiments with ejectables have had failure modes in which the shear of this angular acceleration causes the mating between the instrument and support portion to fail. In order to mitigate this, the design used an aluminum housing and support struts for structure with ultem for as much of the body of the instrument as possible. This keeps the mass of the instrument lower and results in a lower net torque when the payload is ejected. The third constraint on the design is that the aperture must be cylindrical to allow a continuous view up the local field line while the payload spins and that aperture area must be maximized to provide the best possible counting statistics. This constraint is counter to the need for a robust instrument and so the two must be balanced.

The torque experienced by the CERPA is given by

$$\tau = I\alpha \tag{6.3.1}$$

where I is the roll moment of inertia and α is the angular acceleration. The final spin rate for the ejectable as flown on SUBTEC-8 was 4.6 Hz. The method of ejecting the instrument from its rifled housing yielded a fast spin-up time of only 0.04 seconds and thus an angular acceleration of 722 rad/s^2. The roll moment of intertia for the entire ejectable payload (including the support portion provided by NASA Wallops Flight Facility) was $2.445 \times 10^{-3} kg/m^2$. This yields a maximum torque of 1.8 Nm (1.3 ft lbs).

In order to test the performance of the instrument under torque, an experiment was performed on the lab bench with the engineering unit. The engineering unit was composed of a metal base, two concentric layers of frames with screens and a solid delrin cap (rather than a hollow ultem cap piece). Three aluminum struts between the base and the cap identical to those on the flight unit were also utilized. The engineering unit was place firmly in a vice bolted to the lab bench. A rope was wrapped twice around the cap piece and held in place with gorilla tape which did not allow for slipping of the rope around the cap when weight was applied. The rope was fed through a pulley such that the torque was applied perpendicular to the radius of the delrin cap. Weight was hung freely from the end of the rope and the engineering unit was visually inspected for signs of failure. Under these conditions, weight was applied up to 3.56 Nm, nearly twice the expected maximum. The engineering unit demonstrated survivability, though some deflection of the frames was noticed. The frames themselves returned to their non stressed state once the torque was removed. The screens appeared more visibly wrinkled, but still adhered to the frames.

The resulting design is depicted in Figure 13. A major challenge to the construction of the CERPA is the use of fine mesh screens over a curved surface. The screen material used is an electroformed nickle mesh with 268 μm spacing and 14 μm line width which allows for a high transmittance percentage (90%) of incident electrons. This screen material must be affixed to two concentric layers of ultem frames. Each layer of ultem frames are in three independenct sections. The exterior layer screens must be held at payload ground, while the interior frames must be swept in voltage and so isolated from the exterior layer. Each screen must be affixed to the ultem frame as smoothly as possible in order to ensure the most uniform electric field possible. Ideally, the electric field between the inner screen layer and the anode would be perfectly radial. Any wrinkle in the screen will cause a deviation from the radial field and can cause focusing/de-focusing problems for the instrument, so care must be taken in fixing the screens to the frames to avoid wrinkling the screen material.

6.4 Spacecraft Charging

Spacecraft charging occurs when the flux of incident ambient electrons exceeds the flux of incident ambient ions onto the surface of the spacecraft. This can be expressed as

$$n_e v_e > n_i v_i \tag{6.4.1}$$

where n_e and v_e are the electron number density and velocity and n_i and v_i are the ion number density and velocity. This inequality will be met for any object placed into an ambient plasma, though our primary concern is the consideration of an ionospheric plasma for the CERPA. In the ambient, unperturbed ionosphere we can make the assumptions of quasi-neutrality and equipartition of energy such that

$$\frac{1}{2}m_i v_i^2 = \frac{1}{2}m_e v_e^2 \tag{6.4.2}$$

where m_i, v_i, m_e, v_e are their usual quantities. As an "order of magnitude" approximation, we can solve the above equation and arrive at

$$43 v_i = v_e \tag{6.4.3}$$

if we make the assumption that our plasma is simply composed of electrons and protons. This illustrates that the condition given for spacecraft charging is likely to be met, as the velocity of the electrons is significantly higher than that of the ions, and thus our spacecraft will contact a greater flux of electrons than ions and gain a net negative charge and thus have a negative potential difference compared to the background plasma.
The approximation above relies on

$$k_B T_i = k_B T_e \tag{6.4.4}$$

This expression comes from the distribution function

$$f(E) = n\left(\frac{m}{2\pi k_B T}\right)^{\frac{3}{2}} Exp\left(\frac{-E}{k_B T}\right) \tag{6.4.5}$$

which takes the form of a Maxwellian. Taking the logarithm of this expression and plotting it as a function of energy yields a plot with a slope of -1/$k_B T$. This is in fact how the electron temperature is derived from the CERPA. The difficulty with spacecraft charging is that when the payload surface charges to some negative potential ϕ_s, then (once an equilibrium is reached) ions will be pulled in and gain energy equivalent to $e\phi_s$, while electrons will be repelled and lose the same amount of energy. If we plot this effect for ions, this yields an offset spectrum where there is a gap in data between 0 and $e\phi_s$ (i.e. all ions are still recorded, but the lowest energy recorded is $e\phi_s$). In the electron case, those which do not possess a thermal energy greater than $e\phi_s$ are repelled and simply not recorded. Because the CERPA electron temperature measurement relies on fitting a Maxwellian, payload charging, if severe enough, can cause measurement error by cutting off too large a portion of the spectrum to obtain an accurate fit.

6.5 Screening process

To achieve the desired result of an ultem frame with a smooth layer of screen flat across it, a process of tensioning the screen and gluing it in place was developpped. While the screens have almost no structural integrity to resist punctures or tears, they are able to hold a small amount of tension along their plane. Since the frames are cylindrical sections, it is possible to drape a screen across a frame and have it hang such that there are no sharp corners or edges applying pressure to the screen. A jig was constructed which consists of a stand with two interchangeable cylinders. Each cylinder has a radius such that an inner or outer frame will sit smoothly on its surface. Grooves are machined into the cylinder such that the "windows" in the screen frame have a rectangular section which rises to the top surface of the frame and creates one, smooth surface across the entirety of the frame.

A section of screen is then cut to the desired width of the frame. For outer screens, this is the entire width (past the thru-holes which are used to secure the frames to the body of the CERPA) and for the inner frames this width is just inside the thru-holes. By not covering the thru-holes on the innner frame, this ensures that passing a metal screw through the concentric layers will not make electrical contact between the inner screen and the outer screen or body and cause a short.

The section of screen is carefully fixed to a piece of metal bar stock using kapton tape two opposing ends. Care must be taken to avoid static build-up on the kapton tape which will attract the screen towards the tape and can lead to wrinkling. Good practice is to use a conductor to remove static charge on the kapton tape. Once the bar stock is in place, the screen is draped over the ultem frame placed on a jig such that the screen side is pointing towards the jig and the bar stock side is facing away. The bar stock should be dangling from the edges of the jig and supported only by the screen.

Small covers with weights are placed over top of the screen on the windows of the frame. These covers match the curvature of the frame and jig and serve two purposes: 1) that they cover the windows in the frames from accidental application of adhesive while allowing maximum access to the ultem frame itself and 2) they further ensure a flat screen surface across the windowed area.

The adhesive to secure the screen to he frame had to work well enough to keep the screen flat during vibrational testing while being both electrically conducting and low outgassing. Two materials were tested for this purpose; Aerodag and Aquadag. Aerodag provides an even coating (which is desirable) but it was found that the spray would be transported via capillary action into the windowed portion of the screen (non-desirable as it decreases the effective transmittance of the screen) even underneath the small weighted covers. Aquadag has the benefit of controlling the viscosity of the solution as it is manually mixed with water to form a sort of paste. As it is applied with a brush, it can also be controlled where it is applied to more easily, though care must be taken to spread the mixture evenly across the surface of the frame.

The electrical contact for the inner frames is made through a small brass button with a wire which drops down to the circuitry below the aperture. A small recession is milled into the frame of the inner screen such that the surface of the button is marginally above the ultem frame. Aquadag is applied to this recession, the button with wire soldered to it is pressed into it, and the screen is applied over the top. Care must be taken to avoid moving the wire too much and causing the button to break through the screen. Single stranded wire is used in place of braided as it is more malleable and does not transfer as much force to the button, thus decreasing the chance of breaking the screen. This is a calculated trade-off however as single stranded wire is more vulnerable to breaking during vibration than braided.

6.6 First flight

The first two CERPA instruments (CERPA-A and CERPA-B) flew on the SUBTEC-8 payload launched from Wallops Island, VA in October 2019. This was a technology development mission aimed at developping new protocols for communicating with ejectable payloads and as such had no science goals. CERPA-A also had a small ion RPA facing ram and CERPA-B was configured to have a miniature fluxgate magnetometer.

6.6.1 Data

Despite demonstrating survivability during payload integration and vibrational testing, both CERPA instruments exhibited a fatal shorting of the sweep and ground screens immediately upon ejection. Data are presented where available and will be used to motivate a failure mode analysis and design review.

Figure 14 shows the anode current (top) and sweep voltage (bottom) for CERPA-A. The short in the sweep screen occurs at the ejection time, just before T+31.2 seconds post launch. The small variations on the anode current present at the very start of the plot are likely signal noise caused by vibrations associated with the payload doors opening in preparation for ejection.

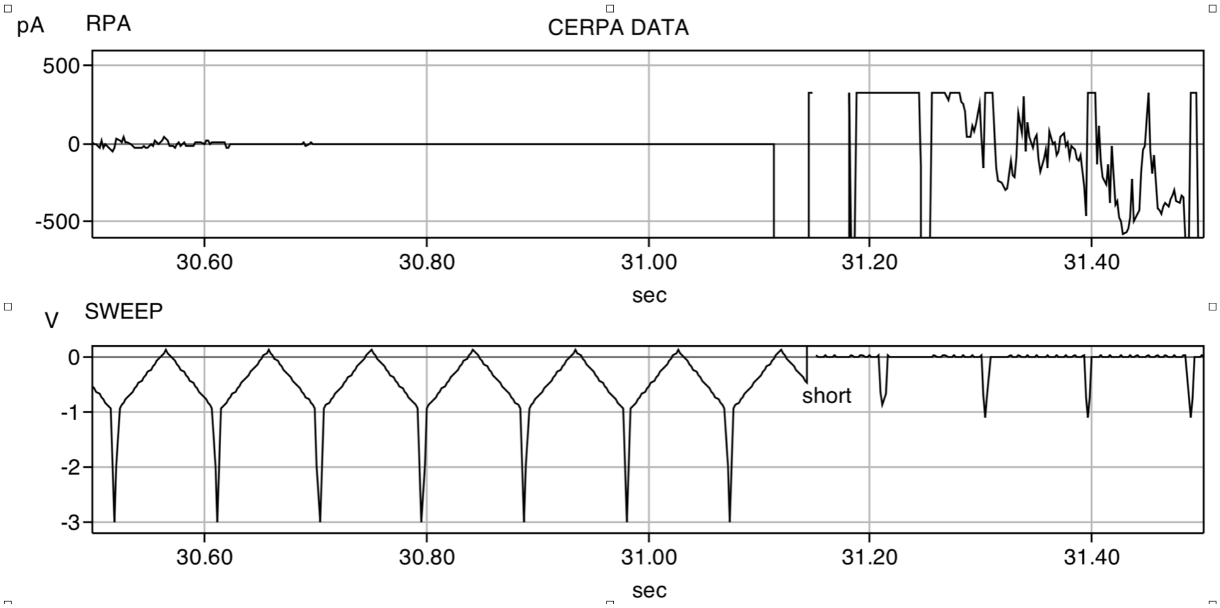

Figure 14: Two plots from one of the CERPA instruments on SUBTEC-8. The period of time is seconds after launch and shows just before to just after the instruments are ejected. The top plot shows the current incident on the anode. The bottom plot shows the voltage on the sweep screen. The short occurs at ejection time and is labeled on the plot. Plot courtesy of Mark Widholm.

The ion RPA on CERPA-A known as FIRPA (Forward Ion RPA) remained functioning throughout the flight with the exception of telemetry dropouts.

Ion data are shown in Figure 15 which depict the differential spectrum recorded from T+100 to loss of signal shortly after T+350. White indicates areas with telemetry dropouts. The FIRPA instrument was oriented such that it was facing ram, the diagonal structuring in the differential spectrum would suggest that there was some amount of coning of the payload. The peak flux is around 1 eV. The minimum of the two horizontal stripes through the data give the payload potential. Since the payload will charge to a negative potential, ambient ions will be accelerated towards the payload and the minimum of their energy is a close approximation of the payload potential. In this case, the payload potential stays in the range of .5-.8 V.

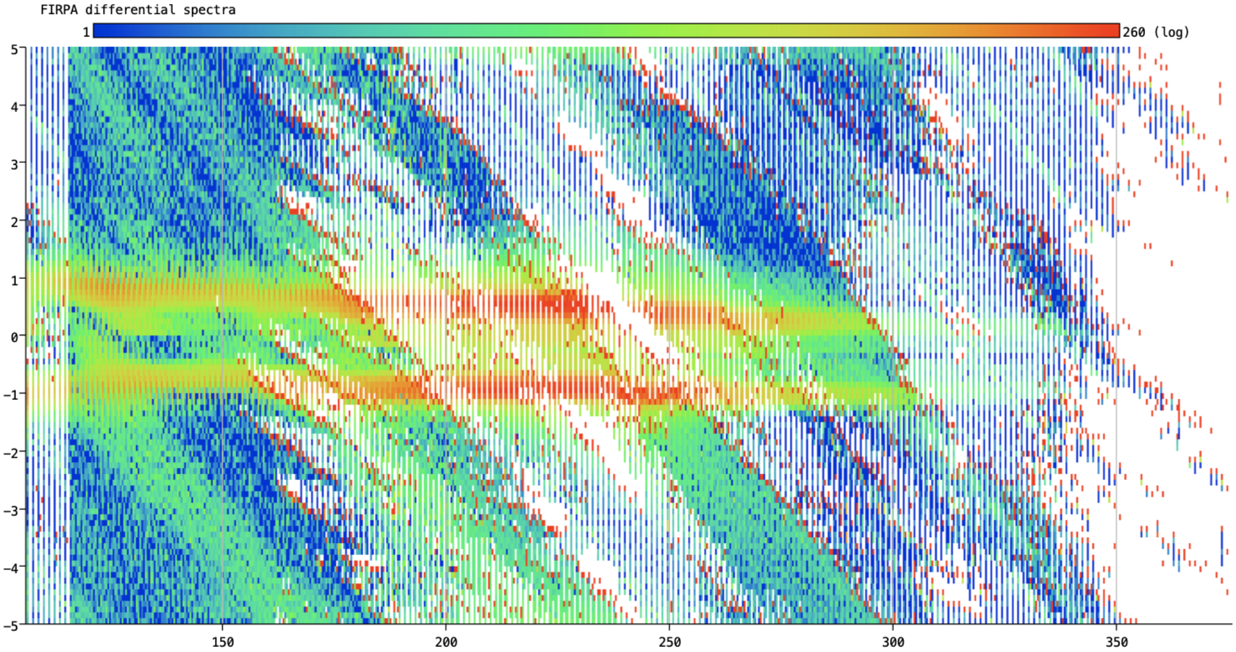

Figure 15: Differential ion spectrum recorded by FIRPA. White indicates telemetry drop out. The vertical axis is in units of electron volts, the negative sign indicates the sweep down in voltage, positive up in voltage. Plot courtesy of Marc Widholm. Peaks from both sweep directions were recorded around 1 eV

It is unclear what caused the short of both CERPA screens at ejection. The CERPA was shown to be able to withstand greater than the maximum torque experienced during launch, as well demonstrating survivability during vibrational testing.

There are currently two possible causes identified. The first is that the combination of vibration and then the torque from ejection caused the screens to short. In laboratory testing, the engineering model underwent torque testing, but flight hardware did not. It is possible that the adhesion of the screens became marginal during vibrational testing, then the shock of ejection caused them to short.

The second cause is that it is possible that the doors which open to expose the ejectables on the main payload somehow got stuck or otherwise did not fully clear the ejection tube and the instruments were obstructed during launch (based on communications with NASA Wallops after launch). This scenario is also possible, though if it were the case,

Figure 16: The original design (left) and the modified design (right). This comparison of frame designs shows the changes to the frames in order to reduce the maximum amount of stress at any point on the frame. The changes are calculated to reduce the maximum stress by greater than 50%. Figure courtesy of Dominic Puoppulo.

both instruments must have undergone the same type of glancing blow from the doors in such a way that the screens were damanged but the payload did not tumble.

6.7 Design modifications

Modifications to the CERPA design are operating under the assumption that the first outlined scenario was the cause of the failure, as the issue with the doors cannot be controlled from the experimenter's side and at this time, it cannot be determined if the doors were an issue or not.

Two modifications to the CERPA insturment design have been identified to produce a more robust and reliable instrument. The first is to alter the cross supports in the screen frames to be diagonal rather than horizontal and vertical. This can be seen in Figure 16.

The change in cross bracing of the screen frames results in a reduction in the maximum stress experienced by any point on the frame by greater than greater than 50% as determined by simulations using SolidWorks. The exact dimensions are not yet finalized, as this type of bracing results in a reduction of the aperture. In the design pictured in Figure 16, the original frame is 2.2 inches tall with an outer arc length of 3.04 inches while the modified frame is 3.1 inches tall with the same outer arc length. For the original frame, this yields an active area of 74% of the outer surface, but only 64% for the modified frame. This change would reduce the signal received on the anode and make it more challenging to make an accurate measurement of electron temperature. This consideration is especially important for the CERPA, which lacks a positively biased outer screen such as the one on the ERPA instrument (Cohen et al., 2016) which accelerates electrons into the detector to overcome spacecraft charging issues.

In addition to the modification to the frame cross bracing, the method for adhering the screens to the frames is also being revised. For the original design, the inner and outer frames were separate pieces held in place by machine screws which secured both concentric layers into the top and base of the instrument. The inner frame had a thin relief milled such that the inner screens would not be in direct contact with the outer frame. This design was to allow for the separate frames to vibrate without friction being applied to the inner screen by the outer frame. Instead, a new process is to be utilized in which the screens and frames are treated with a conductive silver epoxy and pressed together to form one cohesive unit. The outer screen will also be epoxied in place with a thin metal shield forming the outermost layer. This method should minimize issues with vibration, as the frames will move together as one rather than independently. This should also allow for better adhesion of the screens and more tension to be applied across the screen which smooths wrinkles and helps insure maximum throughput of electrons to the anode. Maximizing the signal on the anode is especially important in light of a reduction in the overall aperture.

CHAPTER 7

Introduction to Research Topics

Here I will briefly provide some introduction to the research topics which follow. The purpose is to provide some context between the more basic introductory material which precedes this and the (by nature) more technical work which follows.

Overview

The research topics presented next involve very different auroral events. In Chapter 7, pulsating aurora is the focus. In Chapter 8, Poleward Moving Auroral Forms (PMAFs) in the cusp are the focus. At a surface level, this topics could not be more different. Pulsating aurora is nightside event – most commonly post-midnight (Jones et al., 2011). It is associated with the recovery phase of a substorm, may occur over long time scales and over a very large geographic scales Jones et al. (2013), though pulsating patches themselves are small scale structures.

As discussed in section 5.2.3, pulsating aurora is comprised of high energy electron precipitation. Since these electrons are higher in energy scales than discrete or diffuse aurora, the pulsating patches we see are lower in the ionosphere than other types of aurora; often occuring in the lower E- and D-regions of the ionosphere (60-100 km is a good, general idea of the range). Pulsating aurora has the propensity to create low-altitude secondary (often called backscatter) electrons. This represents a further source of ionization in the ionosphere. The secondary electrons produced are lower in energy than the primary high energy precipitation, but may be in the range of 100 eV (Evans et al., 1987) up to perhaps keV scales (Samara et al., 2017).

In contrast, the cusp region is much more constrained geographically. Rather than being sourced as a by-product of high energy precipitation, the cusp precipitation is sourced from the solar wind and by definition, soft precipitation (again around 100 eV scales). In the cusp, the soft precipitation deposits energy into the ionosphere largely in the range of 200-400 km altitude.

The idea which links these two different types of auroral events and regions in the following research is this: large fluxes of soft electrons are distributed into the ambient ionosphere through fine-scale features. These structures, though much smaller than the overall regions they occur in – have ramifications for the dynamics of the region as a whole. Particularly, in both cases we are interested in upwelling processes that may be tied to those soft electrons. Generally, soft electrons are associated with the establishment of an ambipolar field (see, Figure 8) by heating the ambient ionospheric electrons and causing them to expand upwards along the local magnetic field line. That expansion of a large body of electrons upwards out of a quasi-neutral plasma creates a separation of charge, which establishes an electric field. The positive ions are not efficiently heated by soft electron precipitation, but they are dragged upwards by the negative space charge (i.e., by the upward expanding, large "cloud" of electrons). This is type II upwelling; for type II upwelling to drive neutral upflow, we require that the ions (which are many times heavier than electrons) drag the neutrals upwards with them).

Another way in which the soft electrons may be a factor in upwelling is by altering the conductivity of the region. In this mechanism, consider that soft electrons are primarily going land (i.e., deposit energy) in the F-region of the ionosphere. More electrons here means a higher conductivity. In turn, higher conductivity may open the region to closing FACs which otherwise close at lower altitudes and thus, higher altitude joule dissipation may play a role. This is a mechanism which is only more recently being considered by work such as Varney and Zhang (2017), but may well be an important factor in the upwelling picture. This mechanism is not considered in either of the studies presented. For the pulsating aurora study in Chapter 8, we simply lack the requisite in-situ measurements with which to investigate the local joule heating term, $j \cdot E$. For the case of the cusp study presented in Chapter 9, the radar data suggests that joule dissipation is not the dominant heating mechanism. This could however be a topic for future studies.

CHAPTER 8

Observations of Ion Upwelling during Pulsating Aurora Event

The following chapter is adapted from:

Kenward, D. R., M. R. Lessard, B. A. Fritz, R. H. Varney, R. G. Michell and D. Hampton (2020), Observations of ion upflow and red surge during pulsating aurora, J. Geophys Res. Space Physics, Submitted.

This work was a collaborative effort. Bruce Fritz designed the original Incoherent Scatter Radar (ISR) experiment as part of the ISR summer school. Roger Varney ran the experiment mode at Poker Flat while I operated an white light intensified field camera. In the end, the camera data which I collected did not make it into the study, instead replaced by filtered camera data provided by Robert Michell and Don Hampton. I performed analysis using the radar data processed by Roger Varney and the camera data under the guidance of Don and Robert.

8.1 Abstract

Data from filtered All Sky Imagers (557.7, 630.0 nm) located at Poker Flat are presented alongside four hours of Poker Flat Incoherent Scatter Radar (PFISR) data which shows ion upflow signatures in the vicinity of pulsating aurora. Pulsating aurora observations are more often reported in 557.7 nm and 427.8 nm, as these emissions are more sensitive to high energy (10s of keV) electron precipitation. However, data are presented here which show a strong non-pulsating 630.0 nm emission. This emission is generated preferentially by soft (100s of eV scale) precipitation. We present all sky camera observations which

suggest regions of enhanced soft electron precipitation in conjunction with enhanced ambipolar fields, a known factor contributing to ion upflow.

8.2 Introduction

Ion upflow is a part of the outflow process. During the upflow process, ionospheric plasma increases in scale height where ions may then undergo a second energization process and outflow. This causes mass loading of flux tubes and affects the way in which the magnetosphere responds to external drivers. One process which contributes to ion upflow is the heating of the the ambient electron population of the ionosphere, which causes an upward adiabatic expansion and therefore a separation of charge that leads to a parallel electric field. This field couples the heated electrons to the ion population and is known as Type II upflow (Strangeway et al., 2005).

Pulsating aurora is a common phenomenon which often occurs shortly after magnetic midnight (Lessard, 2013). Jones et al. (2013) reported 74 pulsating aurora events out of 119 days of optical data; Partamies et al. (2017) using a database of 400 event reported agreement to such an occurrence rate. These events are visible as patches which vary in brightness periodically in comparison to the more steady, diffuse background in which they are embedded. Typical pulsation periods range between 2-20 seconds (Royrvik and Davis, 1978), though the range of pulsation period may vary within the same event, or even within the same structure (Humberset et al., 2016). An entire event lasts typically on the order of 1.5 hrs (Jones et al., 2011; Partamies et al., 2017), although much longer events are also reported; up to 7 hours (Partamies et al., 2017) or in a more extreme case, more than 15 hours as reported by Jones et al. (2013).

The pulsating patches themselves are the ionospheric signature of high energy (on the order of 10s - 100s of keV and opposed to the "few" keV of the diffuse aurora) electron precipitation (Brown et al., 1976; Miyoshi et al., 2015; Partamies et al., 2017) although pulsating aurora energies as low as 1 keV have also been reported (McEwan et al., 1981). These high energy electrons are sourced from the interaction of chorus waves near the magnetic equator, which scatter the electrons into the loss cone (Kasahara et al., 2018). The visible signature of these electrons are the pulsating patches most easily observed in 557.7 nm and 427.8 nm observations (due to the shorter lifetime of the emission than the red line, and the greater densities at lower altitudes where the high energy precipitation deposits its energy) rather than the 630.0 nm emission line. However, observations of pulsating aurora at 630.0 nm have been reported (Eather, 1969; Liang et al., 2016).

Conversely, black aurora is the distinct lack of auroral emission in a well defined region (Davis, 1978). Black aurora may appear embedded within pulsating aurora; appearing as narrow regions within or around pulsating patches (Royrvik and Davis, 1978). The cause of black aurora is yet unknown; though several theories have been put forth such as a region of downward current associated with a divergent electric field structure (Marklund et al., 1997), localized suppression of pitch angle scattering (Peticolas et al., 2002), or the relaxation of enhanced plasma pressure near the inner plasma sheet boundary (Sakaguchi et al., 2011). The structuring of black aurora and how it may relate to pulsating aurora is also unknown.

Evans et al. (1987) presented data from the NOAA 6 satellite and subsequent analysis which demonstrated a consistent, low energy tail in electron spectra in the region of pulsating aurora that they attributed to backscatter (or secondary) electrons caused by the primary, high energy electrons in the opposite hemisphere. Recently, Samara et al. (2017) demonstrated through use of optical data such a population of secondary electrons may undergo bounce motion, "subsequently contributing to the total precipitating electron flux in any given hemisphere." They confirm these results with predictions of the SuperThermal Electron Transport (STET) model, which predicts for such a scenario that 15 - 40% of the energy flux gets reflected back up for the primary precipitating electrons with energies of 5 keV (Khazanov et al., 2014).

Pulsating aurora is a commonly occuring phenomenon embedded within diffuse aurora which can operate for hours at a time Nishimura et al. (2020), and represents a significant flux of energy into the ionosphere (Newell et al., 2009). Despite this, relatively few studies have investigated the ability of pulsating aurora to drive density scale height increases in the ionosphere - thermosphere system. In this study, All Sky Imager (ASI) data, and data from the Poker Flat Incoherent Scatter Radar (PFISR) are used to demonstrate that pulsating aurora can drive ionospheric pressure gradients which can lead to ion upflow.

8.3 Instrumentation

Observations are presented from Poker Flat, AK, on February 5th, 2017. The All Sky Imagers were run throughout the night, while the Poker Flat Incoherrent Scatter Radar (PFISR) experiment "TopsideUpflow2" ran from 12:00 - 16:00 UT. This consists of seven beam positions which are shown in Figure 17 and was constructed to give very good statistics in the F-region and topside ionosphere. Beams 3 through 7 form a fan in a plane of constant magnetic longitude that includes the local magnetic zenith beam direction (beam 7) and the vertical direction (beam 3). Beams 1 and 2 are pointed northwest and northeast to allow for estimation of vector velocities. The arrangement of the PFISR beam directions are shown in Figure 17. Pulses are sent out along five beams in the fan three times as often as pulses in the other two beams to give those beams better statistics. The mode uses three frequency channels, and data from all three channels are averaged together to give better statistics. Every pulse transmits a pair of 330 μs (49.5 km) pulses on two of the three channels while the third channel collects noise samples. The pulses are 7 ms apart, yielding an effective duty cycle of 9.4%. This mode gives 50.42 independent estimates of the autocorrelation function (ACF) per second for the beams in the fan. The lag profile arrays are gated into ACFs at 24.75 km range gates, the ACFs are averaged over 5 minutes of data, and nonlinear least-squares fitting is used to fit the ACFs for electron density, electron temperature, ion temperature, and line-of-sight velocity.

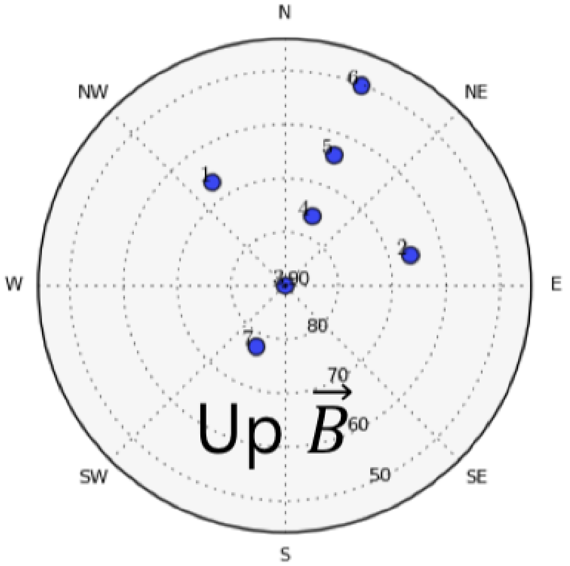

Figure 17: The orientation of the 7-beam mode operated by PFISR. Beam 7 is along the local magnetic field line.

The 557.7 nm (green line) ASI data was provided by NASA GSFC. The imager used was part of the Multi-spectral Observatory Of Sensitive EMCCD (MOOSE) observatory, installed at Poker Flat. These are Andor Ixon DU-888 EMCCD (Electron Multiplying Charge Coupled Device) imagers that use a 1024 x 1024 pixel chip, with internal binning capabilities that allow tradeoffs between temporal and spatial resolution. For the observations presented, the MOOSE imager was operating with an all sky (180 deg. FOV) lens and a 557.7 nm narrowband filter (2 nm FWHM bandpass). The CCD was cooled to -70 C to reduce thermal noise and was set to 2 x 2 binning, resulting in a 512 x 512 image at 3.3 frames per second (300 ms exposure time).

The 630 nm (red line) data comes from a digital, EMCCD-based, ASI at Poker Flat, filtered for the oxygen red, green, and blue line emissions (630.0, 557.7 and 427.8 nm). A composite image from this system is used in figure 20 The three filters are cycled on a 12.5 s cadence. Filter bandpasses are approximately 2 nm (Lynch et al., 2015).

8.4 Observations

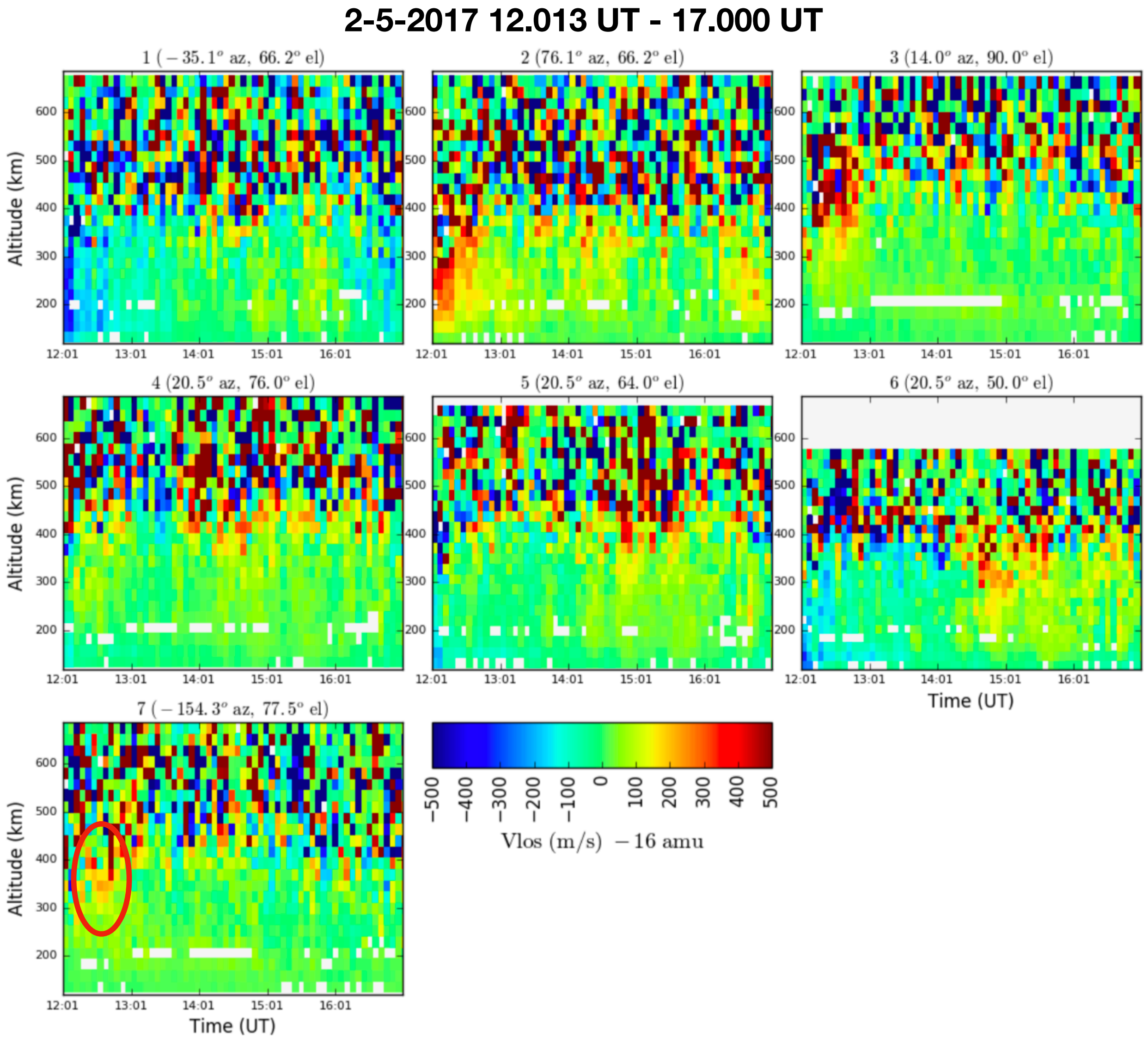

Figure 18: Line-of-sight ion velocity data are shown for each PFISR beam. Here, positive values indicate ions moving away from the beam, negative values towards the beam. A single column in a plot represents a 5 minute integration time. The vertical axis is the height resolution of the radar pulse.

Early in the evening from UT 1200 to UT 1230, beams 1 and 2 (see Figure 18 record ion velocities which indicate an eastward flow in the region of approximately 100-300 km altitude. Such flows are expected post-midnight after PFISR rotates past the Harang discontinuity. This flow is apparent in the first two panels of Figure 18 which show

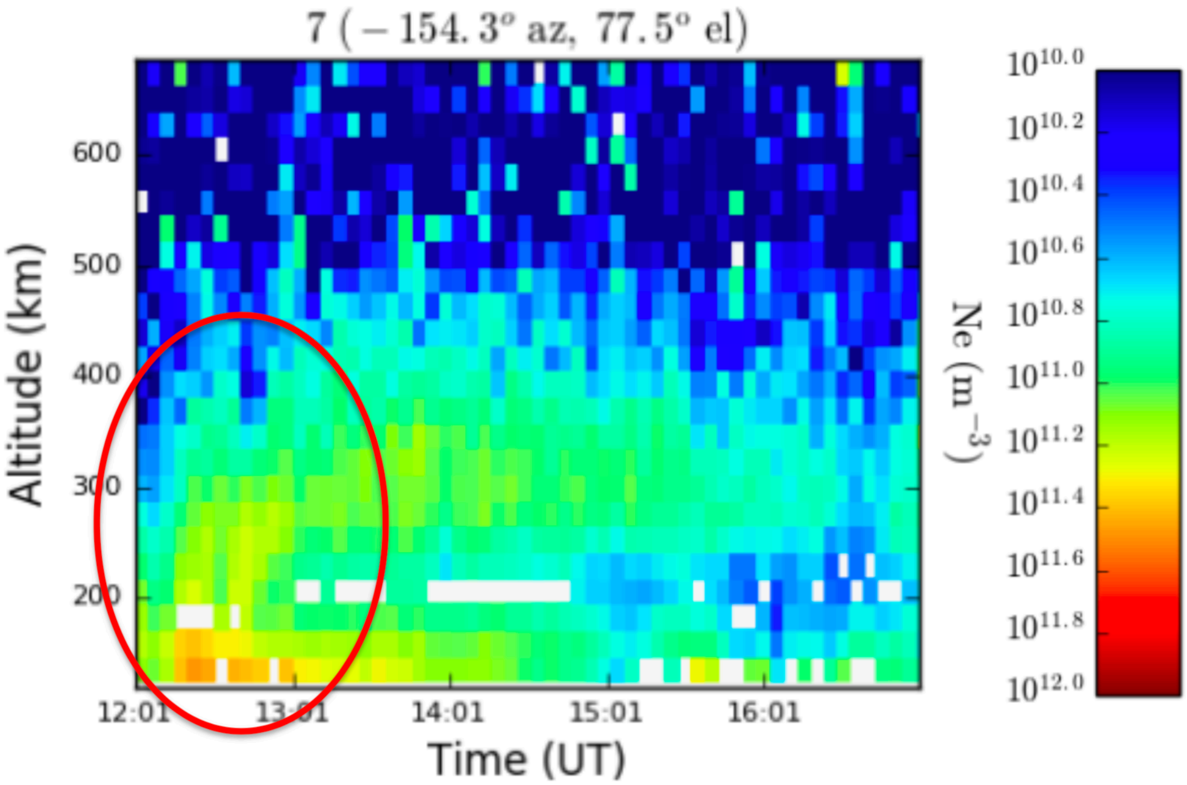

Figure 19: Electron number density recorded by PFISR. A “plume” of ionization is seen rising from lower altitudes close to the start of the pulsating aurora.

a negative velocity (towards the radar) in beam 1 and a positive velocity in beam 2 (away from the radar) until about UT 12:30. Near the time that the pulsating aurora starts (around UT 12:20), PFISR begins to detect enhanced electron number densities and temperatures as shown in Figure 19. This appears as a “plume” of ionization which rises out of the E-region of the ionosphere. This is likely caused by the high energy electrons in the pulsating aurora causing secondary ionization. Interestingly, the eastward convection visible in Figure 18 beams 1 and 2 diminishes around the time of this increase in the number density.

Figure 18 also shows the ion upflow signature from beam 7 (up-B direction) present between UT 12:00 - 13:00 from 300 km at the start and becoming stronger and increasing in altitude (towards 400 km) towards the end of that time period. While a few temporally and spatially constrained bins show velocity enhancements in the ion data from UT 12:00 - 12:30, the upflow signature becomes more apparent from UT 12:30 onwards (see red

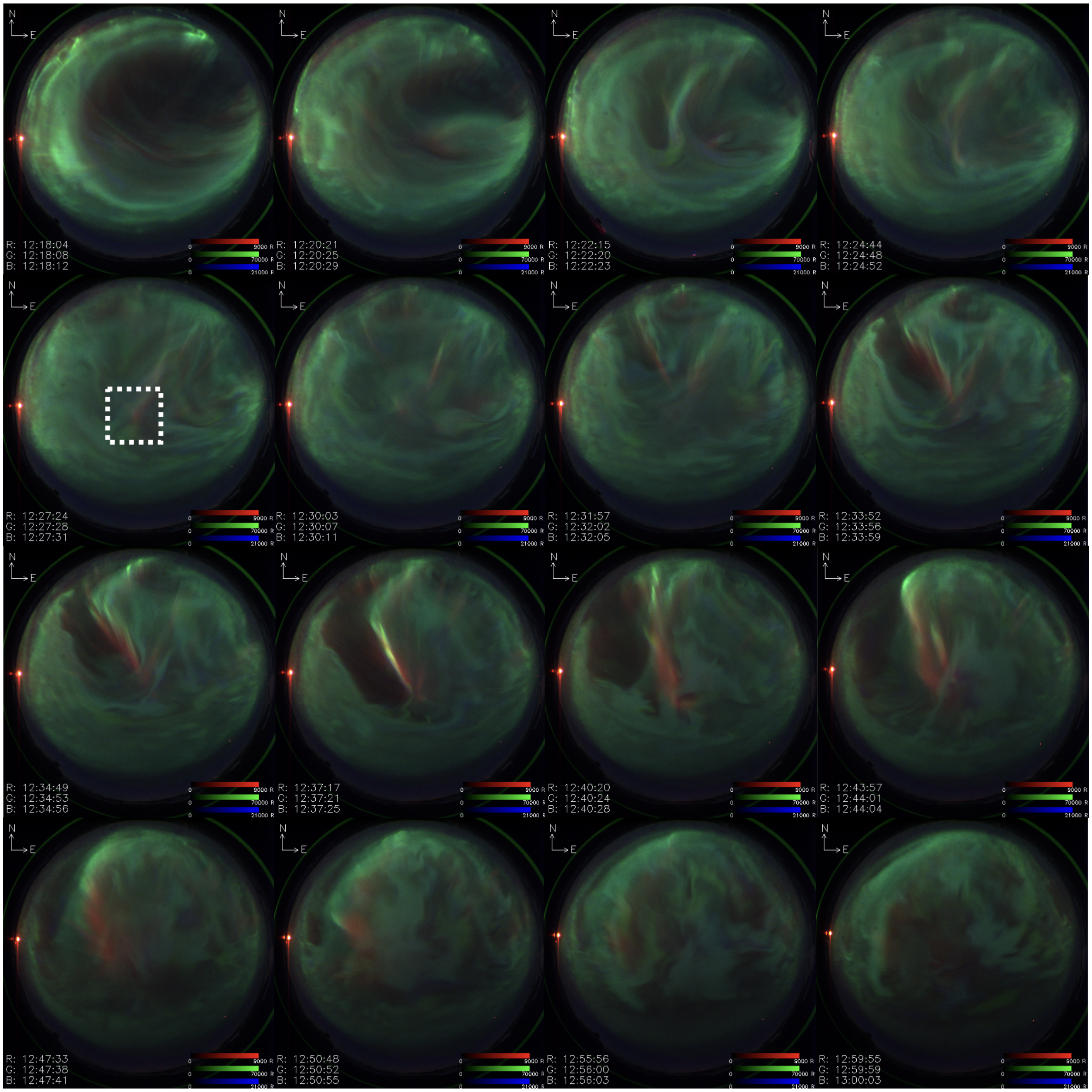

Figure 20: Composite All Sky Imager frames from the Poker Flat EMCCD. Selected images are not regularly sampled from available data but are meant to depict the evolution of the aurora during the event. The white dotted box indicates the location of magnetic zenith (center of the box) which is the same for all frames.

circle on bottom plot in Figure 18). Ion velocity enhancements are also present in beams 3 (near the same UT) and later in the evening in beams 4, 5 and 6. However, beams 4, 5 and 6 are not oriented along the field line and so it is difficult to determine whether these are also signatures of upflow.

Diffuse aurora was visible earlier in the evening, with pulsating aurora starting around UT 1220. Examples of the 630.0 and 557.7 nm auroral emissions are given in Figure 20. In each frame, north is up, east right and magnetic zenith is in the region highlighted by the white box (see the first frame of the second row for reference).

Pulsating aurora becomes visible predominantly in the green (557.7 nm) line at approximately UT 12:20. Figure 20 shows the progression of the aurora beginning with the earliest onset of pulsating aurora through the break up and disappearance of the red line structure which will be discussed later. Figure 21 shows the pulsating aurora as a time series of the emission brightness. To create this plot, the 50x50 pixel square indicated by the white dotted box in Figure 20 (see left-most image in row 2) are averaged over to give the average brightness of the pulsating aurora at magnetic zenith. Pulsations are seen as periodic enhancements in the brightness in the 557.7 nm emission line. Also included as separate panels in Figure 21 are electron temperature, electron number density and ion velocity all from beam 7 (magnetic zenith). These panels will be discussed later.

Small, dim red line features can be seen in the composite images in Figure 20 from UT 12:20 onwards. The most notable feature is the sudden appearance of a red line arc which forms on the boundary of a large region of black aurora. This feature is first apparent in the UT 12:33 frame in Figure 20; though comparing to the previous example frame, a weak red line structure is visible in approximately the same location. Over the course of the next ∼3 minutes the black aurora region expands to the south-west (towards magnetic zenith). During this, the red line emission increases in intensity and moves with the black aurora, extending outward from roughly magnetic zenith and stretching northward. After several minutes (again, about 3 minutes) the red line arc begins to "break up" and pulsating patch structures move into the black aurora region from the south. Bright, green line features appear to be co-located with structure in the red line. As the black aurora "retreats" westward and eventually disappears or becomes non-distinct, the intensity of

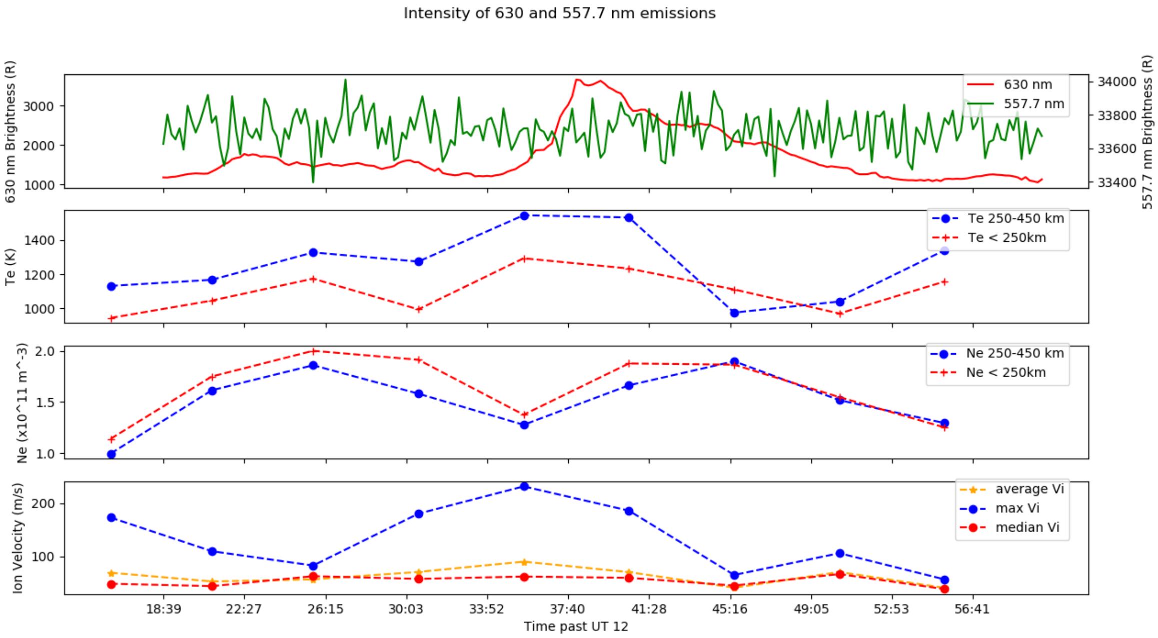

Figure 21: This figure shows the intensity of the 630.0 (red line) and 557.7 nm (green line) emission together with their respective scales (top panel). The camera pixels used for this time series are an average of the 50x50 pixel square indicated in Figure 20. Below, parameters from PFISR beam 7 are displayed for comparison. Electron temperature is portrayed in the second panel, with the blue line displaying the average between 250-450 km and the red line the average below 250 km. The third panel shows the same averages for the electron density. The bottom panel shows the ion velocity represented three ways: the maximum value (blue line) the average value (yellow line) and the median value (red line) all within the region between 250 and 450 km.

the red line emission diminishes, the arc becomes diffuse, and by the last frame in Figure 20 it is gone.

8.5 Analysis

The onset of the red line enhancement coincides with the highest magnitude electron temperature recorded by PFISR in the magnetic zenith look direction during the hour of UT 12. This also coincides with the largest ion velocity enhancement and a local minimum in the electron number density. As the electron temperature decays, so does the ion velocity enhancement; while at the same time the electron number density recovers from the local minimum. These behaviors occur simultaneously with the movement of the red line enhancement westward, away from the magnetic zenith direction.

The sudden (∼5 minute), localized increase in the red line emission suggests that there is a localized, lower energy and more broadband portion of the precipitating electron spectra on the boundary between the black and diffuse/pulsating regions. Pulsating aurora is typically associated with high energy (10s of keV) precipitation which deposits the bulk of its energy at much lower altitudes – below even 100 km (Brown et al., 1976). Secondary electrons caused by the high energy precipitation have been demonstrated to contribute to a low energy portion of the electron spectrum (Evans et al., 1987) and appear as periodic, small increases in brightness in camera data (Samara et al., 2017). The secondary electron explanation is however, not conducive to the sudden large scale increase as the pulsations are not the dominant feature.

Soft electron precipitation is considered a cause of ion upwelling by driving an ambipolar field which lifts ions (Strangeway et al., 2005). For the event presented here, there are two possible sources for soft electrons: secondary emission from pulsating aurora, and an unknown source which is evidenced by the strong, localized enhancement in the red line emission.

The altitude profile of the ambipolar field is calculated and shown in Figure 22. This field is calculated as the electron pressure gradient as shown in Equation 1, where N_e is the electron number density, T_e the electron temperature, e the elementary charge, and k_B is Boltzmann's constant.

$$E_{||} = \frac{-1}{eN_e}\nabla_{||}(N_e k_B T_e) = \frac{-k_B}{e}[\nabla T_e + T_e\frac{\nabla N_e}{N_e}] \tag{8.5.1}$$

The potential along the field line then can be calculated as the integral of this field. This has been performed for each 5 minute integration bin of the PFISR data. Figure

22 shows four selected times beginning at UT 12:36, 12:41, 12:51, and 13:01 respectively. The five panels in the figure show the evolution of the field, potential, and quantities used to derive these values as well as the line of sight ion velocity. The data presented are error filtered to remove points where the measurement error in T_e >1000 K or ion line-of-sight velocity >800 m/s. This eliminates points where statistics were too low to achieve acceptable fits to the parameters. The PFISR data beginning at UT 13:01 is displayed in preference to UT 12:56 because this error filtering removes most data above 350 km for the UT 12:56 time integration.

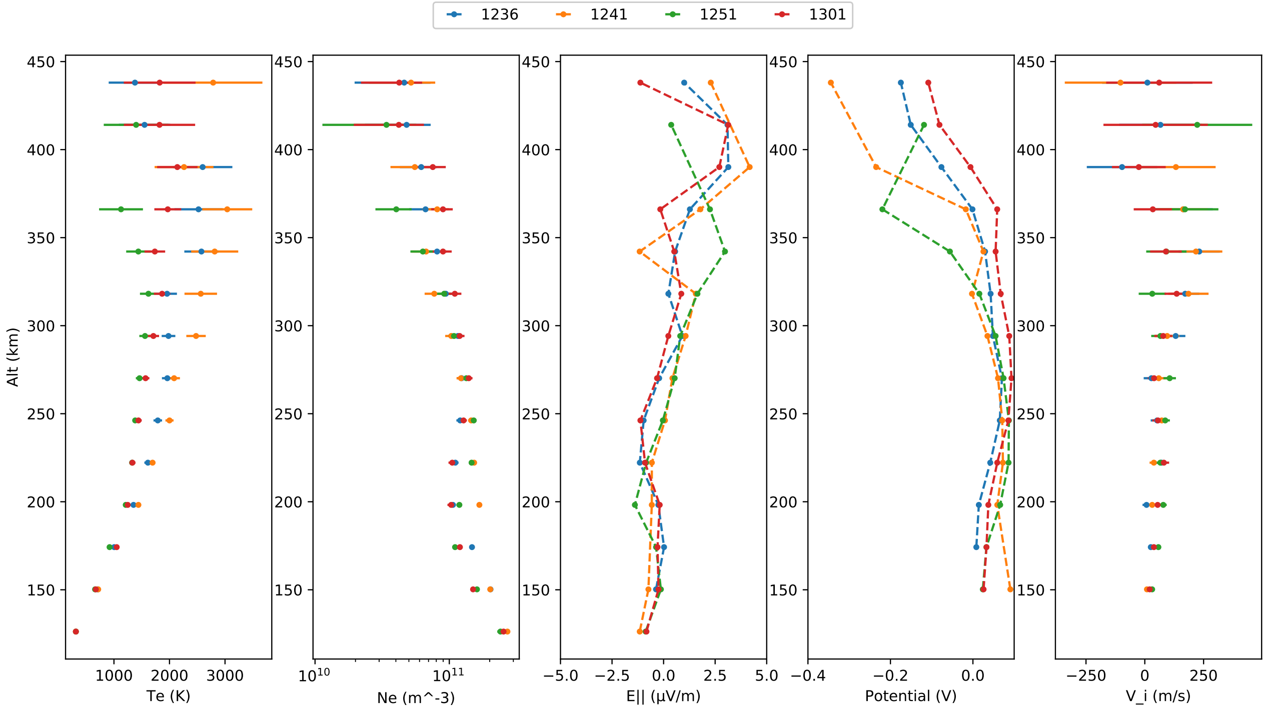

Figure 22: From left to right, electron temperature and density, ambipolar electric field, field aligned potential and line of sight ion velocity are shown for the times indicated (UT) with the height of the measurement on the y-axis. Data are from the PFISR beam oriented along the local field line.

The ambipolar field and potentials shown in Figure 22 have been selected to demonstrate the conditions at the start, in the middle, and at the end of this more strongly enhanced upflow event. The figures show a potential drop in the region of 300 km and upwards is present. The UT 12:41 line shows the highest magnitude of this potential, reaching a peak of near 0.4 V, roughly twice the potential from UT 12:36 and 13:01 plots and coincident with the bulk of the ion velocity enhancement below 400 km.

Interestingly, as is evident in comparing Figure 21 and Figure 22, the period of time with the highest ion velocity signature (i.e. upflow) is not coincident with the with strongest potential drop; though this could in part be an effect of the 5 minute time integration. To elaborate on Figure 21, the top plot shows the average intensity of the 630.0 nm and 557.7 nm emission line averaged in a 50 x 50 pixel grid centered on magnetic zenith. The second panel shows the electron temperature averaged in the two regions indicated (250-450 km and under 250 km), the third panel shows the electron number density averages for the same regions. The bottom panel shows three representations of the ion velocity in the 250-450 km region; as the maximum (blue line), average (yellow line) and median (red line). This is represented by three different methods in order to adequately characterize the velocity enhancement. The overall agreement in the shape of the lines demonstrates that the behavior seems to be a real effect and not an artifact of averaging, for example.

The cause of the red line increase and presumed increase in soft electron precipitation is unknown. Alfvén waves are often considered drivers of soft electron precipitation (see, e.g. (Chaston et al., 2001) and references therein). On the other hand, discrete arcs are typically associated with potential structures.

It has been suggested that pulsating aurora are driven by electrons which flow along field aligned currents in a pair of current sheets Fujii et al. (1985), resulting in an ionospheric return current. It has also been hypothesized that black aurora may be a signature of downward directed field aligned currents Marklund et al. (1997). If this were the case, the red line enhancement would appear on the boundary between oppositely directed current sheets. Fritz et al. (2015) presented observations of black aurora acting as a boundary between different pulsating structures, which could be a physically similar process.

Chaston and Seki (2010) show model results of Kelvin-Helmholtz and tearing instabilities in regions with transverse field aligned current gradients which would be consistent here with the interpretation of pulsating and black aurora representing oppositely directed current sheets. In these modeling work presented by Chaston and Seki (2010), a prominent feature in the scenarios examined is the generation of an inertial Alfvén wave. This wave feature could be driver for the presumed soft electron precipitation which manifests in the ASI data as the red line enhancement. On the other hand, the arc associated with the red line enhancement in question here exhibits a North-South orientation which is commonly associated with Rayleigh-Taylor type instabilities Fritz et al. (2015). Rayleigh-Taylor instabilities are also characterized by non-sheared edges, while Kelvin-Helmholtz and tearing instabilities are associated with sheared edges and/or vortical formations. From the camera data available, the arc in question shows little signs sheared edges (see frames time stamped from UT 12:33 to 12:43 in Figure 20) . There are a few localized bright spots which could be vortical structures, but the resolution makes it difficult to say definitively. As the arc evolves it breaks apart to finer scale features, which is consistent with the processes described by Chaston and Seki (2010).

8.6 Summary

Taken together, the timeline of events reported here demonstrating ion upflow during a pulsating aurora and in conjunction with a localized increase in red line emission are as follows:

- Aurora begins to pulsate. Electron density increase at low altitude and eastward convection diminishes.

- Electron temperature, number density and ion velocity all increase.
- Ambipolar field is generated through electron pressure gradients.
- Ion velocity and electron temperature reach their maxima while number density decreases to a local minimum.
- The red line intensity abruptly increases and follows the boundary of the black aurora region westward
- The discrete arc on the boundary begins to break up.
- The red line enhancement leaves the region of magnetic zenith. Electron temperature and ion velocity diminish and electron density recovers from local minimum.

We have presented a dataset which shows a small-scale, localized ion upflow event. This occurs after pulsating aurora has existed in the region for $\sim$ 20-25 minutes, during which time eastward convection has diminished. From the PFISR data, it is shown that during the period of pulsating aurora, the electron temperature and number density increases, and a weak ambipolar field sets up. However, the largest magnitude ion upflow signature coincides with a period in which the electron number density is diminished. This maximum in the ion upflow signature coincides with an abrupt increase in the 630 nm emission line. This red line emission appears as part of a discrete arc on the boundary of a large black aurora and pulsating regions. As the arc drifts westward, it appears to break up and pulsating aurora pushes into the region of black aurora.

The source of this increase in the red line emission is currently unknown, but the notion that it is driven by an instability seems plausible. While it is difficult to demonstrate that this is the case with only ground based camera and radar data, the sudden appearance of the structure, the subsequent movement of the arc with the boundary followed by ”breaking up” into more fine scale structures and the time scale in which it exists for are consistent with this being driven by, or a signature of an instability.

The ambipolar field and upflow signatures seen here are relatively weak and temporally isolated. However, the prevalence of pulsating aurora to occur and often linger for several hours motivates further study. In particular, conjunctions between ASI observations of pulsating aurora and satellite or rocket observations may be useful for determining the energy and pitch angle distributions of the low energy electrons which the 630.0 nm auroral emissison suggest are present. Additionally, the sudden appearance of the red line arc which follows boundary of the black aurora and pulsating regions is interesting and further statistical studies could be conducted which provide clues as to the generating mechanism; i.e. is the topology of the arc always N-S aligned? Does it always coincide with ion upflow? Does it happen when convection signatures are present in ISR data? Further studies are needed to understand events such as this one.

CHAPTER 9

Characterization of Soft Electron Precipitation in the Cusp Region during Poleward Moving Auroral Form Event

This chapter is adapted from:

Kenward, D. R., M. R. Lessard, B. A. Fritz, K. Oksavik, K. A. Lynch, T. M. Roberts, D. Hysell, I. J. Cohen, T. K. Yeoman, J. Moen, L. Clausen, F. Sigernes (2020), Characterization of Soft Electron Precipitation in the Cusp Region during Poleward Moving Auroral Form Event, Geophys. Res. Lett., Manuscript Submitted.

This was a collaborative effort. I began work related to RENU2 my first summer in graduate school. I performed the mechanical build for the ERPA and UVPMT instruments flown on RENU2 and completed construction of the EPLAS instrument which Ian Cohen had begun. Post-launch, I performed analysis of the EPLAS instrument data set (the majority of which makes up the following chapter) as well as electric and magnetic fields and electron temperature datasets. I present several datasets in the Flight and Event Overview section which represent analysis done by Jim Clemmons, Bruce Fritz and Kjellmar Oksavik. These datasets and the discussion of them are not included in the submitted Geophysical Research Letters manuscript, but they are crucial to the understanding of the RENU2 event.

9.1 Abstract

This letter presents the highest resolution data ever recorded from a sounding rocket inside a Cusp Region Poleward Moving Auroral Form (PMAF). The Rocket Experiment for Neutral Upwelling (RENU2) payload included an instrument called Electron Plasma

(EPLAS). It is a top-hat electrostatic analyzer that measures electron energies from 5 eV to 14.6 keV at 42 ms time resolution in a 360 degree field of view. EPLAS spent approximately 200 seconds inside a PMAF, where it recorded unprecedented structure in the electron precipitation. At the same time the Electron Retarding Potential Analyzer (ERPA) instrument onboard the payload recorded the ionospheric response as electron temperature enhancements. Coupling from 100 m spatial scales to km-scale heating were found, which is a result of the time integrated heating effect driven by the soft electron precipitation. We also report small scale electron velocity dispersions, which differ from those previously reported in the cusp.

9.2 Introduction

The cusp is a dynamic region of the magnetosphere which maps to open field lines at the magnetopause. The ionospheric footprint of the cusp is small; extending 1° - 2° in magnetic latitude and on average 2.5 hours in local time (Deng et al., 2015). The cusp is characterized and may be identified by the soft electron precipitation signature within its boundaries. Newell and Meng (1988) provide criteria for identifying between boundary layer and the cusp based on in-situ particle data from the DMSP satellites based on their analysis of 5609 individual passes through the dayside cusp. The criteria are that ion energy must be between .3-3 keV, electron energy under 200 eV, the ion energy flux less than 10^{10} eV/cm^2-s-sr, the electron energy flux less than 6x10^{10} eV/cm^2-s-sr, and that the energy flux in the 2- or 5- keV electron channel be less than 10^7 eV/cm^2-s-sr-eV.

Poleward Moving Auroral Forms (PMAFs) are transient ionospheric phenomena considered to be the ionospheric signature of Flux Transfer Events (FTEs) set off by pulsed reconnection at the magnetopause (Sandholt and Farrugia, 2007). PMAFs are periodic auroral brightenings which form at the equatorward boundary of the dayside auroral oval and then convect poleward. PMAFs are most commonly observed between 0900 and

1500 MLT (Lockwood et al., 1989). Sandholt et al. (1990) showed that the duration of one individual PMAF is between 2-10 minutes, with 3-15 minutes between successive events, in agreement with Lockwood et al. (1989) who found the mean period of events to be 8 minutes and Fasel (1995) who found the mean period to be 5 minutes.

Previous studies of the cusp such as Pfaff et al. (1998) have characterized cusp electron precipitation as being bursty, implying a temporal nature to the electron precipitation. Some studies have also reported cusp electrons with inverted-V precipitation signatures (Pfaff et al., 1998; Arnoldy et al., 1996). Such signatures constitute a relatively narrowband energy range, rising sharply to a constant energy with steep gradients at the boundaries of the implied accelerating potential (Newell, 2000). More typical cusp electron precipitation is broadband (Oksavik et al., 2004; Newell et al., 2009). Such electron spectra are believed to be caused by dispersive Alfvén waves (Newell et al., 2009). The 11,404 electron distributions recorded within the PMAF event recorded by RENU2 exhibit the latter characteristics; being soft (100s of eV and below) and broadband in their energies. This type of precipitation has been correlated experimentally to both ion and neutral upflow (Strangeway et al., 2005; Moen et al., 2004; Burchill et al., 2010).

The Rocket Experiment for Neutral Upwelling 2 (RENU2) rocket was launched on Dec 13, 2015 at 07:34 UT. The payload was launched from Andøya Space Center, Norway. At 407 s, the payload reached an apogee of 447 km. Approximately 45 seconds later the payload entered the PMAF as indicated by the electron spectra. See Lessard et al. (2019) which contains further background information regarding the conditions.

9.3 Instrumentation

The Electron Plasma (EPLAS) instrument is a tophat style electrostatic analyzer (Carlson et al., 1983). For the configuration of EPLAS flown on RENU2, the 30 anodes were arranged around 360°, each anode covering 10° in pitch angle resolution, with three 20 degree blindspots for the anode support structure. This 360 degree plane was oriented parallel to the rocket spin axis and background field. Additionally, electrons were accepted within a 4.5 degree angle either side of this plane for a 9 degree acceptance angle. The energy is stepped from 5 - 14,638 eV in 42 steps each with a 1 ms duration with an energy resolution of $\Delta E/E$ of 0.122 eV/eV. The geometric factor for a single anode pad is 1.12 x 10^{-4} sr-cm^2 eV/eV.

The Electron Retarding Potential Analyzer (ERPA) instrument provides the thermal electron temperature measurement with an energy range from 0.01-3 eV with 0.06 eV resolution. A detailed description may be found in Cohen et al. (2016) and Frederick-Frost et al. (2007).

9.4 Flight and Event Overview

Prior the the RENU2 launch at 07:34 UT, PMAFs were present in the region for approximately one hour, visible in Figures 23 and 24. These figures show north-south slices of the all sky imager 630.0 nm data which clearly show the PMAFs moving through the region. Figure 24 shows a close up of of the PMAF which RENU2 flew through with the trajectory indicated by the black line.

The EISCAT radar facility was operating in support of the mission and recorded the ionospheric response to the PMAFs throughout the night. The EISCAT survey data is shown in Figure 25. Strong electron temperature enhancements and weaker electron density enhancements are seen as the presumed signature of PMAFs moving through the region. Ion temperature enhancements are less pronounced, but stronger earlier in the evening, particularly near 06:10, 06:30 and 07:00 UT. Weaker ion temperature enhancements are visible around 07:40-07:45 UT. In the ion temperature enhancements prior to 07:10, the ion temperature often exceeds twice the background (1300 K). At the same time, the transient electron temperature enhancements often exceed twice the

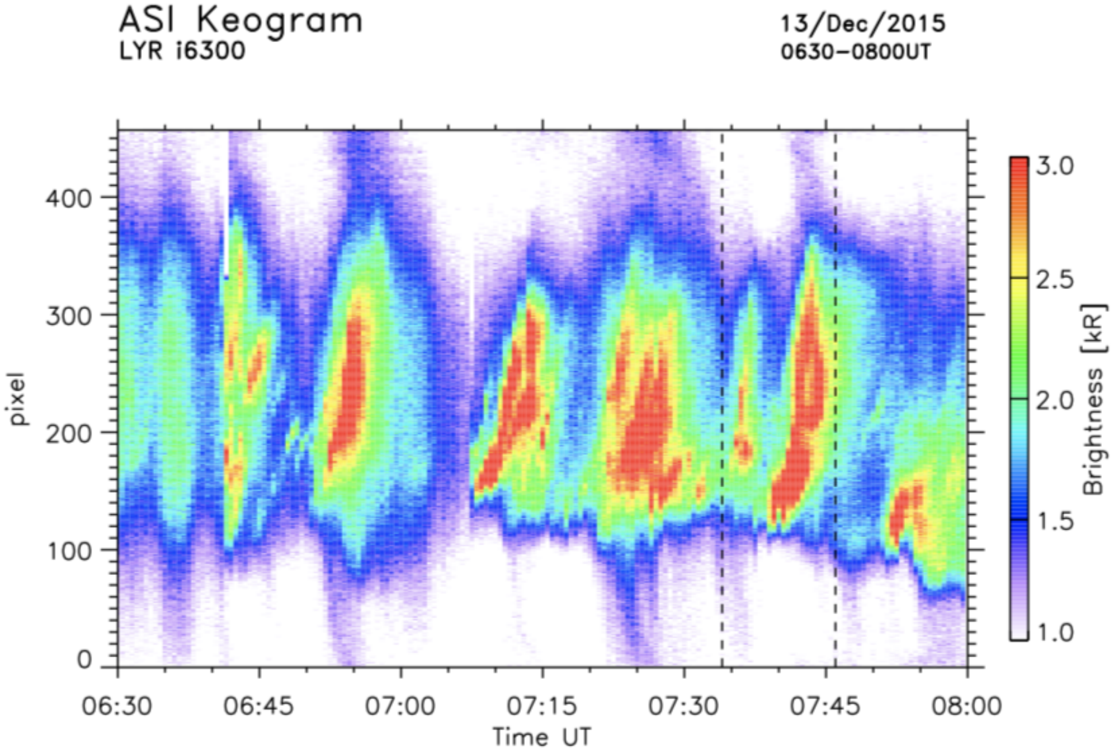

Figure 23: Keogram of 630.0 nm all-sky image data along the meridian demonstrating the large scale structure of a PMAF and showing the time history of the cusp. Vertical dashed lines indicate the time period of the RENU2 flight.

electron temperature background (1500 K), pointing to electron precipitation heating as the dominant process during the RENU2 flight (Oksavik, 2018).

RENU2 was also not the only spacecraft to make measurements in the cusp around the time of the event. The GRACE satellites happened to pass close to the RENU2 trajectory approximately 30 minutes prior to the launch of RENU2. Figure 26 shows the trajectories of GRACE and RENU2 overlaid onto a false color background. The false color image is the average 6300 nm emission intensity as recorded by the ASI in Longyerbyen, which is also used for Figures 23 and 24. The black line in the plot is the approximate orientation of the PMAFs as they swept through the region. It is obvious from inspection of the plot that the GRACE satellites did not cut through the most intense portion of the event.

Despite GRACE only passing through the edge of the PMAF activity where evidence of soft electron precipitation was weaker, GRACE did see a small neutral density enhancement in the region of the cusp. This is shown in Figure 27 as the small "bump" between

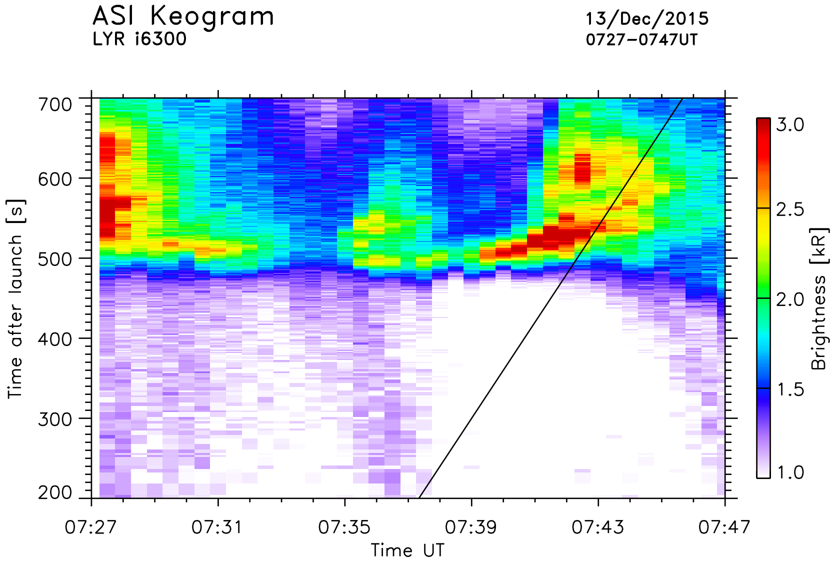

Figure 24: 630.0 nm keogram along the rocket trajectory and mapped to 250 km. The rocket trajectory is indicated by the black line.

the vertical red dashed lines in the bottom plot. This is corresponds to the location of PMAF activity as indicated by Figure 26 and is a small increase over the background density predicted by MSIS (dashed blue line). While this increase is not as large as those shown by Luhr et al. (2004) from CHAMP satellite data, it does demonstrate that there was a weak denisty enhancement in the cusp during the RENU2 event. Furthermore, because the GRACE measurement is roughly 30 minutes prior to RENU2 and only passed through the edge of the region, it is not unreasonable to think that this measurement is on the lower side for the event.

9.5 Data

EPLAS recorded data for 480 seconds from T+230 to T+710, corresponding to 7:37:50 to 7:45:50 UT. Of this time, RENU2 was within the PMAF boundary from just before 7:41:30 until 7:44:30. The boundary of the PMAF is visible in the spectra where the differential energy fluxes greatly increase, while the average energy of the incoming electrons decrease from KeV to $\sim$ 100 eV scales.

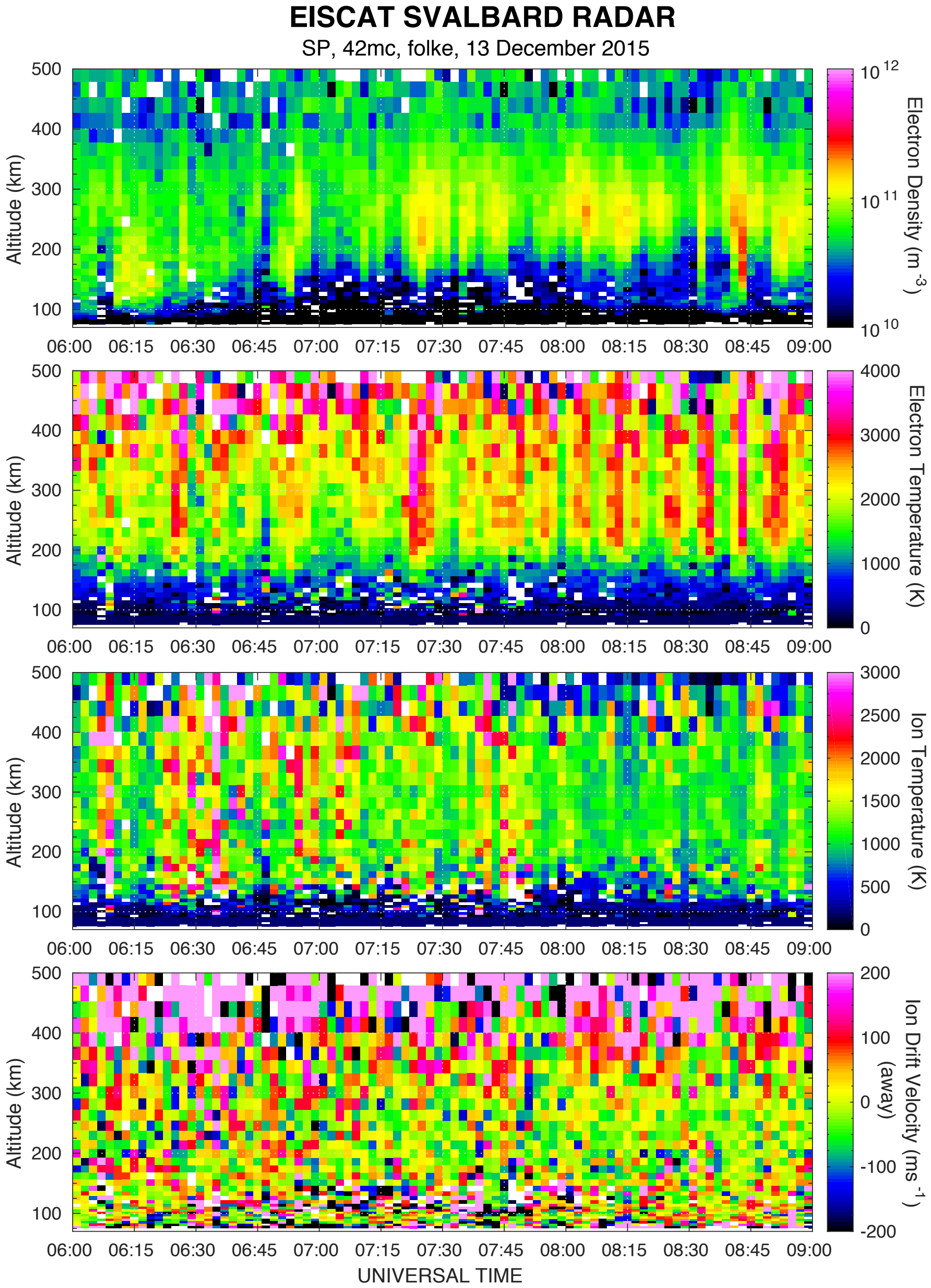

Figure 25: EISCAT observations spanning 1.5 hours pre and post RENU2 launch. From top to bottom EISCAT recorded electron density, electron temperature, ion temperature and ion drift velocity. For the drift velocity plot, positive indicates away from the radar.

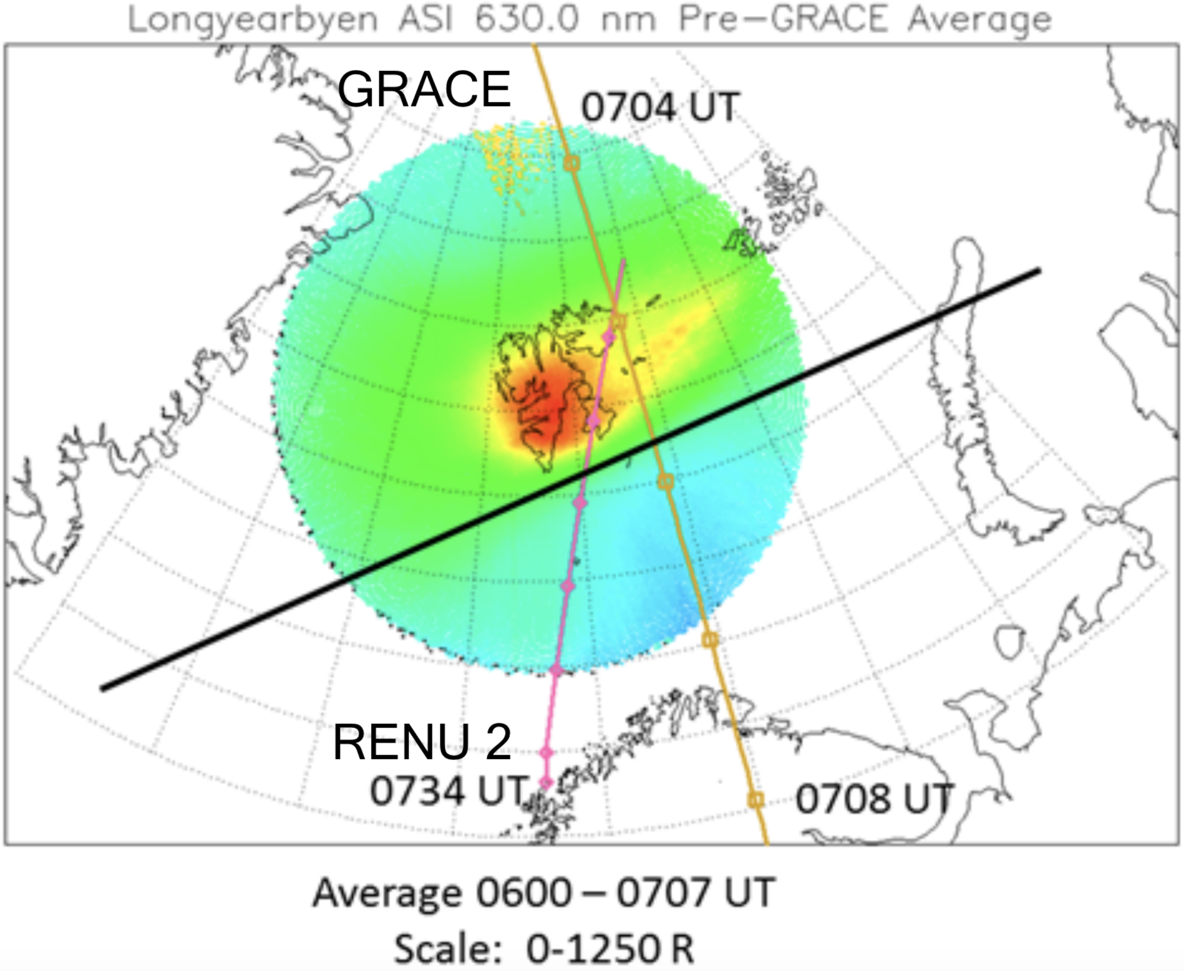

Figure 26: The trajectories of GRACE and RENU2 overlaid on top of the average 6300 nm emission intensity in the cusp region. The emission intensity data was sourced from the filtered ASI at Longyearbyen, which is also used to generate the keograms in Figures 23 and 24. The maximum intensity in the region is 1.25kR. The plot is provided to give a general idea of the location of the cusp and PMAF activity rather than precisely convey the ASI data. The black line shows the approximate orientation of the PMAFs as they moved through the region. Plot courtesy of Jim Clemmons.

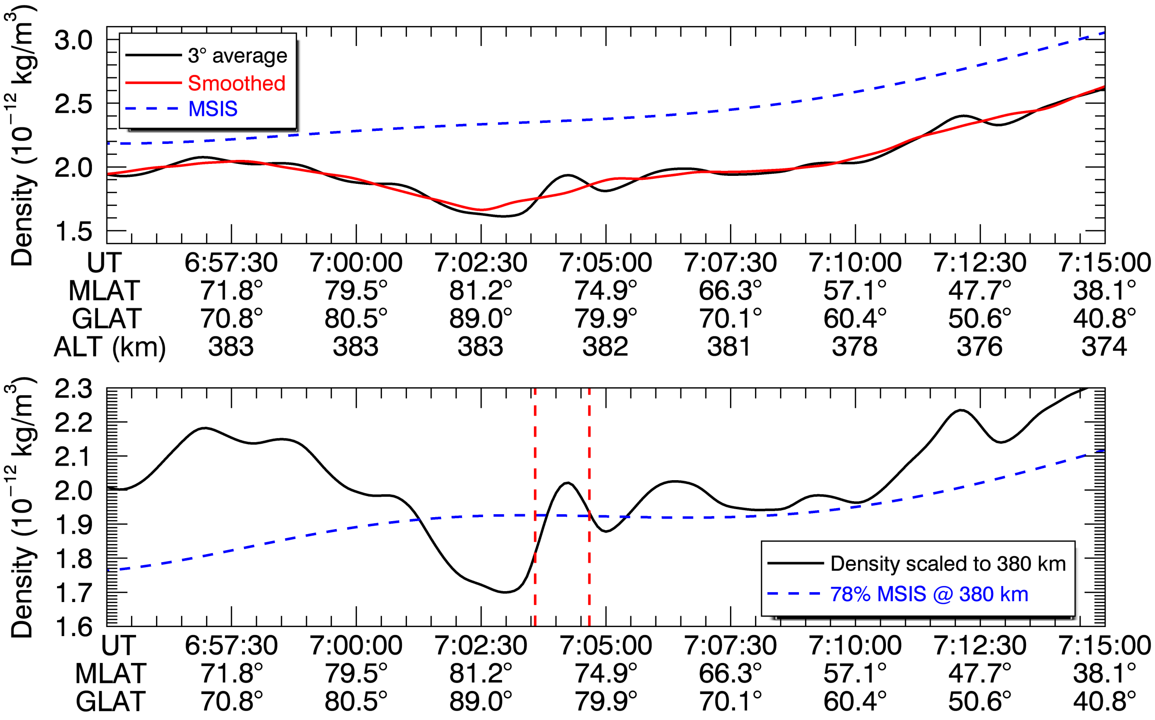

Figure 27: Top: Plot comparison of MSIS modeled density (blue, dashed) to GRACE recorded density (black line: raw, red line: averaged). Bottom: Density (y-axis) re-scaled to better demonstrate the variations present. Both GRACE and MSIS are measurements are scaled to 380 km, and MSIS is multiplied by 0.78 to scale better with the GRACE measurement. Note the cusp is between the two vertical dashed red lines.

In the PMAF, RENU2 traveled at a speed of ~ 2 km/s, while EPLAS completes a full energy sweep every 42 ms, providing a spatial resolution of less than 100 m for each recorded electron distribution functions. Due to the lower altitude and slower speed of the rocket (in comparison to satellite cusp observations), the high time resolution of the EPLAS, and the fortuitous trajectory taken by the rocket to spend over 3 minutes in the PMAF, this data set provides one of the highest spatial and temporal electron spectral and pitch angle datasets from the cusp to date. This resolution allows us to probe electron distributions with scale sizes comparable to those invoked by St.-Maurice et al. (1996) who investigated different mechanisms by which intense FACs 100s of μA/m^2 or greater may be generated by intense fluxes of precipitating electrons with 100s of eV energy scales. Such FACs are of the scale reported by Luhr which were coincident with cusp density enhancements.

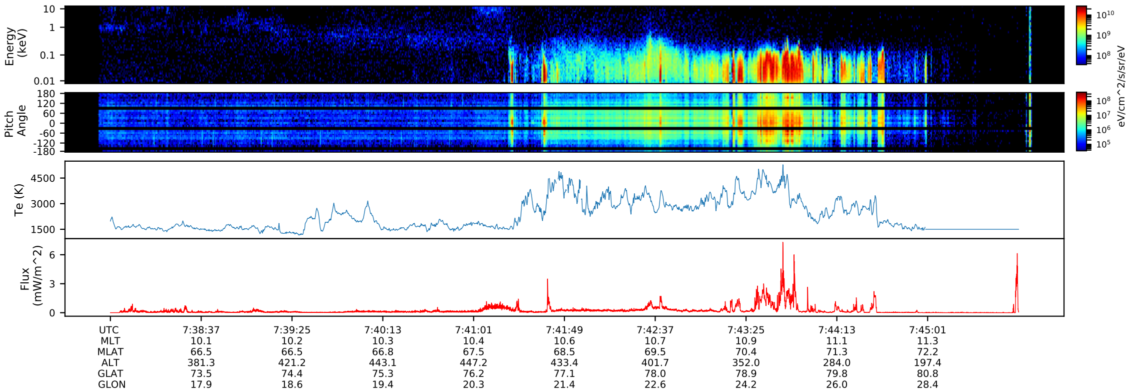

Figure 28: From top to bottom: The electron energy spectra recorded by EPLAS of electrons from 0°-20° in pitch angle, the electron spectra showing pitch angle vs. time, the ambient ionospheric electron temperature recorded by ERPA, and the integrated electron energy flux.

Precipitating and thermal electron measurements are shown in Figure 28. The top plot shows the energy spectrum of the precipitating electrons (the electrons with pitch angles that fall within 20° of the field line, >90% of precipitating electrons recorded by EPLAS). The second shows the pitch angle spectrum of electrons with instrument blindspots indicated. The third plot shows the electron temperature of the ambient ionosphere as measured by ERPA. The bottom plot is the integrated electron energy flux for the electrons shown in the top plot.

9.6 Analysis and Discussion

Inspection of Figure 28 demonstrates the high degree of structure within the PMAF event. The plot largely depicts vertical striations in the spectra, indicative of the rapidly moving thin arcs of electron precipitation similar to those reported by previous studies such as Burchill et al. (2010), Pfaff et al. (1998), Su et al. (2001), Arnoldy et al. (1996), Lunde et al. (2008) and Tanaka:2005. Previous observations have often used the word "bursty" to describe the observed precipitation, implying a temporal nature to the structures (the precipitation is turning on and off). Instead, observations from the RENU2 campaign suggest that PMAF precipitation be viewed instead as a rapidly moving and finely spatially varying structure. Ground based camera data presented in Lessard et al. (2019), and in the supplementary videos of 630.0 and 557.7 nm all sky images show collections of thin arcs which change location in time, as well as the "turning on and off" behavior. This demonstrates the nature of cusp precipitation, i.e. that it is highly structured spatially as well as temporally. To provide a baseline spatial scale for the latitudinal width of these arcs, smallest types of structures recorded by EPLAS are often recorded within three energy sweeps, or 0.126 s. If we make the approximation that the rocket payload and PMAF are travelling parallel with each other, the width of the thinnest structures are on the order of $\sim$ 100 m in latitudinal extent. This also assumes the precipitation is not static on the order of an eighth of a second. (Hecht et al., 2019) use photometer and electron data from EPLAS to demonstrate that the enhancements in precipitation may be as short as 100 ms (note that for the photometer data turning the precipitation on/off has the same effect as varying the location of the enhanced precipitation when the enhancement moves away from a the photometer's field of view) so this estimate of spatial scale may well be limited and better viewed as a lower limit. It should be recognized that although the 630.0 nm emission is more sensitive to the type of soft electron precipitation observed by RENU2, the lifetime of the emission makes it less sensitive to spatially constrained, short time scale features. The fine scale brightenings visible in the supplementary camera data are logically due to the type of intensifications seen in-situ (i.e. that the precipitation is the cause of the auroral forms), although a one-to-one comparison has not been performed. These intensifications are highly field-aligned. The spread in pitch angle distribution seen with the most intense portion of the precipitation is likely due to collisional effects as the payload descends below 300 km. Some small bursts are seen near 180°, similar to signatures of electrons being accelerated back up the field line as reported by Pfaff et al. (1998) from FAST. The average energy of the precipitating electrons ranges between 50 - 200 eV, with the majority of the event being under 100 eV in the PMAF, with energy fluxes of a few mW/m^2.

The temperature of the ambient ionospheric electrons recorded by the ERPA instrument shows a large scale temperature enhancement within the PMAF with localized enhancements evident at smaller scales. The large scale behavior here is important. As the PMAFs sweep through the region, they heat the ionosphere. The next PMAF in the sequence then has a different set of initial conditions when it sweeps through the region; so on and so forth. The cumulative heating effect of PMAFs should not be ignored, as they are rarely solitary events. While there are not before and after datasets to demonstrate this effect explicitly, this should be a logical consideration. More localized electron temperature enhancements also are evident in the ERPA data. Several of these localized temperature enhancements are co-located with strong electron precipitation signatures, such as just before 7:39:41, just after 7:42:37 and 7:44:13. Other, smaller spikes in electron temperature are also evident within the PMAF. These could be from regions that were heated previously and precipitation has either turned off or moved and the region is left to cool. This type of behavior is modeled by Burleigh et al. (2019)

Previous work done by Lund et al. (2012) found that heating the cold ionospheric electrons by soft precipitation required a 100 seconds of active precipitation to drive heating from 200 km altitude up past the peak of the F-region, significantly longer than the timescale computed by Hecht et al. (2019) for how long the intense portions of precipitation are active in an area. Zhu:2018 also modeled electron heating times with inclusion of Alfvén waves and found that temperature enhancements of $\sim$ 500 K are possible with single second time scales. However, neither of these models fit precisely the RENU2 scenario; Zhu et al. (2001) used a characteristic energy for electron precipitation of 1 keV. The study by Lund et al. (2012) was motivated by the SCIFER2 sounding rocket campaign which was also focused on the cusp region and so may be more applicable. However, their work was based on the 630.0 nm optical data, so small spatial scales and short time scales are neglected. Both of these are considerations pertinent to RENU2 data which show T_e enhancements upwards of 1500 K at the largest, but commonly in excess of 500 K. Additionally, the sounding rocket used for in-situ observations used in the study by Lund et al. (2012) had an apogee 1000 km higher than RENU2. One possible mechanism for prompt ionospheric electron heating could be heating by parallel electric fields such as those discussed by Bahcivan and Cosgrove (2010) and references therein. Small scale parallel electric fields with short time scales have previously been inferred from the presence of field-aligned, suprathermal electron bursts by Raitt and Sojka (1977). These types of distributions have been previously observed by Tanaka et al. (2005) and bear a similarity to electron distributions observed during RENU2 as will be shown later.

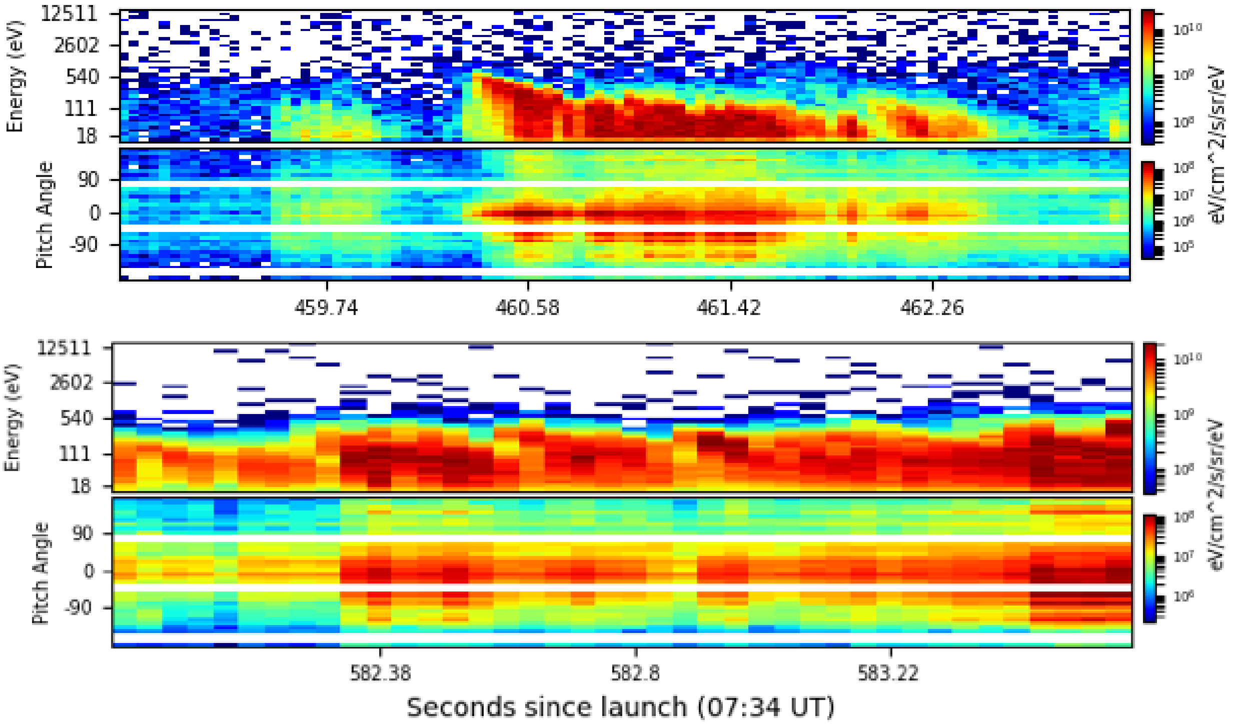

Figure 29: Close ups of the EPLAS (+/- 20 pitch angle) data from selected times which demonstrate the velocity dispersion seen throughout the PMAF

Figure 29 show zoomed-in electron distributions exhibiting a velocity dispersion. These dispersions are chosen from the flight as being the most prominent examples of a feature that is seen throughout the region. Such dispersions are seen with consistent time delays (within three or four sweeps of the EPLAS instrument) and without an apparent set of energies, that is, some of the distributions reach higher energies than others. The examples shown are from portions of the precipitation which had higher fluxes of electrons, but it should be noted that these dispersions are present when fluxes are on the lower side relatively speaking (i.e. when fluxes are closer to 10^9, the examples chosen are an order of magnitude higher because they more clearly exhibit the feature). For distributions which do not show such dispersion, no other structure is prominent other than what Tanaka et al. (2005) called “edge type”, meaning a burst whose spectrum shows a sharp, vertically oriented edge denoting a region of enhanced precipitation with all energies arriving simultaneously within the time resolution of the instrument. Edge type distributions are frequently seen from satellite cusp observations, though they do not always carry this name. Su et al. (2001) and Pfaff et al. (1998) both show similar edge type bursts, though the lack of a dispersion could simply be due to spatial effects caused by the satellite's higher transit speed compared to sounding rocket observations. We can also not rule out that the edge type distributions are simply temporal effects. If the velocity dispersions recorded by EPLAS are interpreted to be temporal, i.e. that lower energy electrons are not recorded until a few instrument sweeps later because of the time delay in travel rather than they are spatially excluded from the equatorward edge of the distribution, then the edge type distributions may not be any different sort of mechanism, simply that the rocket did not arrive early enough to see the dispersion.

For the dispersions, a distance from acceleration region can be calculated as

$$X_{accel} = \Delta t \sqrt{\frac{2}{m}} \frac{\sqrt{E_1 E_2}}{\sqrt{E_1} - \sqrt{E_2}} \tag{9.6.1}$$

Where Δt is taken to be the time delay between the first high energy bin arriving and the first low energy bin arriving, E_1 and E_2 are the higher and lower particle energies respectively and m is the electron mass. This analysis assumes that all electrons are accelerated at the same time and place, as was done by Tanaka et al. (2005). For the distribution shown in 3a, E_1 is 540 eV, E_2 is 18 eV and Δt is 0.126 s, leading to a calculated 388 km from the acceleration region. For 3b, E_1 is 287 eV and E_2 is 18 eV, and Δt is 0.126 seconds, so we infer a distance of 317 km from the acceleration region. This places the acceleration region between 630 km and 850 km, respectively. These types of dispersions are seen throughout the flight. They differ from the rapid fluctuations seen by Lunde et al. (2008) and do not contain any inverted-v structures as was seen by Pfaff et al. (1998) and Oksavik et al. (2004) from FAST satellite data and by Arnoldy et al. (1996); Moen et al. (2012) from sounding rocket observations of the cleft. They do however bear a similar resemblance to the field-aligned Bursts (FABs) reported by Tanaka et al. (2005) except that they also reported the dispersions to be found near regions with inverted-V structures. While the assumption that the electrons are accelerated simultaneously is limited, the proposed mechanism for accelerating electrons via parallel electric fields by Raitt and Sojka (1977) found that an acceleration region for their electrons at 230 eV (similar to the energies observed by RENU2) would only need to be 23 km thick, with parallel field magnitudes on the order of 1 mV/m. St.-Maurice et al. (1996) found that the inclusion of Alfvén waves into this type of framework reduced the thickness of the accelerating region. The inferred source region from RENU2 is also much lower (by roughly an order of magnitude) than that reported by Tanaka et al. (2005). However, the bursts of suprathermal electrons reported by Raitt and Sojka (1977) were observed at low altitude (270 km), much closer to the altitude of RENU2. It should also be noted that with the temporal interpretation of the dispersions in place, the distance to the accelerating region is a lower limit only; if the rocket observation missed the highest energy portion of the distribution, this pushes the region further from the rocket.

Another possibility for source of acceleration causing the electron dispersion are Alfvén wave interactions. Similar dispersions have been reported from the night side polar cap boundary by Chaston et al. (2002); though their event recorded by FAST showed some a portion of the electron spectrum with higher energies which are absent in the RENU2 data. Figure 30 shows the results from a similar analysis as utilized by Chaston et al. (2002). Here, the top two panels show the Fast Fourier Transforms (FFT) of the transverse magnetic and electric fields; both of which show peaks at 0.95 and 2.5 Hz. The waves show reasonably high coherence (bottom panel) above 0.5 until about 8 Hz, and very little to almost no coherence beyond 10 Hz. Higher coherence is better for this analysis, although at the altitudes it can be expected that there is significant wave reflection which naturally limits the coherence as there would be considerable phase mixing. The third panel of Figure 30 shows the phase difference (in π radians in the electric perturbations compared to the magnetic perturbations. For the portion of the spectrum with good coherence below 8 Hz, this panel largely shows a phase difference of π radians as is expected for a traveling wave, except for two instances 2 Hz and 5.5 Hz where the phase difference is very nearly $\pm\frac{\pi}{2}$ as is expected for a standing wave (Chaston et al., 2002).

Modeling results presented by Chaston et al. (2002) demonstrate that electron velocity dispersions of 100 eV scales reveal that the transverse wave field which generates the parallel fields to accelerate the electrons peaks at about 600 km, which is consistent with the acceleration altitude determined by Equation 9.6.1. The signatures of reflected waves in the frequency range expected for Alfvén waves, and the low accelaration region calculated without the presence of wave-particle interactions suggests that standing

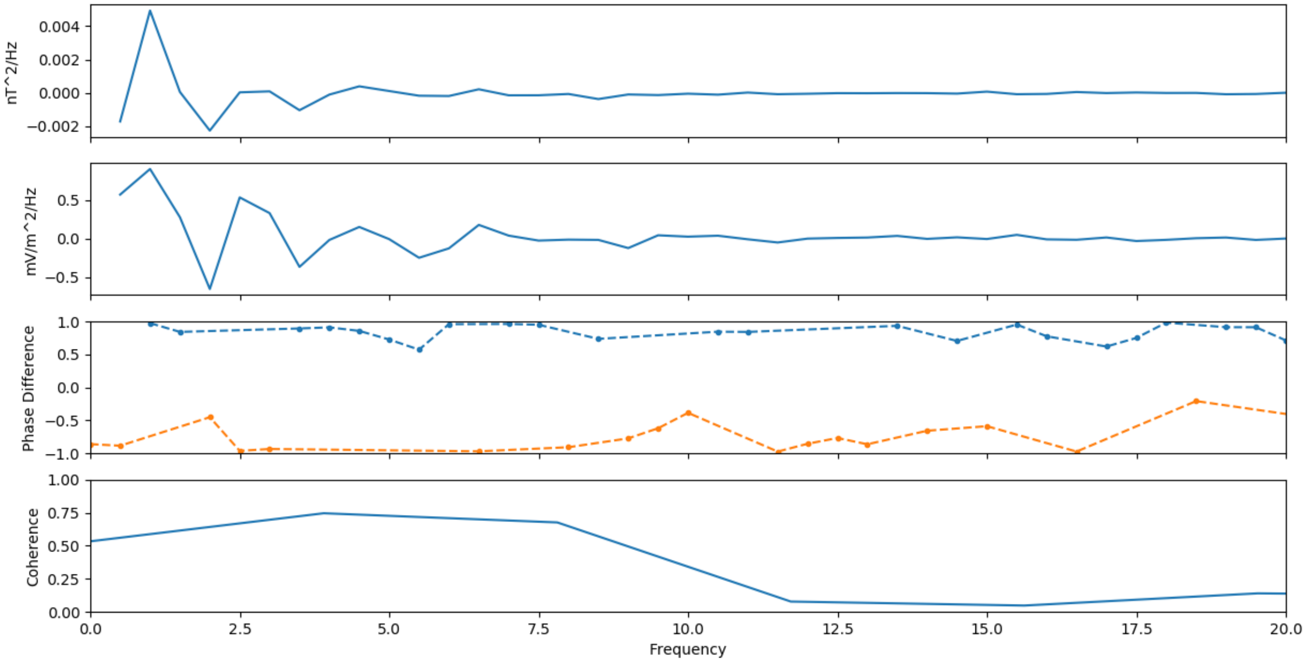

Figure 30: From top to bottom: a) the FFT of the transverse B component b) the FFT of the transverse E component c) the phase difference in E compared to B in π radians d) the wave coherence. This figure uses data from T=459.1 to T= 461.1s which coincides with the dispersion from the top plot in Figure 29.

9.7 Conclusions

Electron precipitation in the cusp is typically comprised of soft, broadband energy distributions highly structured in space and time. Groupings of these distributions form poleward moving auroral forms which sweep across the region and lead to an integrated heating effect over several hundred kilometers. The main takeaways from the data taken by RENU2 are as follows.

1. After the payload entered the cusp region, electron signatures consisted uniquely of field-aligned, soft precipitation which has been associated with Alfvénic aurora. This population can be modeled as having a characteristic energy of 80-100 eV and an energy flux of 1-6 mW/m^2 with a spatial and temporal modulation rather than one broad, consistent region of precipitation.

2. A notable feature in the electron data was an abundance of small-scale (down to $\sim$100 m) features in the precipitation, which compare well with the types of brightenings in the auroral image shown in Lessard et al. (2019). As is seen in the associated imagery for this event, PMAFs consist of clusters of thin arcs that move poleward as a group. Enhancements in electron precipitation cause the thin arcs which change position and may turn on and off, contributing to electron heating through the region through collisional heating.

3. The electron temperature within the PMAF region exhibits both large-scale and small-scale structuring. The large scale heating effect is likely due to the cumulative heating effects as consecutive PMAFs pass through the region. Small-scale heating is consistent with the thin, temporally constrained arcs which comprise a PMAF.

4. The structure observed in the electron data appears similar to previous studies from satellites such as those reported by Newell and Meng (1988) and Pfaff et al. (1998) but the much higher spatial resolution demonstrates small scale dispersions which are not able to be detected by DMSP or FAST. One feature which was not present was a monoenergetic

or inverted-V spectra seen by Pfaff et al. (1998), Tanaka et al. (2005) and Arnoldy et al. (1996).

5. During some portions of the flight, velocity dispersion signatures were observed that placed (as a lower limit) the source region roughly in the 630-850 km altitude range and may be driven by reflected Alfvén waves. This is consistent with prior observation and modeling results presented by Chaston et al. (2002). The majority of the flight data showed no apparent dispersion, similar to the edge type distributions reported by (Tanaka et al., 2005). These could well be the same type of event and the lack of a dispersion simply indicates that the observation missed the time dispersed portion of the precipitation. The velocity dispersion signatures of the type seen by RENU2 have, to the knowledge of the authors, not been reported inside of the cusp without there also being an inverted-V structure present.

CHAPTER 10

Summary and discussion of fine scale structuring

The previous chapters have catalogued three topics of ongoing research covering two rather different auroral events and the development of a new ejectable instrument for sounding rockets. While PMAFs and the cusp region in particular are very commonly associated with ion and neutral upwelling processes, pulsating aurora is only more recently being investigated for its role in the ion upwelling picture. The unifying notion between these two different events is that in each instance, the ionosphere-thermosphere system is responding to drivers which are intrinsically fine-scale. This is important to our understanding of the Magnetosphere-Ionosphere-Thermosphere system as a whole; as we paint our picture with a finer brush, more details emerge which make the picture more clear as a whole.

10.1 Summary of fine scale structuring of RENU2 cusp electrons

The behaviors exhibited by the energetic precipitating electrons and the response by the ambient ionospheric electrons recorded the EPLAS and ERPA instruments respectively, highlight the importance of understanding cross-scale coupling in the cusp region. The cusp, while being a relatively small region of the ionosphere (a few degrees in latitude, 6-8 hours in local time) is still a large area in comparison to the structures within the PMAFs. Structuring within the PMAF was recorded down to three times the spatial/temporal resolution of the EPLAS instrument: on the order of 100 m in scale size and/or 0.126 s. As is the case with any in-situ point measurement from a sounding rocket, it becomes difficult to separate spatial and time-like structures especially near the resolution of the instruments used to observe them. In any case, these fine-scale arcs are predominantly driven by very soft electron precipitation, with bursts commonly having characteristic energies around 50-80 eV. The response of the ionosphere is evident in the electron temperature data which exhibits two different heating scales: a large scale, base line temperature enhancement of approximately twice the background with spatially constrained enhancements overlaid. These spatially constrained enhancements are often, but not always correlated to bursts in the electron precipitation dataset. The logical conclusion to be drawn here is that the bursts in precipitation drive spatially constrained electron heating, and that those electrons stay hot longer than the active precipitation structure is present. As consecutive PMAFs pass through the region, the heating in the cusp region largely becomes a question of the time history of events.

10.2 Summary of fine scale structuring in pulsating aurora event

The study presented within this body of work on pulsating aurora differed greatly not only in the type of event, but also in the experimental set-up compared to the work in the cusp. For the pulsating aurora study, only remote sensing methods (imaging and incoherrent scatter radar) were used to study the event. As such, while the nature of the observations from the ASI and from the PFISR experiment mode preclude the study from being able to observe structure at the 100 m scales that the in-situ data provides from the cusp observations. Still, auroral features recorded by the ASI show detail down to single kilometer scale near zenith (the geometry of ray-optics intrinsic to ASIs mean that spatial resolution decreases away from zenith) and from inspection of the data, it is clear that the diffuse and pulsating aurora is highly structured. Although the PFISR data provides meso scale resolution (24.75 km height resolution, 5 minute integration time) one such feature that is obvious is that the plume of ionization rising out of the D and E region of the ionosphere is coincident with the diminished signatures of convection –

an example of meso-scale to large scale dynamics being modified by fine-scale features (pulsating patches). Furthermore, while the event presented did demonstrate weak ion upflow signatures in the presence of a weak ambipolar field and pulsating aurora – it is clear that the understanding of this type of event would benefit greatly from further study. In-situ measurements in particular of electron temperature, electric and magnetic fields and electron spectra would better elucidate the dynamics such an event, particularly the red line surge. Though the red line arc features prominently as a mesoscale feature, it again appears to be driven by or emerge from fine scale structuring.

10.3 CERPA and its niche in fine scale structure

The development of ejectable instruments is not a new idea in ionospheric science in general; the origins can be traced back at least to the ECHO-6 sounding rocket in 1984. More modern technologies allow the further miniaturization of instruments which are capable of delivering higher resolution measurements than their nearly 40 year old counterparts. The study of the M-I-T system (and really, physics in general) is driven by not just experimental results, but modeling capability as well. Better computing power enables higher resolution models, which require higher resolution measurements to drive/compare simulations.

A sounding rocket outfitted with a pair (or multiple pairs) CERPA ejectables would be uniquely situated to provide snapshots of electron temperature measurements in a 2-D plane. Additionally, although CERPA (or ERPA) does not measure electron energies above 3 eV, higher energy electrons are constantly recorded and so it does provide information about the structuring of the precipitation by recording and binning an “above 3 eV” channel. It is not difficult to imagine the value in this type of measurement for a highly structured event such as a PMAF in being able to better probe the spatial scale of the filamentary enhancements in precipitation; or in the case of pulsating aurora in probing the temperature variation across the patch boundary. In either of these cases and certainly a plethora of other events, this type of measurement is critical to be able to provide modelers with high resolution, multidimensional in-situ measurements of an event. The hope and expectation of this work is that with these measurements modelers will be able to compare their outputs in unprecedented detail – or drive models in ways they were previously unable to with an array of coverage of event rather than a single slice provided by a typical sounding rocket.

Bibliography

Akasofu, S.-I. (1964). The development of the auroral substorm. *Planet. Space Sci.*, 12:273–282.

Anderson, K. A. (1960). Balloon observations of x-rays in the a uroral zone. *J. Geophys. Res.*, 65(2):551–564.

Arnoldy, R. L. (1981). Review of auroral particle precipitation. *Physics of auroral arc formation*, 25:56–66.

Arnoldy, R. L. and Chan, K. W. (1969). Particle substorms observed at the geostationary orbit. *J. Geophys. Res.*, 74:5,019–5,028.

Arnoldy, R. L., Lynch, K. A., Kintner, P. M., Bonnell, J., Moore, T. E., and Pollock, C. J. (1996). Scifer – structure of the cleft ion fountain at 1400 km altitude. *Geophys. Res. Lett.*, 23(14):1,869–1,872.

Bahcivan, H. and Cosgrove, R. (2010). On the generation of large wave parallel electric fields responsible for electron in in the high latitude e region. *J. Geophys. Res.*, 115(A10).

Brown, N. B., Davis, T. B., Hallinan, T. J., and Stenbaek-Nielsen, H. C. (1976). Altitude of pulsating aurora determined by a new instrumental technique. *Geophys. Res. Lett.*, 3(7):403–404.

Burchill, J. K., Knudsen, D. J., Clemmons, J. H., Oksavik, K., Pfaff, R. F., Steigies, C. T., Yau, A. W., and Yeoman, T. K. (2010). Thermal ion upflow in the cusp ionosphere and its dependence on soft electron energy flux. *J. Geophys. Res.*, 115(A05206).

Burleigh, M., Zettergren, M., Lynch, K., Lessard, M., Kenward, D., Hysell, D., Clausen, L., and Moen, J. (2019). Transient ionospheric upflow driven by poleward moving auroral forms observed during the Rocket Experiment for Neutral Upwelling 2 (RENU2) campaign. *Geophys. Res. Lett.* submitted.

Carlson, C. W., Curtis, D. W., Paschmann, G., and Michael, W. (1983). An instrument for rapidly measuring plasma distribution functions with high resolution. *Adv. Space Res.*, 2.

Chapman, S. and Ferraro, V. C. A. (1931). A new theory of magnetic storms. *Terr. Mag. and Atmos. Elec.*, 36(2):77–97.

Chaston, C., Peria, W., Carlson, C., Ergun, R., and McFadden, J. (2001). Fast observations of inertial alfvn waves and electron acceleration in the dayside aurora. *Physics and Chemistry of the Earth, Part C: Solar, Terrestrial Planetary Science*, 26(1):201 – 205.

Chaston, C. C., Bonnell, J. W., Carlson, C. W., Berthomier, M., Peticolas, L. M., Roth, I., McFadden, J. P., Ergun, R. E., and Strangeway, R. J. (2002). Electron acceleration in the ionospheric Alfven resonator. *Journal of Geophysical Research (Space Physics)*, 107(A11):1413.

Chaston, C. C., Bonnell, J. W., Carlson, C. W., McFadden, J. P., Ergun, R. E., and Strangeway, R. J. (2003). Properties of small-scale alfvén waves and accelerated electrons from fast. *J. Geophys. Res.*, 108(A4).

Chaston, C. C., Bonnell, J. W., Carlson, C. W., McFadden, J. P., Ergun, R. E., Strangeway, R. J., and Lund, E. J. (2004). Auroral ion acceleration in dispersive alfve n waves. *J. Geophys. Res.*, 109(A04205).

Chaston, C. C., Carlson, C. W., McFadden, J. P., Ergun, R. E., and Strangeway, R. J. (2007). How important are dispersive alfve n waves for aur- oral particle acceleration? *Geophys. Res. Lett.*, 34(L07101).

Chaston, C. C., Peticolas, L. M., Carlson, C. W., McFadden, J. P., Mozer, F., Wilber, M., Parks, G. K., Hull, A., Ergun, R. E., Strangeway, R. J., Andre, M., Khotyaintsev, Y., Goldstein, M. L., AcuñA, M., Lund, E. J., Reme, H., Dandouras, I., Fazakerley, A. N., and Balogh, A. (2005). Energy deposition by Alfvén waves into the dayside auroral oval: Cluster and FAST observations. *Journal of Geophysical Research (Space Physics)*, 110(A2):A02211.

Chaston, C. C. and Seki, K. (2010). Small-scale auroral current sheet structuring. *Journal of Geophysical Research (Space Physics)*, 115(A11):A11221.

Cohen, I. J., Widholm, M., Lessard, M. R., Riley, P., Heavisides, J., Moen, J. I., Clausen, L. B. N., and Bekkeng, T. A. (2016). Rocket-borne measurements of electron temperature and density with the electron retarding potential analyzer instrument. *J. Geophys. Res. Space Phy*, 121:6,774–6,782.

Davis, T. N. (1978). Observed microstructure of auroral forms. *Journal of Geomagnetism and Geoelectricity*, 30(4):371–380.

Deng, Y., Sheng, C., Su, Y.-J., Hairston, M. R., Knipp, D., Huang, C. Y., Ober, D., Redmon, R. J., and Coley, R. (2015). Correlation between poynting flux and soft electron precipitation in the dayside polar cap boundary regions. *J. Geophys. Res. Space Phys.*, 120(10):9,102–9,109.

Dunbar, B. (2006). The history of auroras.

Eastwood, J. P. and Kiehas, S. A. (2015). Origin and Evolution of Plasmoids and Flux Ropes in the Magnetotails of Earth and Mars. In *Magnetotails in the Solar System*, volume 207, pages 269–287.

Eather, R. H. (1969). Short-period auroral pulsations in $\lambda 6300 oi. J. Geophys. Res., 74(21): 4998 - -5004$.

Ergun, R. E. (1998). Fast satellite observations of electric field structures in the auroral zone. *Geophys. Res. Lett.*, 25.

Evans, D. S., G. T, D., Voss, H. D., Imhof, W. L., Mobilia, J., and Chiu, Y. T. (1987). Interpretation of electron spectra in morningside pulsating aurorae. *J. Geophys. Res.*, 92(A11):12295–12306.

Fairfield, D. H., Lepping, R. P., Jr., E. W. H., Blame, S. J., and Asbridge, J. R. (1981). Simultaneous measreuments of magnetotail dynamics by imp spacecraft. *J. Geophys. Res.*, 86:1,396–1,414.

Fairfield, D. H. and Ness, N. F. (1970). Configuration of the geomagnetic tail during substorms. *J. Geophys. Res.*, 75:7,032.

Fasel, G. J. (1995). Dayside poleward moving auroral forms: A statistical study. , 100(A7):11891–11906.

Feldstein, Y. I. (1986). A quarter of a century with the auroral oval. *EOS*, 67:761,765–767.

Frederick-Frost, K. M., Lynch, K. A., Jr., P. K., Klatt, E., Lorentzen, D., Moen, J., Ogawa, Y., and Widholm, M. (2007). Sersio: Svalbard eiscat rocket study of ion outflows. *J. Geophys. Res.*, 112(A8).

Fritz, B. A., Lessard, M. L., Blandin, M. J., and Fernandes, P. A. (2015). Structure of black aurora associated with pulsating aurora. *J. Geophys. Res.*, 120:10096–10106.

Fujii, R., Oguti, T., and Yamamoto, T. (1985). Relationships between pulsating auroras and field-aligned electric currents. *National Institute Polar Research Memoirs*, 36.

Ganushkina, N. Y., Dandouras, I., Shprits, Y. Y., and Cao, J. (2011). Locations of boundaries of outer and inner radiation belts as observed by cluster and double star. *J. Geophys. Res.*, 116(A09234).

Gillies, D. M., Knudsen, D., Donovan, E., Jackel, B., Gillies, R., and Spanswick, E. (2017). Identifying the 630 nm auroral arc emission height: A comparison of the triangulation, fac profile and electron density methods. *J. Geophys. Res.*, 122(8).

Gold, T. (1959). Motions in the magnetosphere of earth. *J. Geophys. Res.*, 64(9):1219–1224.

Gonzalex, W. D., Joselyn, J. A., Kamide, Y., Kroehl, H. W., Rostoker, G., Tsurutani, B. T., and Vasyliunas, V. M. (1994). What is a geomagnetic storm? *J. Geophys. Res.*, 99(A4):5771–5792.

Grodent, D. (2015). A brief review of ultraviolet auroral emissions on giant planets. *Space Science Reviews*, 187:23–50.

Grono, E. and Donovan, E. (2018). Differentiating diffuse auroras based on phenomenology. *Ann. Geophys.*, 36:891–898.

Hecht, J. H., Clemmons, J. H., Lessard, M. R., Kenward, D. L., Sadler, B. F., Fritz, B. A., Evans, J. S., , and Lynch, K. A. (2019). A New Technique for Estimating The Lifetime of Bursts of Electron Precipitation From Sounding Rocket Measurements. *Geophys. Res. Lett.* submitted.

Heikkila, W. J. (1972). The morphology of auroral particle precipitation. In Bowhill, S. A., Jaffe, L. D., and Rycroft, M. J., editors, *Space Research Conference*, volume 2 of *Space Research Conference*, pages 1343–1355.

Heikkila, W. J. (1985). Definition of the cusp. In Holtet, J. A. and Egeland, A., editors, *The Polar Cusp*, volume 145 of *NATO Advanced Workshop*.

Heikkila, W. J. and Winningham, J. D. (1971). Penetration of magnetosheath plasma to low altitudes through the dayside magnetospheric cusps. *J. Geophys. Res.*, 76(4):883–891.

Humberset, B. K., Gjerloev, J. W., Samara, M., Michell, R. G., and Mann, I. R. (2016). Temporal characteristics and energy deposition of pulsating auroral patches. *J. Geophys. Res.*, 121:7087–7107.

Jones, S. L., Lessard, M. R., Rychert, K., Spanswick, E., and Donovan, E. (2011). Large-scale aspects and temporal evolution of pulsating aurora. *J. Geophys. Res.*, 116(A03214).

Jones, S. L., Lessard, M. R., Rychert, K., Spanswick, E., Donovan, E., and Jaynes, A. N. (2013). Persistent, widespread pulsating aurora: A case study. *J. Geophys. Res.*, 118:2998–3006.

Kasahara, S., Miyoshi, Y., Yokota, S., Mitani, T., Kasahara, Y., Matsuda, S., Kumamoto, A., Matsuoka, A., Kazama, Y., Frey, H. U., Angelopoulos, V., Kurita, S., Keika, K., Seki, K., and Shinohara, I. (2018). Pulsating aurora from electron scattering by chorus waves. *Nature*, 554:337–339.

Kaufmann, R. L. (1987). Substorm currents: growth phase and onset. *J. Geophys. Res.*, 92:7,472–7,489.

Keith, W. R., Winningham, J. D., Goldstein, M. L., Wilber, M., Fazakerley, A. N., Rème, H., Fritz, T. A., Balogh, A., Cornilleau-Wehrlin, N., and Maksimovic, M. (2005). Observations of a Unique Cusp Signature at Low and Mid Altitudes. *Surveys in Geophysics*, 26:307–339.

Kelley, M. C. (2009). *The Earth's Ionosphere*. Academic Press, 2 edition.

Khazanov, G. V., Glocer, A., and Himwich, E. W. (2014). Magnetosphere-ionosphere energy interchange in the electron diffuse aurora. *J. Geophys. Res.*, 119:171–184.

Khazanov, G. V., Sibeck, D. G., and Zest, E. (2017). Major pathways to electron distribution function formation in regions of diffuse aurora. *J. Geophys. Res.*, 122:4251–4265.

Knudsen, W. C. (1966). Evaluation and demonstration of the use of retarding potential analyzers for measuring several ionospheric quantities. *J. Geophys. Res.*, 71(19):4669–4678.

Lessard, M. R. (2013). *A Review of Pulsating Aurora*, pages 55–68. American Geophysical Union (AGU).

Lessard, M. R., Fritz, B., Sadler, B., Cohen, I., David Kenward, N. G. J. H. C., Hecht, J. H., Lynch, K. A., Harrington, M., Hysell, D., Crowley, G., Sigernes, F., Syrjäsuo, M., Ellingson, P., Partamies, N., Moen, J., Clausen, L., Oksavik, K., and Yeoman, T. (2019). Overview of the Rocket Experiment for Neutral Upwelling Sounding Rocket 2 (RENU2). *Geophys. Res. Lett.* submitted.

Li, S. S., Liu, J., Angelopoulos, V., Runov, A., Zhou, X. Z., and Kiehas, S. A. (2014). Antidipolarization fronts observed by ARTEMIS. *Journal of Geophysical Research (Space Physics)*, 119(9):7181–7198.

Liang, J., Donovan, E., Jackel, B., Spanswick, E., and Gillies, M. (2016). On the 630nm red-line pulsating aurora: Red-line emission geospace observatory pbservations and model simulations. *J. Geophys. Res.*, 121:7988–8012.

Lockwood, M., Sandholt, P. E., and Cowley, S. W. H. (1989). Interplanetary magnetic field control of dayside auroral activity and the transfer of momentum across the dayside magnetopause. *Planet. Space Sci.*, 37(11):1347–1365.

Luehr, H. and Buchert, S. (1988). Observational evidence for a link between currents in the geotail and in the auroral ionosphere. *Annales Geophysicae*, 6:169–175.

Luhr, H., Rother, M., Kohler, W., Ritter, P., and Grunwaldt, L. (2004). Thermospheric up-welling in the cusp region: Evidence from champ observations. *Geophys. Res. Lett.*, 31(L06805).

Lund, E. J., Lessard, M. R., Sigernes, F., Lorentzen, D. A., Oksavik, K., Kintner, P. M., Lynch, K. A., Huang, D. H., Zhang, B. C., Yang, H. G., and Ogawa, Y. (2012). Electron temperature in the cusp as measured with the scifer-2 sounding rocket. *J. Geophys. Res.*, 117(A06326).

Lunde, J., Buchert, S. C., Ogawa, Y., Hirahara, M., Seki, K., Ebihara, Y., Sakanoi, T., Asamura, K., Okada, M., Raita, T., and Haggstrom, I. (2008). Ion-dispersion and rapid electron fluctuations in the cusp: a case study. *Ann. Geophys.*, 26:2485–2502.

Lynch, K. A., Hampton, D. L., Zettergren, M., Bekkeng, T. A., Conde, M., Fernandes, P. A., Horak, P., Lessard, M., Miceli, R., Michell, R., Moen, J., Nicalls, M., Powell, S. P., and Samara, M. (2015). Mica sounding rocket observations of conductivity-gradient-generated auroral ionospheric responses: Small-scale structure with large-scale drivers. *J. Geophys. Res.*, 120(11).

Marklund, G., Blomberg, L., Falthammar, C.-G., and Lindqvist, P.-A. (1994). On intense diverging electric fields associated with black aurora. *Geophys. Res. Lett.*, 21(17):1859–1862.

Marklund, G., Karlsson, T., and Clemmons, J. (1997). On low-altitude particle acceleration and intense electric fields and their relationship to black aurora. , 102(A8):17509–17522.

McEwan, D. J., Yee, E., Whalen, B. A., and Yau, A. W. (1981). Electron energy measurements in pulsating auroras. *Can. J. Phys.*, 59(8):1106–1115.

McPherron, R. L. (1997). *The Role of Substorms in the Generation of Magnetic Storms*, pages 131–147. American Geophysical Union (AGU).

Mende, S. B., Frey, H. U., and Angelopoulos, V. (2016). Source of the dayside cusp aurora. *Journal of Geophysical Research (Space Physics)*, 121(8):7728–7738.

Miyoshi, Y., Oyama, S., Saito, S., Kurita, S., Fujiwara, H., Kataoka, R., Ebihara, Y., Kletzing, C., Reeves, G., Santolik, O., Clilverd, M., Rodger, C. J., Turunen, E., and Tsuchiya, F. (2015). Energetic electron precipitation associated with pulsating aurora: Eiscat and van allen probe observations. *J. Geophys. Res.*, 120:2754–2766.

Moen, J., Oksavik, K., Abe, T., Lester, M., Saito, Y., Bekkeng, T. A., and Jacobsen, K. S. (2012). First in-situ measurements of hf radar echoing targets. *Geophys. Res. Lett.*, 39(L07104).

Moen, J., Oksavik, K., and Carlson, H. C. (2004). On the relationship between ion upflow events and cusp auroral transients. , 31(11):L11808.

Moore, T. E., Fok, M. C., and Garcia-Sage, K. (2014). The ionospheric outflow feedback loop. *Journal of Atmospheric and Solar-Terrestrial Physics*, 115:59–66.

Newell, P. T. (2000). Reconsidering the inverted-v particle signature: Relative frequency of large scale electron acceleration events. *J. Geophys. Res.*, 105(A7):15,779–15,794.

Newell, P. T. and Meng, C.-I. (1988). The cusp and cleft/boundary layer: low-altitude identification and statistical local time variation. *J. Geophys. Res.*, 93(A12):14,549–14,556.

Newell, P. T. and Meng, C.-I. (1992). Mapping the dayside ionosphere to the magnetosphere according to particle precipitation characteristics. , 19(6):609–612.

Newell, P. T., Sotirelis, T., and Wing, S. (2009). Diffuse, monoenergetic, and broadband aurora: The global precipitation budget. *J. Geophys. Res.*, 114(A09207).

Newell, P. T., Sotirelis, T., and Wing, S. (2009). Diffuse, monoenergetic, and broadband aurora: The global precipitation budget. *Journal of Geophysical Research (Space Physics)*, 114(A9):A09207.

Newell, P. T., Sotirelis, T., and Wing, S. (2009). Diffuse, monoenergetic, and broadband aurora: The global precipitation budget. *J. Geophys. Res.*, 114(A09207).

Nishimura, Y., Lessard, M. R., Katoh, Y., Miyoshi, Y., Grono, E., Partamies, N., Sivadas, N., Hosokawa, K., Fukizawa, M., Samara, M., Michell, R. G., Kataoka, R., Sakanoi, T., Whiter, D. K., Oyama, S.-i., Ogawa, Y., and Kurita, S. (2020). Diffuse and Pulsating Aurora. , 216(1):4.

Oksavik, K. (2018).

Oksavik, K., Soraas, F., Moen, J., Pfaff, R., Davies, J. A., and Lester, M. (2004). Simultaneous optical, cutlass hf radar, and fast spacecraft observations: signatures of boundary layer processes in the cusp. *Ann. Geophys.*, 22:511–525.

Partamies, N., Whiter, D., Kadokura, A., Kauristie, K., Tyssoy, H. N., Massetti, S., Stauning, P., and Raita, T. (2017). Occurrence and average behavior of pulsating aurora. *J. Geophys. Res.*, 122:5606–5618.

Peticolas, L. M., Hallinan, T. J., Stenbaek-Bielsen, H., Bonnell, J. W., and Carlson, C. W. (2002). A study of black aurora from aircraft-based optical observations and plasma measurements on fast. *J. Geophys. Res.*, 107(A8).

Pfaff, R., Clemmons, J., Carlson, C., Ergun, R., McFadden, J., Mozer, F., Temerin, M., Klumpar, D., Peterson, W., Shelley, E., Moebius, E., Kistler, L., Strangeway, R., Elphic, R., and Cattell, C. (1998). Initial fast observations of acceleration processes in the cusp. *Geophys. Res. Lett.*, 25(12):2,037–2,040.

Raitt, W. J. and Sojka, J. J. (1977). Field-aligned suprathermal electron fluxes below 270 km in the auroral zone. *Planet. Space Sci.*, 25:5–13.

Reiff, P. H. (1979). Low-altitude signatures of the boundary layers. In Battrick, B., Mort, J., Haerendel, G., and Ortner, J., editors, *Magnetospheric Boundary Layers*, volume 148 of *ESA Special Publication*.

Rostoker, G., Akasofu, S.-I., Foster, J., Greenwald, R. A., Kamide, Y., Kawasaki, K., Lui, A. T. Y., McPherron, R. L., and Russell, C. T. (1994). Magnetospheric substorms–definition and signatures. *J. Geophys. Res.*, 99(A4):5771–5792.

Royrvik, O. and Davis, T. N. (1978). Pulsating aurora: local and global morphology. *J. Geophys. Res.*, 82(29):4720–4740.

Sakaguchi, K., Shiokawa, K., Donovan, E., Nakajima, A., Hiraki, Y., Trondsen, T., and Plaschke, F. (2011). Periodic black auroral patches at the dawnside dipolarization front during a substorm. *Journal of Geophysical Research (Space Physics)*, 116:A00I18.

Samara, M., Michell, R. G., and Khazanov, G. V. (2017). First optical observations of interhemispheric electron reflections within pulsating aurora. *Geophys. Res. Lett.*, 44:2618–2623.

Sandholt, P. E. and Farrugia, C. J. (2007). Poleward moving auroral forms (pmafs) revisited: responses of the aurorae, plasma convection and birkeland currents in the pre- and postnoon sectors under positive and negative imf by conditions. *Ann. Geophys.*, 25:1,629–1,625.

Sandholt, P. E., Lockwood, M., Oguti, T., Cowley, S. W. H., Freeman, K. S. C., Lybekk, B., Egeland, A., and Willis, D. M. (1990). Midday auroral breakup events and related energy and momentum transfer from the magnetosheath. *J. Geophys. Res.*, 95(A2):1,039–1,060.

Serbu, G. P. (1964). Results from the imp-1 retarding potential analyzer. *NASA Internal Report*, TMX 5504(X-615-64-109).

Shue, J.-H. and Song, P. (2002). The location and shape of the magnetopause. *Planetary and Space Science*, 50(5-6):549–558.

Song, P., Gombosi, T. I., and Ridley, A. J. (2001). Three fluid ohm's law. *J. Geophys. Res.*, 106(A5).

St.-Maurice, J.-P., Kofman, W., and James, D. (1996). In situ generation of intense parallel electric fields in the lower ionosphere. *J. Geophys. Res.*, 101(A1):335–356.

Strangeway, R. J. (2012). The equivalence of joule disspation and frictional heating in the collisional ionosphere. *J. Geophys. Res.*, 117(A02310).

Strangeway, R. J., Ergun, R. E., Su, Y.-J., Carlson, C. W., and Elphic, R. C. (2005). Factors controlling ionospheric outflows as observed at intermediate altitudes. *J. Geophys. Res.*, 110(A03221).

Su, Y.-J., Ergun, R. E., Peterson, W. K., Onsager, T. G., Pfaff, R., Carlson, C. W., and Strangeway, R. J. (2001). Fast auroral snapshot observations of cusp electron and ion structures. *J. Geophys. Res.*, 106:25595–25600.

Sugiura, M. and Chapman, S. J. (1961). In *THE AVERAGE MORPHOLOGY OF GEOMAGNETIC STORMS WITH SUDDEN COMMENCEMENT*.

Tanaka, H., Saito, Y., Asamura, K., Ishii, S., and Mukai, T. (2005). High time resolution measurement of multiple electron precipitations with energy-time dispersion in high-latitude part of the cusp region. *Journal of Geophysical Research (Space Physics)*, 110(A7):A07204.

Tu, J., Song, P., and Vasyliunas, V. M. (2011). Ionosphere/thermosphere heating determined from dynamic magnetosphere-ionosphere/thermosphere coupling. *J. Geophys. Res.*, 116(A09311).

Varney, R. H. and Zhang, B. (2017). Influence of Cusp Neutral Upwelling on Ion Upflow and Outflow. In *AGU Fall Meeting Abstracts*, volume 2017, pages SA42B–06.

Vasyliunas, V. M. and Song, P. (2005). Meaning of ionospheric joule heating. *J. Geophys. Res.*, 110(A02301).

Weimer, D. R. and Gurnett, D. A. (1993). Large-amplitude auroral electric fields measured with de 1. *J. Geophys. Res.*, 98(A8):13,557–13,564.

Welling, D. T., Jordanova, V. K., Glocer, A., Toth, G., Liemohn, M. W., and Weimer, D. R. (2015). The two-way relationship between ionospheric outflow and the ring current. *Journal of Geophysical Research (Space Physics)*, 120(6):4338–4353.

Zhu, H., Otto, A., Lummerzheim, D., Rees, M. H., and Lanchester, B. S. (2001). Ionosphere-magnetosphere simulation of small-scale structure and dynamics. *J. Geophys. Res.*, 106(A2):1795–1806.